Universidade de Aveiro Departamento de Física
2016

Luís Miguel da Conceição Moutinho

Estudos para o sistema de rastreamento da experiência NEXT e desenvolvimento de dispositivos médicos usando SiPMs

Studies on the NEXT experiment tracking system and development of medical devices with SiPMs

Universidade de Aveiro Departamento de Física
2016

Universidade do Porto Faculdade de Ciências

Universidade do Minho Departamento de Física

Luís Miguel da Conceição Moutinho

Estudos para o sistema de rastreamento da experiência NEXT e desenvolvimento de dispositivos médicos usando SiPMs

Studies on the NEXT experiment tracking system and development of medical devices with SiPMs

Universidade de Aveiro Departamento de Física
2016

Universidade do Porto Faculdade de Ciências

Universidade do Minho Departamento de Física

Luís Miguel da Conceição Moutinho

Estudos para o sistema de rastreamento da experiência NEXT e desenvolvimento de dispositivos médicos usando SiPMs

Studies on the NEXT experiment tracking system and development of medical devices with SiPMs

Dissertação apresentada à Universidade de Aveiro para cumprimento dos requisitos necessários à obtenção do grau de Doutor em Física, realizada sob a orientação científica do Doutor João Filipe Calapez de Albuquerque Veloso, Professor Auxiliar com Agregação do Departamento de Física da Universidade de Aveiro e coorientação do Professor Doutor Joaquim Marques Ferreira dos Santos, Professor Catedrático do Departamento de Física da Universidade de Coimbra.

O autor foi financiado pela Fundação para a Ciência e Tecnologia (FCT), através da bolsa de Doutoramento com a referência SFRH/BD/80179/2011, no âmbito do Quadro de Referência Estratégico Nacional (QREN) e do Programa Operacional de Potencial Humano (POPH), comparticipado pelo Fundo Europeu e por fundos nacionais do Ministério da Educação e Ciência (MEC). Este trabalho foi desenvolvido no âmbito do projeto PTDC/FIS-NUC/2525/2014 - Detection of the neutrinoless double beta decay in Xe-136: the NEXT experiment, COMPETE e FEDER.

o júri / the jury

presidente / president

Doutor Paulo Jorge dos Santos Gonçalves Ferreira
Professor Catedrático do Departamento de Eletrónica, Telecomunicações e Informática da Universidade de Aveiro

vogais / examiners committee

Doutor Luís Filipe dos Santos Garcia Peralta
Professor Associado com Agregação da Faculdade de Ciências da Universidade de Lisboa

Doutor Luís Manuel Cadillon Martins Costa
Professor Associado com Agregação do Departamento de Física da Universidade de Aveiro

Doutor Luís Manuel Panchorrinha Fernandes
Investigador Principal da Faculdade de Ciências e Tecnologia da Universidade de Coimbra

Doutor João Filipe Calapez de Albuquerque Veloso
Professor Auxiliar com Agregação do Departamento de Física da Universidade de Aveiro

Doutor João António Miranda dos Santos
Coordenador do Grupo de Física Médica e Proteção Radiológica do Centro de Investigação do Instituto Português de Oncologia do Porto, Francisco de Gentil, E.P.E.

Acknowledgements

I would like to express my sincere gratitude to my advisor Prof. João Veloso for the continuous support during my Ph.D studies and related research, for his patience, motivation, and immense knowledge. I also thank to Prof. Joaquim Santos from the Physics Department of University of Coimbra for the support has co-advisor and the Coimbra group part of the NEXT collaboration.

I am also thankful to J.J. Gómez-Cadenaz, NEXT spokesperson, to David Nygren and Azriel Goldsmith for having me at their labs for month periods integrating their research teams.

I thank to the staff from the Serviço de Radiologia of the Centro Hospitalar e Universitário de Coimbra, namely Paulo César Simões and Paulo Rachinhas for the availability and for the possibility to perform the studies in clinical conditions for the characterization of the dosimeter prototype. I thank to my fellow labmates for the stimulating discussions and for all the fun we have over the last years. I take this opportunity to express my gratitude to all of the Physics Department faculty members, for their help and support.

I would like to thank to my family: my parents and to my brother and sister for supporting me throughout this academic journey. I am also grateful to Ana Picado who strongly supported me through this venture thus contributed to the development of this research.

palavras-chave SiPM, NEXT collaboration, $0\nu\beta\beta$, Brachytherapy, Dosimeter, PET, easyPET

resumo

Os recentes desenvolvimentos na área dos fotodetectores de estado sólido, nomeadamente os fotomulplicadores de silício (SiPM), permitiram a proliferação desta tecnologia num vasto número de aplicações em áreas distintas. Estes fotosensores robustos, versáteis e com um preço competitivo, tornaram-se uma das mais promissoras alternativas aos tubos fotomultiplicadores para deteção de baixo nível de luz, especialmente para aplicações onde é necessário um grande número de fotodetectores. Estes fotosensores multi-pixel, são capazes de deteção de fotão único, permitindo obter ao mesmo tempo informação sobre fotão de interação e energia. Os estudos realizados no âmbito deste programa doutoral e reportados neste documento dividem-se em três aplicações principais: colaboração no desenvolvimento do sistema de rastreamento (*tracking system*) da experiência NEXT na área da física de neutrinos e *Neutrinoless Double Beta Decay* ($0\nu\beta\beta$), que comporta $\sim$7.000 SIPMs para identificação da assinatura $0\nu\beta\beta$, um dosímetro para braquiterapia de próstata e um sistema PET didático - easyPET.

Foram realizados vários estudos para caracterização da nova geração de SiPMS. Como verificado, estes dispositivos apresentam características melhoradas tais como uma maior eficiência quântica e menor crosstalk, afterpulsing e sensibilidade térmica.

Esta nova geração de SiPMs adequa-se aos requisitos para aplicação no *tracking system* no NEXT. No entanto, uma maior eficiência quântica no ultravioleta de vazio (VUV) é desejável.

Foi avaliada a aplicação de SiPMs em sensores de radiação para dosimetria médica. Foi desenvolvido um dosímetro com base em fibra ótica cintilante. O dispositivo foi caracterizado numa larga gama de energia e em regimes de baixa e de alta taxa de dose. O dosímetro foi avaliado em ambiente clínico recriando as condições de braquiterapia HDR, tratamento aplicado no tratamento de cancros da próstata e mama. Conforme verificado, os SiPM apresentam elevada dependência com a temperatura sendo portanto necessárias técnicas de compensação ou de estabilização. O protótipo do easyPET foi implementado com sucesso. A tecnologia foi licenciada e é esperada a sua comercialização até ao fim do ano de 2016.

Dos estudos realizados nas várias aplicações, conclui-se que os SiPMs são fotodetectores muito versáteis devido à sua alta sensibilidade, elevado ganho, insensibilidade a campos magnéticos, de rápida resposta e de pequenas dimensões, abrindo a possibilidade de aplicação desta tecnologia em múltiplos campos permitindo uma infinidade de novos conceitos de detectores, tais como na física de alta energia e aplicações de imagiologia biomédica.

keywords SiPM, NEXT collaboration, $0\nu\beta\beta$, Brachytherapy, Dosimeter, PET, esayPET

abstract

The recent developments of solid-state photodetectors, namely Silicon Photomultipliers (SiPMs), allowed a proliferation of this technology through numerous applications. These robust and versatile photosensors with an attractive price have become one of most promising alternatives for low light level detection, especially for applications where a large number of devices is required.

These multi-pixel photosensors, capable of single photon detection, allow to obtain at the same time information on photon-interaction and energy.

The Ph.D studies reported in this document cover three main applications: the NEXT experiment, a Neutrinoless Double Beta Decay ($0\nu\beta\beta$) experiment using $\sim$7000 SiPMs in the tracking system for topological signature identification, a dosimeter for prostate brachytherapy and a simple PET system for education purposes - the easyPET.

Several studies were conducted envisaging the characterization of a new generation of SiPMs. As verified, these devices present improved features such as higher quantum efficiency, lower crosstalk and afterpulsing and lower thermal sensitivity. This new generation of SiPMs suits the requirements for application on the NEXT TPC tracking plane. Although, higher quantum efficiency at the vacuum ultraviolet (VUV) is a desirable feature.

The application of the SiPMs in radiation sensors intended for dosimetry in medical applications was evaluated. A dosimeter was developed and characterized in a wide energy range and at both low and high dose rates (LDR and HDR). The dosimeter was evaluated in real treatment facilities related to HDR-brachytherapy for treatment of prostate and breast cancers. According to the results, SiPMs present a high temperature dependency and compensation techniques are required in precision measurements.

The easyPET was successfully prototyped. The technology has been licensed and is expected to be commercialized in late 2016.

From the studies on the several applications, one concludes that the SiPMs are very versatile photodetectors due to their high sensitivity, high gain, small size, insensibility to magnetic fields, easiness of optical couplings, low bias voltage and fast response, opening the possibility to apply this technology in multiple fields enabling a plethora of new detector concepts and applications such as in high energy physics and biomedical imaging applications.

Contents

List of Figures

List of Tables

List of symbols

b	Background rate
$B - L$	Baryon-Lepton
C	Capacitance
CE	Collection efficiency
d	Crystal pitch
dA	Cross-sectional area
dN	Number of incident particle
D	Dose
D_{cav}	Dose in the cavity
D_{med}	Dose in the medium
D_r	Detector ring diameter
$D_{T,R}$	Absorbed dose
ΔE	Energy resolution window
E	Particle energy
E_{eff}	Effective dose
E_{th}	Energy threshold
ϵ	Detection efficiency
$F(r, \theta)$	Anisotropy function
$FWHM$	Full width at half maximum
Φ	Particle fluence
$g_L(r)$	Radial dose function

G	Gain
$G_L(r, \theta)$	Geometric function
$G^{0\nu}$	Phase space factor
H_T	Equivalent dose
I	Transmitted photons
I_0	Number of incident photons
I_{SiPM}	SiPM output current
I_{PMT}	PMT output current
γ	Gamma
k	KERMA - Kinetic Energy Released per Unit of Mass
K	Scale factor
κ	Cherenkov angle
l	Length
λ	Wavelength
Λ	Dose rate constant in water
m	Mass
$m_{\beta\beta}$	Effective neutrino majorana mass
m_e	Electron mass
M	$\beta\beta$ isotope mass
$M^{0\nu}$	Transition nuclear matrix element
μ	Linear attenuation coefficient
n	Refractive index
N_{acc}	Accidental coincidences
$N_{\boldsymbol{fired}}$	Number of pixels fired
N_i	Incident photons
$N_{\boldsymbol{pixels}}$	Number of SiPM pixels
N_i	Incident photons

N_1, N_2	Background rates
p	Parallax error
PDE	Photon detection efficiency
$P_{avalanche}$	Probability of avalanche
$Q_{\beta\beta}$	Q-value for neutrinoless double beta decay
q_e	Elementary charge
QE	Quantum efficiency
QE_{PMT}	PMT quantum efficiency
Q_{out}	Total output charge
r	Distance
R	Radiation type
S	Photo sensitivity
$S(m_{\beta\beta})$	Sensitivity of a double beta decay to $m_{\beta\beta}$
t	Time
T	Tissue
$T^{0\nu}_{1/2}$	Half life of the 0ν
τ	Coincidence time window
θ	Angle between r and the long axis of the source
θ_0	Source transverse plane
U_{ei}	Elements of the neutrino mixing matrix
V_{br}	Breakdown voltage
V_{op}	Operation voltage
V_{in}	Input voltage
V_{out}	Output voltage
V_{ref}	Normalization constant
Ψ	Energy fluence
χ	Distance

List of Acronyms

ABS	American Brachytherapy Society
ADC	Analog to digital converter
APD	Avalanche photo-diode
BGO	Bismuth germinate
CCD	Charge-coupled device
CCM	Compact crystal matrix
C.L.	Confidence level
CM	Current-mirror
CP	Charge Parity
CT	Computed Tomography
DAC	Digital to analog converter
DCR	Dark count rate
DOI	Depth-of-interaction
EBS	Electronic brachytherapy source
EL	Electroluminescence
FOV	Field-of-View
FWHM	Full-width-at-half-maximum
HDR	High Dose Rate
IAEA	International Atomic Energy Agency
IBT	Ion Beam Therapy
IC	Integrated circuit

ICRP	International Commission on Radiological Protection
ICRU	International Commission on Radiation Units and Measurements
IFIC	Instituto de Física Corpuscular
IMRT	Intensity Modulated Radiation Therapy
ISRP	International System of Radiological Protection
KERMA	Kinetic Energy Released per Unit of Mass
LBNL	Lawrence Berkeley National Laboratory
LSC	Laboratorio Subterráneo de Canfranc
LED	Light Emitting Diode
LDR	LOW Dose Rate
LOR	Line of Response
LYSO	Lutetium-yttrium oxyorthosilicate
MC	Multi-clad
MCA	Multi channel analyzer
MRI	Magnetic Resonance Imaging
NEMO	Neutrino Ettore Majorana Observatory
NEXT	Neutrino Experiment with Xenon Time-projeciton-chamber
OSL	Optically Stimulated Luminescence
PCB	Printed Circuit Board
p.e.	Photo-electron
PET	Positron Emission Tomography
PID	Proportional–integral–derivative
POI	Point-of-interaction
POF	Plastic optical fiber
PMT	Photomultiplier Tube
PSF	Point spread function
PVT	Polyvinyl toluene

PTFE	Polytetrafluoroethylene (TEFLON)
RBE	Relative biological efficiency
RIS	Resonance Ionization Spectroscopy
RIA	Radiation Induced Attenuation
RMS	Root mean square
RF	Radio-frequency
RL	Radio-luminescence
SI	International System of Units
SiPM	Silicon Photomultiplier
SOF	Scintillating optical fiber
SPECT	Single-photon Emission Computed Tomography
TL	Thermoluminesce
TOF	Time-of-flight
TOF-PET	Time-of-flight Positron Emission Tomography
TPB	Tetraphenyl butadiene
UV	Ultraviolet
VUV	Vacuum ultraviolet
WL	Wavelength
WLS	Wavelength shifter
WSF	Wavelength Shifting fiber

Outline

The recent developments of solid-state photodetectors, namely with the silicon photomultipliers, allowed a proliferation of this technology through innumerous applications. These robust and versatile photosensors with an attractive price have become one of most promising alternatives for low light level detection, especially for applications where a large number of devices is required. Our group has been working with these devices in the last couple of years for applications in the medical field, obtaining some promising results.

The Silicon Photomultiplier (SiPM) recently became one of the most attractive photodetectors on the market. These multi-pixel photosensors, capable of single photon detection, are very versatile due to their high sensitivity, high gain, small size, insensibility to magnetic fields, easiness of optical couplings, low bias voltage and fast response, opening the possibility to apply this technology in multiple fields enabling a plethora of new detector concepts and applications such as in high energy physics and biomedical imaging applications. The capability of these devices to obtain at the same time photon-interaction and energy-information makes them a promising option.

This thesis is organized into two parts: Part I is related to the NEXT experiment for the Neutrinoless double beta ($0\nu\beta\beta$) decay search and Part II where two application studies are presented.

Part I is divided in three chapters, Chaper 1 describes the state-of-the-art of $0\nu\beta\beta$ decay experiments. Chapter 2 is related to the NEXT Time Projection Chamber (TPC) and the topological signature with SiPM tracking system and in the Chapter 3 experimental work developed within NEXT during this PhD is presented.

Part II comprises two chapters. Chapter 4 is related to the development and clinical studies of a dosimeter for real-time dosimetry in prostate brachytherapy. The last chapter, Chapter 5 presents the studies related to the development of a small PET scanner for didactical purposes.

Part I

Studies for the development of the NEXT tracking system

Chapter 1

Neutrinoless double beta decay search

1.1 Introduction

Postulated by Pauli in 1930, the neutrino conserved itself as mysterious particle until second half of XX century. Neutrinos are sometimes referred as ghostly particles due to their weak interaction being capable of crossing the entire Earth without any interaction. They are not affected by electromagnetic force once they are not electrically charged and as leptons won't be affected by the strong force that acts on particles inside the nuclei. The results from the Cowan–Reines neutrino experiment[1] leaded to the discovery of the antineutrino. Years later the muon neutrino was confirmed experimentally by Lederman, Schwartz and Steinberger[2].

Stars like the Sun are sources of these particles with reduced probability of interaction. The nuclear reaction in the Sun's core produce electron neutrino (ν_e) exclusively. In the Ray Davis Homestake experiment, in 1968, observations on solar neutrinos revealed intriguing results when 2/3 of the solar ν_e were missing (being known as the Solar Neutrino Problem). Decades later, the KamLAND Reactor observed more than one neutrino flavor originated from the sun. These results showed that this issue was due to neutrino oscillation in the path between the Sun and Earth, and the Homestake experiment wasn't capable to detect other type of neutrino besides the ν_e. While bosons are mediators of interactions, fermions are building blocks for matter. According to the Standard Model, neutrinos were believed to be massless particles. The study of solar neutrinos allowed to verify that neutrinos oscillate and do have mass. Massive neutrinos can be Dirac or Majorana particles. Majorana neutrinos and neutrinoless double beta ($0\nu\beta\beta$) decay violate lepton number conservation and the observation of $0\nu\beta\beta$ decay is enough to prove that neutrinos are Majorana particles, inform on their mass and shed light on Charge Parity (CP) violation. This can explain the

[1] Frederick Reines was honored by the Nobel Prize in 1995 for his work on neutrino physics

[2] 1988 Nobel Prize in Physics for the neutrino beam method and the demonstration of the doublet structure of the leptons through the discovery of the muon neutrino

matter and antimatter asymmetry through the *leptogenesis* mechanism.

1.2 Neutrinoless Double Beta Decay ($0\nu\beta\beta$)

Neutrino oscillation experiments clarified the deficit of upward going atmospheric muon neutrinos and have established that neutrinos have mass and mix. Neutrino oscillations are depending on mass (m) differences [2]:

$$\Delta m_{ij}^2 = m_j^2 - m_i^2 \tag{1.1}$$

Oscillations do not probe the absolute neutrino mass scale and the mass scale of the neutrinos is still unclear. Considering that neutrinos are massive, taking the Standard Model and no other physics, the $0\nu\beta\beta$ probes the neutrino mass. In particle and nuclear physics, besides the $0\nu\beta\beta$ the only remaining avenue is the tritium beta decay [3].

In double beta decay ($\beta\beta$), two neutrons of an atom simultaneously decay originating two protons conserving the electric charge with the emission of two electrons. This decay occurs in even-even nuclei (with even numbers of neutrons and protons), since these nuclei can be even more stable by the neutron conversion into protons, with the emission of two pairs of electrons and neutrinos. There are 35 potential natural-occurring double beta emitters. The two neutrino double beta ($2\nu\beta\beta$) (Eq. 1.2) decay has been observed in several nuclides with typical half-lives in the range of 10^{18}–10^{21} years, meaning that the single beta decay must be forbidden or highly suppressed by a large change in angular momentum [4].

$$(Z, A) \rightarrow (Z + 2, A) + 2e^- + 2\overline{\nu_e} \qquad (2\nu\beta\beta) \tag{1.2}$$

The $0\nu\beta\beta$ decay is possible if the annihilation of the two anti-neutrinos occurs. This represents a lepton violation by two (Figure 1.1, Eq. 1.3).

$$(Z, A) \rightarrow (Z + 2, A) + 2e^- \qquad (0\nu\beta\beta) \tag{1.3}$$

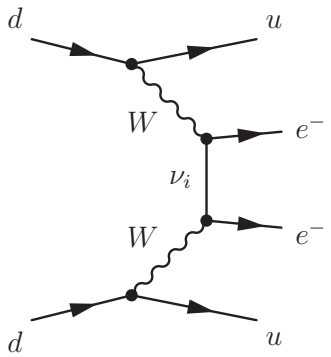

Figure 1.1: Feynman diagram leading to neutrinoless double beta decay [5].

Assuming the seesaw mechanism, if $B-L$ symmetry is verified it has to be spontaneously broken to give the neutrinos a nonzero mass. A third decay mode with a Majoron emission (χ), a massless Goldstone neutral boson that arise upon a global breakdown of baryon-lepton ($B-L$) symmetry, is also considered [6, 7]:

$$(Z, A) \rightarrow (Z+2, A) + 2e^- + N_\chi \qquad (0\nu\,\chi\beta\beta) \tag{1.4}$$

Considering that neutrinos are Majorana particles, $0\nu\beta\beta$ experiments would allow to determine the absolute neutrino mass. In that sense, the probability of $0\nu\beta\beta$ is related to the neutrino mass such that the bigger the neutrino mass, the higher the probability of $0\nu\beta\beta$. The $0\nu\beta\beta$ decay rate depends on the $\nu_e - \nu_e$ element of the neutrino mass matrix [8]. The effective Majorana mass of the electron neutrino is:

$$\langle m_{\beta\beta} \rangle = \left| \sum U_{ei}^2 m_{\nu i} \right| \tag{1.5}$$

where $m_{\nu i}$ are the small masses of the Majorana neutrinos and U_{ei} are the elements of the neutrino mixing matrix, the so called Pontecorvo-Maki-Nakagawa-Sakata (PMNS) mixing matrix [9]. Majorana neutrinos explain the smallness of neutrino masses, the so-called *seesaw* mechanism, and the measurement of the $0\nu\beta\beta$ decay rate provides direct information on neutrino masses.

The half-life of $0\nu\beta\beta$ is:

$$(T_{1/2}^{0\nu})^{-1} = G^{0\nu} \left| M^{0\nu} \right|^2 \left(\frac{m_{\beta\beta}}{m_e} \right)^2 \tag{1.6}$$

where $G^{0\nu}$ is the phase space, $M^{0\nu}$ is the nuclear matrix element of the transition and m_e is the electron mass [2, 10, 6].

In the $0\nu\beta\beta$ mode, the spectrum for the sum of the kinetic energies of the emitted electrons is a mono-energetic line at $Q_{\beta\beta}$, where Q is defined as the mass difference between the parent and daughter nuclide:

$$Q_{\beta\beta} \equiv M(A, Z) - M(A, Z+2) \tag{1.7}$$

In the $2\nu\beta\beta$ decay, the total kinetic energy of the two electrons is lower than the total available energy, while for the $0\nu\beta\beta$ the total kinetic energy of the two released electrons equals to the $Q_{\beta\beta}$ value of the decay. This makes it possible to experimentally distinguish these two processes (Figure 1.2). If neutrinos are Majorana particles, an energy scale at a level inversely proportional to the observed neutrino masses should be considered.

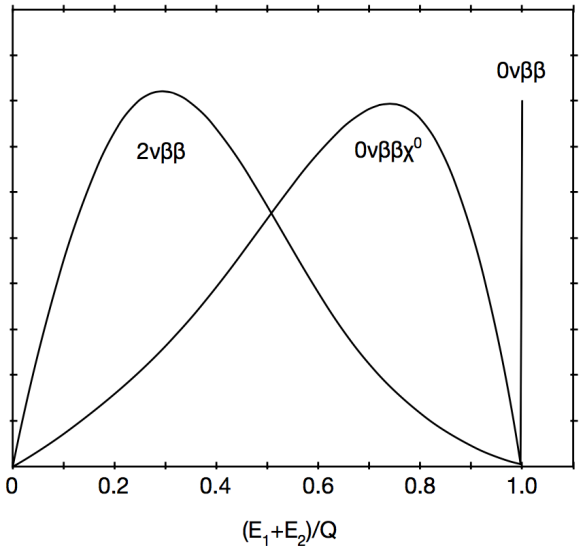

Figure 1.2: Spectra for the sum of the kinetic energies of the two emitted electrons in three different $\beta\beta$ modes: $2\nu\beta\beta$, $0\nu\beta\beta$ and $\beta\beta$ decay with Majoron emission (χ^0) (arbitrary amplitudes) [10].

1.3 Absolute scale of neutrino masses

If the neutrino is a Majorana particle it means that it is its own antiparticle and the $0\nu\beta\beta$-decay, a Standard Model forbidden process, is possible in some isotopes, including ^{136}Xe. Besides giving an experimental proof of the Majorana nature of neutrinos, the measurement of the decay's half-time would allow the absolute scale of neutrino masses, a demanding and essential task in the understanding of these particles. The only emitted products in this process are two electrons, which can only occur if the neutrino and antineutrino are the same particle (i.e. Majorana neutrinos), so the same neutrino can be emitted and absorbed within the nucleus. There are three types of neutrino with different flavors: electron neutrino (ν_e), muon neutrino (ν_μ) and tau neutrino (ν_τ). In the case of three-neutrino mixing, two neutrino mass spectra are possible [11]:

(1) Normal spectrum (NS)

$$m1 < m2 < m3; \quad \Delta m^2_{12} << \Delta m^2_{23} \tag{1.8}$$

(2) Inverted spectrum (IS)

$$m3 < m1 < m2; \quad \Delta m^2_{12} << \Delta m^2_{13} \tag{1.9}$$

The absolute value of neutrinos masses would be solved by the experimental observation of neutrinoless double beta decay. One could constraint the allowed patterns of neutrino masses by plotting the values of the masses as functions of the unknown lightest mass m_{light} [5] (Figure 1.3). The next generation of $0\nu\beta\beta$ decay experiments will probe the inverted mass hierarchy region, in which $|m_{\beta\beta}| \sim(2 - 5)\times10^{-2}$ eV.

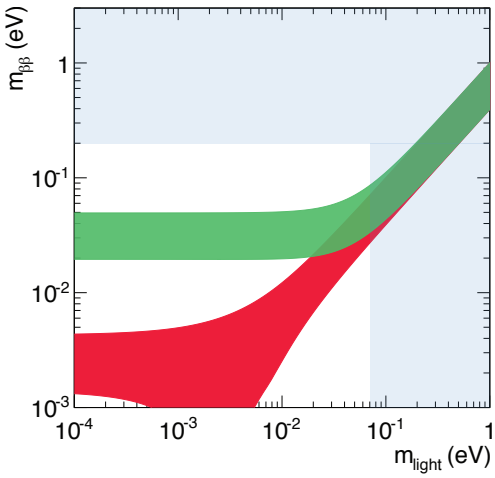

Figure 1.3: The normal hierarchy (red) and inverted hierarchy (green) possible for neutrino masses as a function of the lightest neutrino mass. The identified regions came from experimental bound on the half-life of the $0\nu\beta\beta$ decay. From [12].

1.4 Neutrinoless Double Beta Decay Experiments

As described by Cremonesi [6], the essential criteria in a $0\nu\beta\beta$ experiment are a good energy resolution, time stability, capable to obtain energy and topology information, low maintenance due to the long underground running times, large isotope mass and effective background suppression strategy. The extremely low rates expected impose underground operation for the development of specific background rejection techniques [8]. The sensitivity of any $0\nu\beta\beta$ experiment is deeply related to crucial parameters such as low background rate, energy resolution and detection efficiency, exposure and source/isotope [10]. The highest sensitivity to small Majorana neutrino masses can be reached in experiments on the search of the L-violating $0\nu\beta\beta$ decay process [5].

As pointed by Cadenas and Martin-Albo [10], a high energy resolution is the only protection against the intrinsic $2\nu\beta\beta$ brackground and improves signal-to-noise ratio at $Q_{\beta\beta}$. An experiment with poor energy resolution would require optimum background rejection and high exposure [10]. The sensitivity to the effective Majorana mass of the electron neutrino ($m_{\beta\beta}$) is a figure of merit used to compare between $0\nu\beta\beta$ decay experiments. Considering the trend for $0\nu\beta\beta$ experiments seeking the inverted hierarchy regions, hundred kilos or tonnes of isotopes are needed. To increase $m_{\beta\beta}$, isotope mass can be increased. Although, for the same background, the mass must increase by a factor of 4 to obtain the same increase in $m_{\beta\beta}$ sensitivity has doubling its efficiency [10], since:

$$S(m_{\beta\beta}) = A'\sqrt{1/\epsilon}\left(\frac{b.\Delta E}{M.t}\right)^{1/4} \tag{1.10}$$

where ϵ is the detection efficiency, ΔE the energy resolution window where the $0\nu\beta\beta$ will be reconstructed, b is the background rate, M the $\beta\beta$ isotope mass and t the data-taking time

[13].

The best isotope option for $\beta\beta$ experiments should have high natural occurrence, thus reducing cost, avoiding expensive enrichment processes. A high Q-value ($Q_{\beta\beta}$) and low $2\nu\beta\beta$ background are ideal. The Q-value has a practical contribution to both background and sensitivity by affecting the phase space factor $G^{0\nu}$ (Eq. 1.6) which varies as $Q^5_{\beta\beta}$ (Eq. 1.7) [14]. The isotope choice usually is such that $Q_{\beta\beta} > 2$ MeV, restricting the 35 naturally occurring isotopes $\beta\beta$-emitters to a group of nine. High Q-values larger than energies of natural gamma backgrounds (up to 2615 keV) reduces background. High Q-values and large nuclear matrix elements enhance the expected number of $0\nu\beta\beta$ decay events because the phase space factor scales as Q^5 and $|M^2|$. There are two approaches for reducing the radioactive budget of a $0\nu\beta\beta$ experiment to very low levels: the use of radiopure components, with low contents of uranium and/or thorium, and shielding. All the $0\nu\beta\beta$ experiments use a formula that combines both recipes, but of course, no experiment achieves a null radioactive budget. Therefore, resolution and possibly other handles are a must to suppress both intrinsic (e.g. the $2\nu\beta\beta$ channel) and external backgrounds. Considering that the background severely limits the sensitivity of a $0\nu\beta\beta$ experiment, a high detection efficiency is crucial.

In summary, an ideal $0\nu\beta\beta$ decay search experiment is characterized by:

1. An arbitrarily large mass of sensitive, 100% enriched target, e.g. target and detector are the same, reconstruction efficiency of the signal is one.
2. An arbitrarily small radioactive budget (thus, not affected by external backgrounds).
3. Perfect resolution, necessary to separate the $0\nu\beta\beta$ and $\beta\beta2\nu$ spectra.

1.4.1 State-of-the-art of $0\nu\beta\beta$-decay experiments

Numerous experiments have been carried out to search for neutrinoless double-beta decay. The next near-future $0\nu\beta\beta$ decay search milestone is to reach a sensitivity of $\langle m_{\beta\beta}\rangle \sim 20$ meV which covers the inverted neutrino mass hierarchy [15]. Most of the $0\nu\beta\beta$ experiments had been proposed in late 90's and still there's no proof of this rare event. The main contribution for $0\nu\beta\beta$ decay search are the GERDA and Majorana germanium calorimeters, CUORE bolometers and EXO, combining self-shielding with good event fiducialization [13].

The next generation of $0\nu\beta\beta$ experiments in the tonne-scale with low backgrounds will explore the inverted-hierarchy region. This may enlighten the neutrino mass question and together with CP-violation could help to clarify why matter dominates over antimatter in our Universe [6]. The second and third generations of double beta decay experiments using large strength source of enriched $\beta\beta$ emitter material were proposed at the beginning of the 90's. Even if neutrinoless double beta decay is observed in next generation experiments we nevertheless will not be able to decide from beta decay experiments alone whether the mass hierarchy is normal or inverted [16].

Heidelberg-Moscow experiment

The Heidelberg-Moscow experiment is a German-Russian collaboration which firstly claimed the observation of $0\nu\beta\beta$ decay in ^{76}Ge [17–22]. The experiment was initially proposed in 1987 and started operation at Gran Sasso Underground Laboratory in 1990. The collaboration uses an active detector (source and detector are the same) operating with 11 kg of enriched ^{76}Ge running the detector from 1990 to 2003. The observation of $0\nu\beta\beta$ has been criticized due to the simple statistical analysis of the measured spectra and poor statistics [23]. By combining results from Heidelberg-Moscow and IGEX experiments, in 2001, Zdesenko *et al* [23] established the half-life limit on the $0\nu\beta\beta$ decay of ^{76}Ge:

$$(T^{0\nu}_{1/2}) = 2.5(4.2) \times 10^{25} \tag{1.11}$$

at 90% (68%) C.L., corresponding to the Majorana neutrino mass of $(m_{\beta\beta}) = 0.3(0.2)$ eV [23]. New generations of $0\nu\beta\beta$ experiments such as GERDA, EXO-200 and KamLAND-Zen allowed to refute the Heidelberg-Moscow claim on the observation of $0\nu\beta\beta$ decay. This new generation of $0\nu\beta\beta$ decay experiments are described below.

GERDA experiment

Located at *Laboratori Nazionali del Gran Sasso* the GERmanium Detector Array (GERDA) experiment as been proposed in 2004 and the Phase I was completed in 2013. The second phase experiment is under commissioning. GERDA is searching for $0\nu\beta\beta$ with bare germanium detectors enriched by ^{76}Ge, submerged into high-purity liquid argon (LAr), a 70 m^3 cryostat inside a 650 m^3 water tank. Bare Ge detectors allow to decrease background from the surrounding materials, liquid argon shields from the radiation and cools down the Ge detectors.

From Phase I, GERDA set limit on $0\nu\beta\beta$ decay half-life $T^{0\nu}_{1/2}$ >2.1×10^{25} yr (90 % C.L.) and limit on effective neutrino mass $m_{\beta\beta} < 0.2 - 0.4$ eV (90% C.L.).

Gerda Phase II expect a background at $Q_{\beta\beta}$ of 10^{-3} counts / (keV.kg.yr) and an expected sensitivity of $T^{0\nu}_{1/2}$ ~1.4 × 10^{26} yr, $m_{\beta\beta}$ ~0.1 eV.

New BeGe detectors for GERDA Phase II provide better energy resolution (FWHM up to 1.6 keV at 1.3 MeV in a vacuum cryostat) and better Pulse Shape Discrimination.

Recent measurements with BeGe detector inside LArGe test facility show very good suppression of background. The goal of Phase II background index of $< 10^{-3}$ cts/(keV × kg × yr).

Majorana Demonstrator

The Majorana Demonstrator aims to demonstrate the feasibility of a tonne-scale ^{76}Ge array detector for $0\nu\beta\beta$ search. The experiment will be constructed at Sanford Underground Research Facility (South Dakota, USA). The 40 kg ^{76}Ge detector comprises an array of

detectors with 30 kg enriched to 86% ^{76}Ge (Figure 1.4). The collaboration aims to achieve a background rate in the $0\nu\beta\beta$ region of interest of no more than 3 counts per tonne of target isotope per year [1] and determine whether a future 1-tonne experiment can achieve a background goal of one count per tonne-year in a 4-keV region of interest around ^{76}Ge $0\nu\beta\beta$ Q-value at 2039 keV.

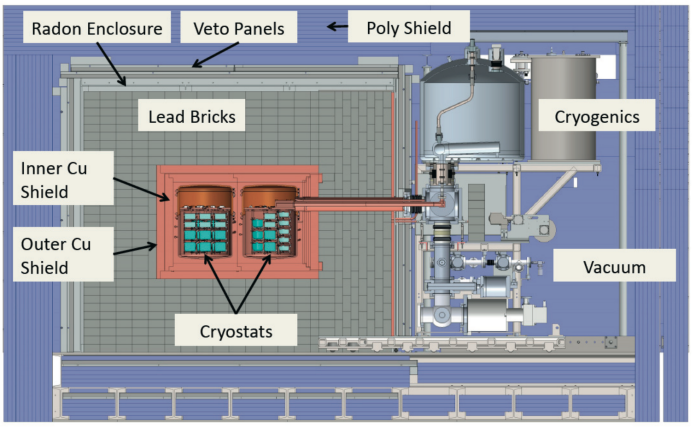

Figure 1.4: Majorana demonstrator illustration [1].

SNO+

SNO+ is a multi-purpose Neutrino Physics experiment under construction at VALE's Creighton mine in Sudbury (Ontario, Canada). Besides the search for $0\nu\beta\beta$ it is intended to investigate neutrino-matter couplings, search for non-standard modes of nucleon decay, study terrestrial neutrinos and supernova neutrinos [24]. Succeeding the SNO experiment by replacing heavy water with ∼800 ton liquid scintillator (linear alkylbenzene with 2,5-diphenyloxazole (PPO) primary fluor) loaded with ^{130}Te held in a 12 m acrylic vessel and ∼10000 PMTs held in a support structure inherited by the SNO experiment. These structures are immersed in 7000 tonnes of ultra-pure water, shielding the scintillator volume from background radiation. Difficulties in Te loading into scintillator obliged to the addition of water which increases the U/Th context of the mixture affecting background but still low enough to allow the use of Bi-Po tagging to reduce associated backgrounds to insignificant levels [24]. The demonstrator experiment will have 0.3% Te, expecting to reach sensitivity approaching the top of the inverted neutrino mass hierarchy, for a 3 to 5 year run [24]. Perspectives for improvement are related to the optimization regarding PMT efficiency (currently ∼15%), increasing effective photocathode coverage (currently ∼ 50%), reducing external background from the acrylic vessel and increasing fiducial volume (currently ∼200 tonnes), full cavity volume of ∼7 kt).

NEMO-3

The Neutrino Ettore Majorana Observatory (NEMO) collaboration started in 1989. The concept behinds NEMO is the use of several isotopes in the form of thin foils. The detectors placed on both sides of the foil are able to detect electrons and positrons emitted in the double beta decay. Three prototype detectors (NEMO 1, 2 and 3) have been built and used until 1997 and NEMO-3 finished operation in 2011. In NEMO-3, 7 isotopes (^{48}Ca, ^{82}Se, ^{96}Zr, ^{100}Mo, ^{116}Cd, ^{130}Te and ^{150}Nd) were investigated, obtaining their half-life (energy and angular distributions were measured) and the strong limits on decays with Majoron emission. No evidence of both $0\nu\beta\beta$ and Majoron emission $0\nu\beta\chi^0\beta$ was found [25]. Data collected allow to set strong limits on 0ν decay of ^{82}Se, ^{96}Zr, ^{100}Mo and ^{150}Nd.

The NEMO experiment allows both energy and topology detection (Figure 1.5). The tracking consisted of 8000 drift chambers operating in Geiger Mode. The calorimeter was made of 2000 plastic scintillators coupled to low-radioactivity PMTs. In addition, a small magnetic field of 10^{-1} T allows identification of the electron signal [26]. Data with 7 kg of ^{100}Mo in 4.5 years of data set a limit on the half-life of $T_{1/2} < 1 \times 10^{24}$ corresponding to a neutrino mass limit of $m_v < 0.3 - 0.9$ eV.

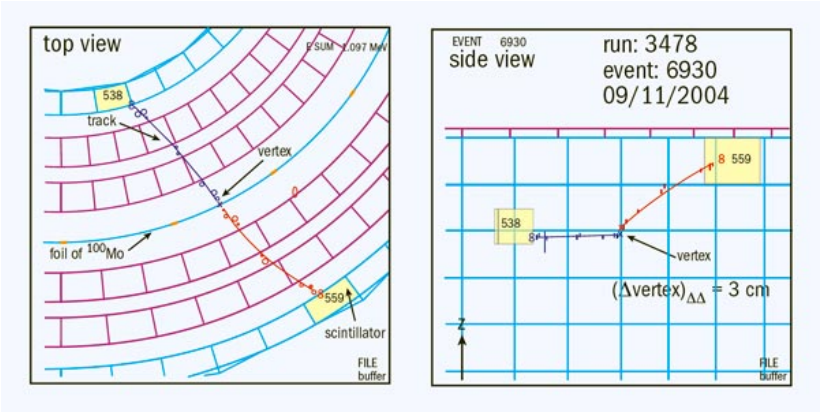

Figure 1.5: Top and side view of a typical $\beta\beta$ event in NEMO-3 [26].

The SuperNEMO experiment prospects housing 100 kg of isotope, ten times larger than NEMO-3, expecting a neutrino mass around 50 meV. For background suppression the $0\nu\beta\beta$ topological signature will be measured together with the energy of the $\beta\beta$ decay. The installation of a first module (using ^{82}Se) at the Modane Underground Laboratory is under way, with data taking expected in the second half of 2015. From all new generations of $0\nu\beta\beta$ experiments, SuperNEMO is the only experiment that can use many isotopes.

COBRA

The Cadmium Zinc Telluride 0-Neutrino Double-Beta Research Apparatus (COBRA) experiment comprises monolithic, calorimetric ^{116}Cd (Q-value of 2814 keV) array of Cadmium-Zinc-Telluride semiconductor detectors in a coplanar grid design [27]. The large-

scale experiment predicts using 11000 detectors, which corresponds to a total detector mass of roughly 400 kg [27]. For a 90% enrichment in ^{116}Cd is estimated an energy resolution of better than 1.5% (FWHM) and a background rate of less than 0.5×10^{-3} counts/keV/kg/yr, reaching a sensitivity to effective Marojana neutrino mass of less than 50 meV and a ^{116}Cd half-life sensitivity of 1.0 - 3.5 $\times10^{26}$ [27].

CUORE

The Cryogenic Underground Observatory for Rare Events (CUORE) located at Gran Sasso National Laboratory (Italy), is a tightly packed array of 988 TeO_2 crystals in bolometer modules ranged in 19 towers of 13 layers each with 4 crystals, each bolometer $5 \times 5 \times 5$ cm^3 and 750 g, for a total mass of 741 kg of TeO_2 with 204 kg of ^{130}Te [28]. The detector is cooled to $\sim$ 10 mK. In a proof of concept experiment, CUORICINO, was obtained a 90% C.L. lower limit of 3.0×10^{24} yr on the ^{130}Te lifetime for $0\nu\beta\beta$ decay [28].

The CUORE prototype version, the CUORE-0, comprises a single tower of 52 bolometers and started operation in spring 2013 [29]. Operating from March 2013 to May 2014, the total exposure is $\sim$18.1 kg.yr. The CUORE-0 achieved a background reduction of factor 6 in the α region and a factor of 2 in the γ region compared to CUORICINO. The CUORE-0 $0\nu\beta\beta$ signal region is blinded [29]. The CUORE-0 background is dominated by the γ from the cryostat, the α background is 0.019 ± 0.002 counts/(keV.kg.yr) [30]. CUORE is expected to reach a $0\nu\beta\beta$ ^{130}Te half-life sensitivity of 1×10^{26} yr [31].

KamLAND-Zen

Built at Kamioka Obervatory (Toyama, Japan), the KamLAND detector designed for electron neutrino detection is running since 2002. The KamLAND-Zen experiment started in 2011. The detector consists in of a onion like design, comprising several concentric spherical shells. The phase-2 detector used 320 kg of 91% enriched ^{136}Xe dissolved in 13 ton liquid organic scintillator placed in the inner balloon of the detector. Phase-2 had 383 kg of Xe. This 3 m diameter mini-balloon is surrounded by a 13-meter diameter spherical balloon with 1 kton liquid scintillator made of 135 μm thick transparent film. This balloon is suspended in 18-meter stainless steel tank containing a buffer oil because the film is too thin to support the 1000-ton of liquid. The space between the detector and the cavity walls is filled by a pure water layer that absorbs the radioactivity coming from the walls and moderating the fast neutrons produced by cosmic rays in the rock. This layer is equipped with 255 20-inch PMTs for detection of cosmic-ray muons traversing the detector.

Recently the KamLAND-Zen collaboration published a lower limit for the $0\nu\beta\beta$ decay half-live of $T^{0\nu}_{1/2}>1.1\times10^{26}$ yr (90% C.L.), corresponding to a Majorana neutrino mass upper limit in the range $60 - 161$ meV (Figure 1.6). The Figure 1.6 right-panel shows the corresponding limits for each nucleus as a function of the mass number [32].

With 1 ton of enriched xenon, brighter scintillator, high quantum efficiency PMTs and by introducing light collective mirrors, the KamLAND2-Zen aims to cover inverted hierarchy

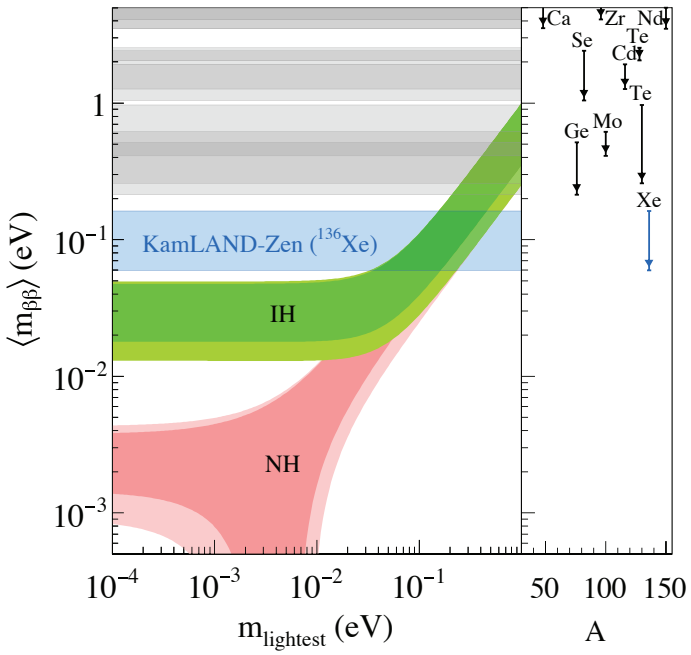

Figure 1.6: $\langle m_{\beta\beta} \rangle$ as a function of the lightest neutrino mass with new limits provided by KamLAND-Zen collaboration [32].

by improving energy resolution against $2\nu\beta\beta$ background, to < 2.5 % at the Q-value of ^{136}Xe $\beta\beta$ decay, targeting a 20 meV sensitivity in a 5 year measurement [15].

EXO-200

The EXO–200 (Enriched Xenon Observatory) consists of 175 kg of liquid Xenon enriched to 80.6% in ^{136}Xe housed in a double Time Projection Chamber (TPC). The liquid vessel allows 110 kg in the active volume of the detector (Figure 1.7). The TPC with liquid xenon operates at 167 K and 147 kPa (Xe density of 3.0 g/cm^3). EXO-200 aims to achieve a sensitivity close to 100 meV for Majorana neutrino masses [4]. An extended version with 1 ton capable to perform Ba^+ tagging is planned, allowing a very low background of about 10^{-4} counts/(kg keV yr) [11]. Although the 2ν contribution to the background remains, the energy resolution at $\beta\beta$-decay Q-value of 2457.8 keV is largely improved by reading both ionization and scintillation signals. EXO–200 has recently claimed the first observation of $2\nu\beta\beta$ in ^{136}Xe ($Q\beta\beta = 2457.8$ keV) [25].

In [33], the collaboration reported a 90% confidence level lower limit on the $0\nu\beta\beta$ half-life of 1.1×10^{25} yr, corresponding to an upper limit on the Majorana neutrino mass of 190-450 meV.

NEXT

The Neutrino Experiment with ^{136}Xe Time-projection-chamber (NEXT), at Canfranc Underground Laboratory (LSC), Spain, will search for $0\nu\beta\beta$ decay in ^{136}Xe using a

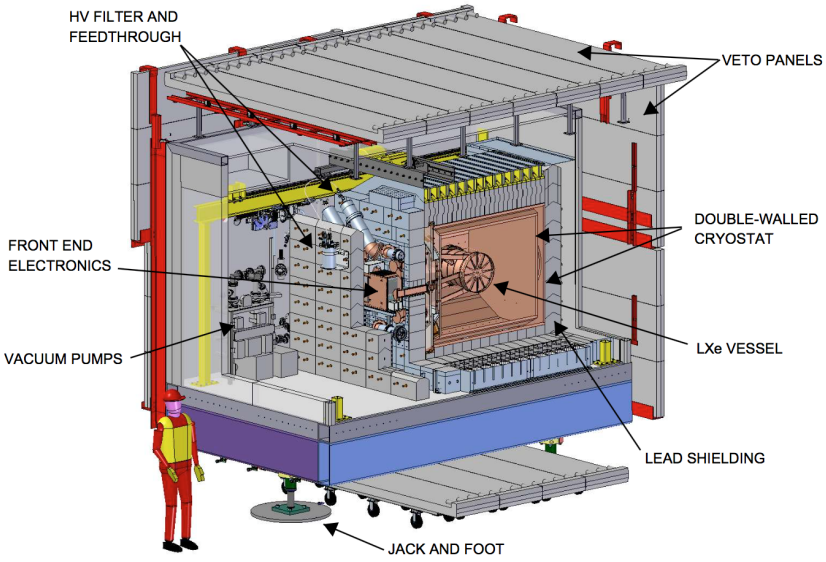

Figure 1.7: Cutaway view of the EXO-200, with the primary sub-assemblies identified [4].

High-Pressure Gaseous Xenon Time-Projection Chamber [34]. This detector allows both calorimetry and tracking with dedicated readouts and provides a fully active volume detector. The initial NEXT prototypes, the NEXT-DEMO and NEXT-DBDM, are small scale detectors with 1 kg of natural xenon at 10-15 bar. Extrapolation form energy resolution measurements show a 0.74% and 0.5% FWHM for NEXT-DEMO [35] and NEXT-DBDM [36], respectively. The NEXT-100 is a TPC with 100 kg of gaseous xenon with commissioning at LSC by 2017. NEW is a 1:2 scale detector from NEXT-100 with 10 kg of xenon and is under commissioning at the LSC. NEXT detectors are summarized in Chapter 2.

1.4.2 Barium tagging and the tonne-scale $0\nu\beta\beta$ experiments

The next generation of $0\nu\beta\beta$ decay experiments will be searching the full inverted hierarchy of neutrino masses, seeking sensitivities of Majorana neutrino mass of 20 meV. This will require isotope masses in the *ton* scale. For these big scale experiments, the biggest challenge is to achieve a high background suppression, up to some counts per *tonne-year*. The technology of the NEXT-100 time-projection-chamber, with both energy and tracking capability, can be extrapolated for the next generation of $0\nu\beta\beta$ decay experiments with fiducial masses in the *tonne*-scale. To scale to this masses, at 20 bar a 10 m^3 vessel would be required.

The identification both barium daughter atom (Ba^{++}) in the decay $^{136}Xe \rightarrow Ba + 2e^-$ and the two emitted electrons would allow full background rejection and identification of a $0\nu\beta\beta$ event. A future generation of EXO-200 is the nEXO experiment, a 5-ton liquid Xe TPC capable to recover barium decay product by surface adsorption and it's identification by Resonance Ionization Spectroscopy (RIS), allowing a background-free measurement of neutrinoless double-beta decay and increase the half-life sensitivity of the experiment by at

least one order of magnitude [37]. The ^{136}Ba has been suggest by Moe [38] and currently investigated by EXO collaboration [37, 39, 40]. A basic principle was investigated by Mong [39], consisting in the capture of the ^{136}Ba daughter at the tip of a fiber optic probe by freezing a sample of xenon capable to contain the barium ion. In concept, the barium ion would the trapped at the tip of the probe in the solid xenon ice by the application of electric fields. The identification of the barium ion might by achieved by tagging the ion or atom by laser induced fluorescence. While for the Ba^{2+} the expected emission would be in the extreme ultraviolet, around 75 nm, making it difficult to detect, the irradiation of the Ba^{+} ion with blue-green at 493 nm would lead to red fluorescence at ∼650 nm [38, 41].

Summary

Double beta decay experiments can address the Majorana or Dirac nature of the neutrino. If neutrinos are Majorana particles, the neutrino is it's own anti-particle. These experiments allow to know the absolute scale of neutrino masses, normal or inverse mass hierarchy and CP violation in leptonic sector. The leptonic decay of massive Majorana neutrinos would explain leptogenesis.

The NEXT experiment is one of the late runners on the race to search for $0\nu\beta\beta$ decay. It has several key features such good energy resolution and low background rates with the possibility of scalability to ton-scale [10]. This putts the NEXT experiment side-by-side with other ongoing projects. Two main aspects are crucial for the NEXT-100, first to achieve good signal detection efficiency and second to achieve optimal background rejection most importantly at $Q_{\beta\beta}$. The main sources of background are natural occurring high-energy gamma rays from detector materials (mainly ^{208}Tl and ^{214}Bi) and surroundings, airborne radon, muons and neutrons. Further analysis on this issue is found in [12]. For NEXT-100, an energy resolution close to 0.5% FWHM at 2.5 MeV is predicted.

Chapter 2

The NEXT TPC topological signature with a SiPM tracking System

2.1 Physics potential of NEXT

The Time Projection Chamber (TPC) was initially proposed by David Nygren in the late 1970s. This particle detector consists in a gas-filled chamber with an electric field applied over the volume, providing position-sensitive electron collection.

As detector medium, xenon provides both primary scintillation signal that can be used to establish event triggering and ionization signal usable for calorimetry and tracking [42, 43]. Gaseous xenon presents a low Fano factor and W-value allowing a good intrinsic limit on the energy resolution, 0.3% full width at half maximum (FWHM) at $Q_{\beta\beta}$ ($\sim$2500 keV) in addition to a slow two-neutrino mode (2×10^{21} yr). Besides an improved resolution, gaseous xenon provides long attenuation length for high-energy gammas (>3 m) and allows event topology information. When high pressure ^{136}Xe emits two electrons they propagate in the medium ionizing and exciting its atoms, causing the prompt emission of vacuum ultraviolet (VUV) scintillation light of 172 nm that lasts $10-30$ ns [36].

The NEXT TPC comprises two main readout systems for calorimetry and for tracking. On the cathode side (Figure 2.1), a Photomultiplier Tube (PMT) plane allows both signaling the *start-of-event* (t_0) by measuring the primary scintillation signal (S1) and energy measurement by the detection of a fraction of the secondary scintillation (S2) light, providing a precise measurement of the total energy deposited in the gas [42]. On the anode side a panel with Silicon Photomultipliers (SiPMs) detects the same S2 signal, allowing topological signature recognition.

In the NEXT TPC (Figure 2.1) the ionization electrons, when prevented ongoing recombination by a moderate electric field ($\sim 0.3-0.5$ kV/cm), will drift into the anode (with a velocity around $\sim$1 mm/μs) and are subjected to a higher intensity electric field ($2-3$

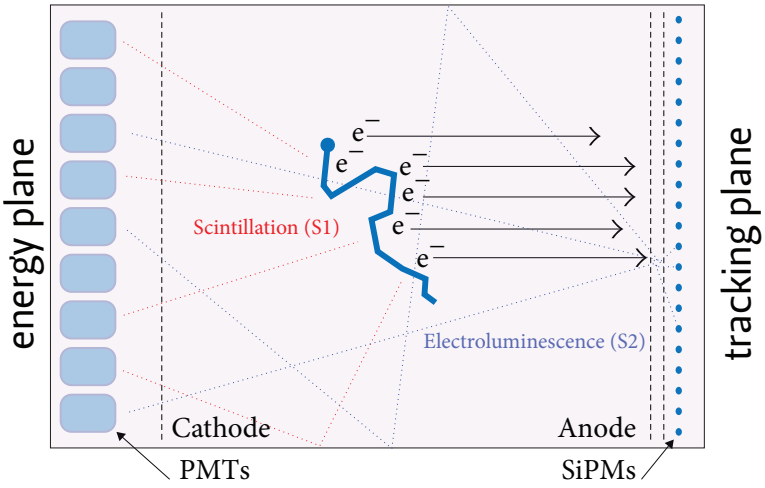

Figure 2.1: NEXT TPC with PMT plane at the cathode and SiPM plane on the anode [34].

kV cm^{-1}bar^{-1}) capable to excite Xe atoms without ionizing thus generating isotropic VUV photons by electroluminescence (EL) [12, 34]. The NEXT-100 addresses two major features, both energy resolution better than 1% at Q value of ^{136}Xe and topological signature for signal identification and background rejection [34]. The granularity and detection efficiency provided by the light tracking system will be major contributions for background suppression and at the same time for particle event identification. As a result, the background rate is expected to be one of the lowest of the new generation of $0\nu\beta\beta$ experiments, placing the NEXT experiment in good position in the $0\nu\beta\beta$ race.

2.2 $0\nu\beta\beta$ topological signature in NEXT

In gaseous xenon at 10 bar, $0\nu\beta\beta$ events present a distinctive topological signature in the form of a Brownian-like continuous ionization track, 30 cm long and with two energy blobs at each end corresponding to the larger energy deposition from the two stopping electrons, about 20% of the event energy shared by the two blobs [10, 34, 44]. This blob is a result of multiple scattering where ~300 keV is deposited in a short path. The continuous track connecting the two blobs is a minimum ionizing particle (MIP)-like region with dE/dx ~70 keVcm^{-1}. The emission of delta electrons and bremsstrahlung photons and the diffusion of the electron cloud during drift are the main physical effects to consider regarding the topological signature identification [45]. The ^{208}Tl and ^{214}Bi (isotopes of the progeny of ^{232}Th and ^{238}U) present gamma lines at 2.615 MeV and 2.448 MeV, respectively, strongly contributing for background due to the probability of generating a signal-like track in the fiducial volume with energy $\sim Q_{\beta\beta}$ [46]. For NEXT, at 15 bar the $0\nu\beta\beta$ topological signature is expected as a single track ~15 cm long [44]. The expected $0\nu\beta\beta$ decay topological signature is shown in Figure 2.2, from Monte Carlo simulation of a $0\nu\beta\beta$ event and a single electron

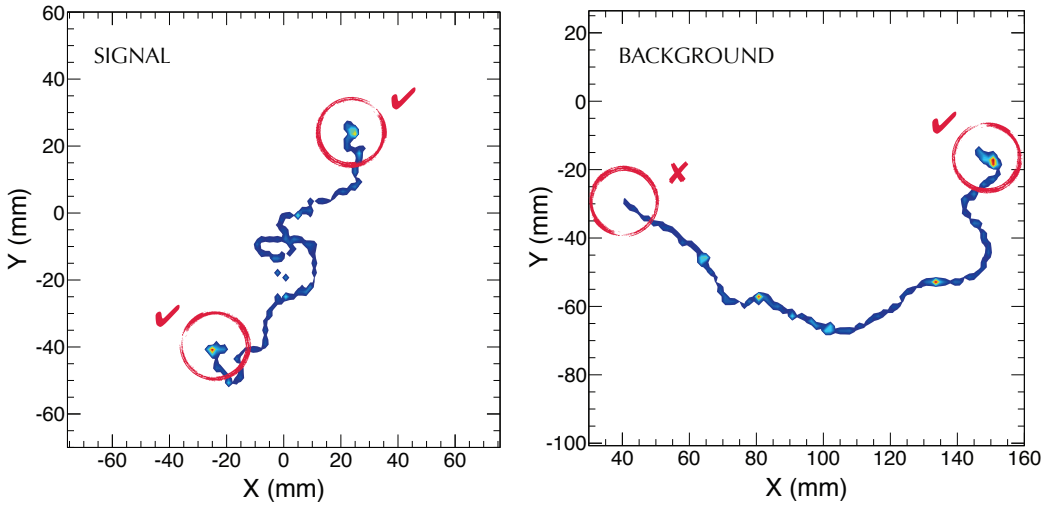

Figure 2.2: Monte Carlo simulation of a $0\nu\beta\beta$ event (left) and a single electron background event from a 2.44 MeV ^{214}Bi gamma (right) at 15 bar [44].

background event from a 2.44 MeV ^{214}Bi gamma at 15 bar [44]. For single electrons, one should observe a single blob from high energy deposition at one end of their track, allowing to identify these background tracks (Figure 2.2, right).

The NEXT tracking plane is located behind a transparent EL grid and comprehends several Dice Boards (DBs) with 8×8 SiPMs distributed with a pitch of 1.1 cm [34, 13]. This pitch is a compromise due to several constraints related to the detector physics, namely: in a dense gas a moving electron doesn't behave exactly as a MIP, losing significant part of its energy by the emission of discreet delta rays and bremsstrahlung radiation; typical rms of the charge distribution for electrons produced in the center of the chamber is of the order of 1 cm; as the pitch increases, the background rejection capability decrease due to constraints in the identification of low-energy photons (e.g. 35 keV X-rays) nearby the electron track [34].

2.3 NEXT experiment roadmap

In an initial proof-of-concept phase (2009-2014), the NEXT collaboration constructed two scaled version of detectors, the NEXT-DEMO and NEXT-DBDM.

The NEXT-DBDM is a TPC prototype with 1 kg high pressure xenon gas developed by the *Lawrence Berkeley National Laboratory* (LBNL) group for NEXT. The purpose of NEXT-DBDM was the demonstration of near-intrinsic energy resolution [36]. The prototype had a cylindrical fiducial volume with 16 cm diameter and 16 cm length. The energy plane was equipped with 19 R7378A PMTs (Hamamatsu). Energy resolutions of ∼1% FWHM for ^{137}Cs 662 keV gamma rays were obtained at 10 and 15 atm and ∼5% FWHM for 30 keV fluorescence xenon X-rays, demonstrating the feasibility of 0.5% FWHM energy resolution at the ^{136}Xe double beta Q-value (2.48 MeV) with 3D tracking capabilities [36, 47].

The NEXT-DEMO, operated at *Instituto de Física Corpuscular* (IFIC) in Valencia (Spain), provided the validation of the NEXT-100 design, meaning the evaluation of the energy resolution in large active volumes, reconstruction of the topological electron signature in a high-pressure xenon chamber, test long drift lengths and high voltages, understand gas recirculation and purification in large volumes and understand light collection using wavelengths shifters (WLS) [42].

Beginning 2016, NEXT-White[1] (or NEW) started commissioning at *Laboratorio Subterráneo de Canfranc* (LSC).

In the following sections, the tracking plane of the several NEXT detectors is described.

2.3.1 NEXT-DEMO prototype

The NEXT-DEMO detector (Figure 2.3) is a prototype with ∼1.5 kg of natural xenon at 10 bar in a 60 cm long pressure vessel with 30 cm diameter. The DEMO detector characterizes by comprising both energy and tracking plane, having two active regions, a 30 cm long drift region between the cathode and the gate with a typical drift field of 500 V.cm^{-1} and a 0.5 cm long electroluminescence (EL) region between the gate and the anode. A set of six panels made of polytetrafluoroethylene (PTFE/Teflon) coated with tetraphenyl butadiene (TPB) mounted inside the electric field cage form a light tube of hexagonal cross section [45]. The energy plane comprises 19 1-inch Hamamatsu R7378A PMTs, with a photocathode coverage of the energy plane of about 39%. Degradation of photocathode detection efficiency has been observed in NEXT-DEMO [35], due to direct exposure to xenon ultraviolet (UV) scintillation light.

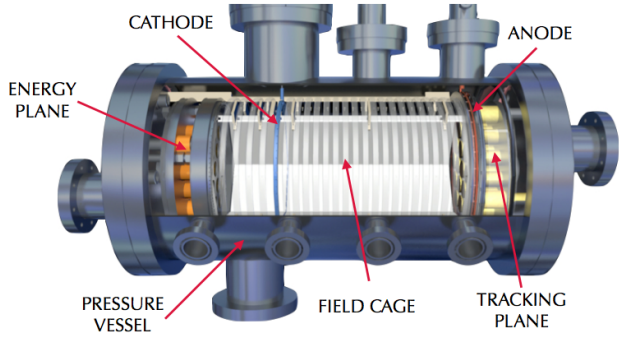

Figure 2.3: Cross-section drawing of the NEXT-DEMO detector with all major parts labeled [42].

The tracking plane is an array of 256 Hamamatsu S10362-11-050P SiPMs, distributed into 4 boards, 64 photodetectors per board with a 1 cm pitch and sharing the bias voltage (Figure 2.4). For an operation voltage of 73 V, these SiPMs have a gain of $\sim 7.5\times10^5$ at room temperature and a dark current of $0.2 - 0.3$ photoelectrons per μs [45]. The SiPM boards

[1] in memory of James White

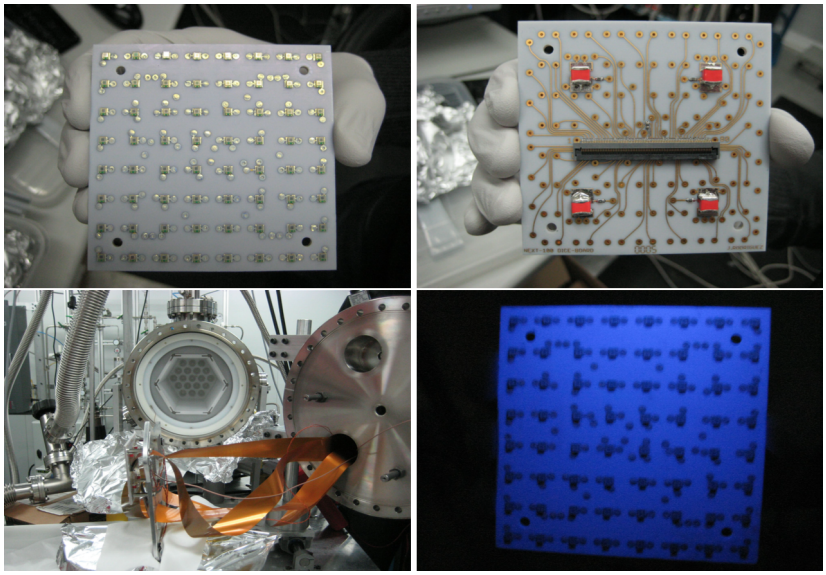

Figure 2.4: SiPM boards for NEXT-DEMO. The SiPMs are mounted on multilayer printed-circuit-boards (PCBs) of PTFE substrate with copper layers, gold plated. Four tantalum capacitors per board reduce detector dead time and maintain the nominal supply voltage [45].

are 2 mm behind the EL production region. Each SiPM has a 1 mm^2 active area of 50 μm cells. The SiPM coating with a WLS material allows the increase of VUV light detection, since at the short wavelength of xenon emission of ∼173 nm the SiPM quantum efficiency is very low. The peak of the emission spectrum of TPB (430 nm) matches the region of highest quantum efficiency (QE) of the SiPMs. With a 0.1 $mg.cm^{-2}$ thickness the transmittance of the shifted light is >96% [43].

The K-shell X-ray interactions were used to study the gas properties and drift region [48]. The measured mean electron drift-time allows the correction of the charge loss due to attachment. Results from NEXT-DEMO demonstrated a ^{22}Na 511 keV photopeak energy resolution of 1.62% and a predicted $Q_{\beta\beta}$ resolution of 0.63% [48].

The DEMO tracking allowed the reconstructed single electron from ^{22}Na and ^{137}Cs and double electron from the double escape peak of ^{208}Tl [10]. Recent work with data from the NEXT-DEMO prototype, using ^{22}Na 1275 keV gammas to recreate background and ^{228}Th electron-positron pair representing the signal from $0\nu\beta\beta$ allowed to demonstrate that topology provides extra handles to reject background events [44]. A 24.3±1.4% background rejection factor was obtained while maintaining an efficiency of 66.7±1% for signal events.

The NEXT-DEMO enabled the demonstration of NEXT-100 detector, namely the tracking capability with SiPMs and track reconstruction, to test long drift lengths and high voltages (50 kV in the cathode and 25 kV in the anode) [13].

2.3.2 NEXT-100 and NEXT-White (NEW) detectors

The NEXT-100 is a TPC with 100 kg of gaseous xenon (^{136}Xe) enriched to 91% where the xenon is simultaneously $\beta\beta$ source and detector, providing a fully active volume and homogeneity with no dead regions. The detector is a TPC of 1.4 m diameter and 1.3 m drift length, with both calorimetry and tracking capabilities. The detector is placed on an anti-seismic platform and shielded by 20 cm thick lead castle, set into two movable half's, mounted in two rails as illustrated in Figure 2.5. The NEXT-100 stainless-steel (316Ti, with low level of natural radioactivity) pressure vessel has a cylindrical shape of 160 cm length, 136 cm inner diameter and 1 cm wall thickness. The inner shield is made of 12 cm ultra-pure copper bars and further provides attenuation of γ radiation from the stainless-steel vessel, where a 32 mBq residual activity is estimated.

The energy plane is located behind the cathode of the TPC (Figure 2.6), comprising 60 R11410-10 PMTs (Hamamatsu). The PMTs provide ∼30% fill factor of the energy plane. As detailed in [12], there's a compromise regarding the number of photodetectors with cost, complexity and radioactivity. The PMTs, rated to 6 bar, are inserted into pressure-resistant vacuum-tight copper enclosures coupled to sapphire windows to be located behind the TPC cathode. The PMT cans are maintained at vacuum well below Paschen minimum, avoiding sparks and glow discharge across PMT pins [13]. The low background contribution PMTs have a synthetic silica window and a photocathode made of low temperature bialkali with quantum efficiency above 30% for the emission wavelengths of xenon and TPB [49]. The PMTs in the energy panel measure both primary scintillation light which defines the *start of event* (t_0) and secondary EL light. The radioactivity budget from the energy plane is 35 mBq mainly due to PMTs.

The NEXT-100 tracking plane is located behind a fused-silica window close to the EL

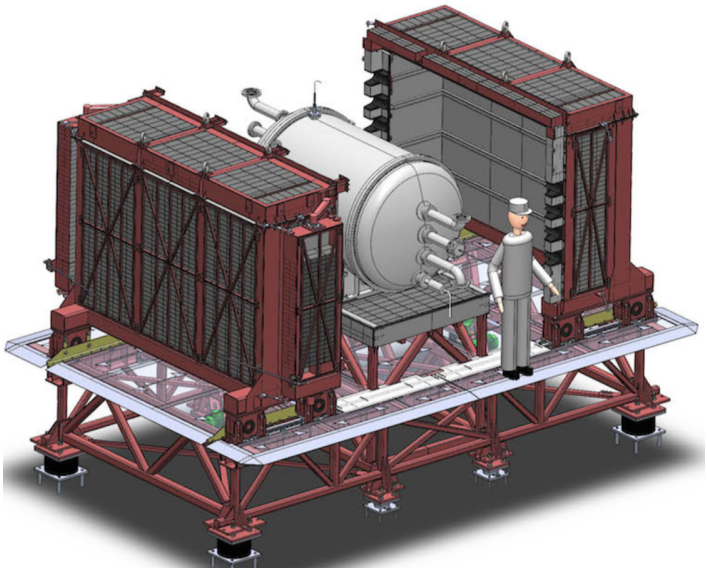

Figure 2.5: NEXT-100 stainless-steel vessel

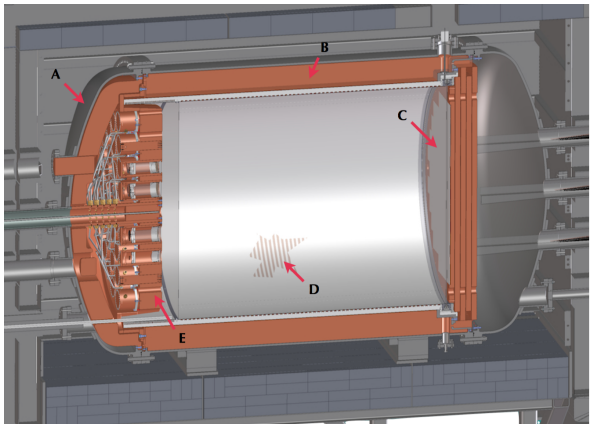

Figure 2.6: Cross-section drawing of the NEXT-100 detector. A) stainless-steel vessel, B) copper shield, C) tracking plane, D) time-projection-chamber including the field cage, cathode, EL grids and HV penetrators E) energy plane. From [10].

gap [12] and will comprise ∼7000 MicroFC-10035-SMT-GP SiPMs from SensL. The SiPMs are distributed into Kapton boards with 64 SiPM each (Figure 2.7), in a 1 cm pitch. The Kapton board cabling is shaped in order to pass through the zig-zag copper shield slit made to avoid a straight path for external gammas.

The NEXT-100 commissioning at LSC is planned for 2017.

The NEW detector is a first approach of the NEXT-100, being limited to 10 kg of enriched ^{136}Xe and only 20% of the energy and tracking plane sensors of the NEXT-100 version (Figure 2.8). NEW is a 1:2 scale detector from NEXT-100, providing technology demonstrator by using the same materials and photosensors. NEW will allow to optimize calibration techniques for NEXT-100 and perform new studies on 2-electron tracking, background rate model and radon contribution and measure the half-life of the $\beta\beta$-decay mode of ^{136}Xe. In addition, the NEW detector is intended for validation of the NEXT-100 background model.

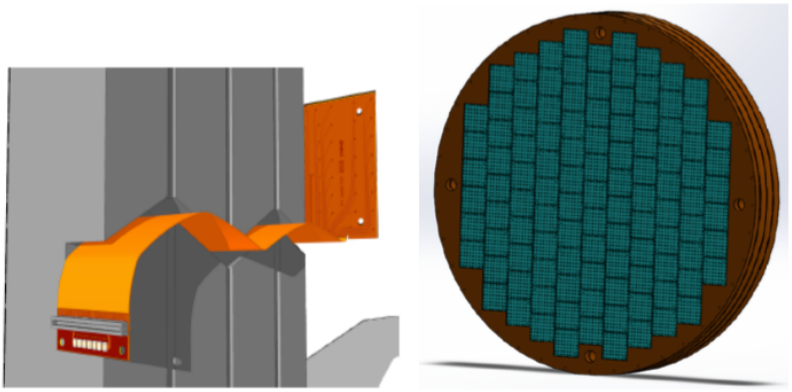

Figure 2.7: Schematic of the Kapton board for the SiPMs (left) and NEXT-100 tracking plane comprising 111 Kapton SiPM boards (right). From [10].

Currently, NEW is under commissioning at the LSC, Canfranc (Spain), Figure 2.9. For NEXT-NEW and NEXT-100, the Cuflon boards were replaced by Kapton boards, allowing oven soldering instead of hand-soldering like in the Cuflon boards. To increase light reflection, the SiPM boards were covered with Teflon masks for light reflection, as shown in Figure 2.10.

The main features of the NEXT detectors are listed in Table 2.1.

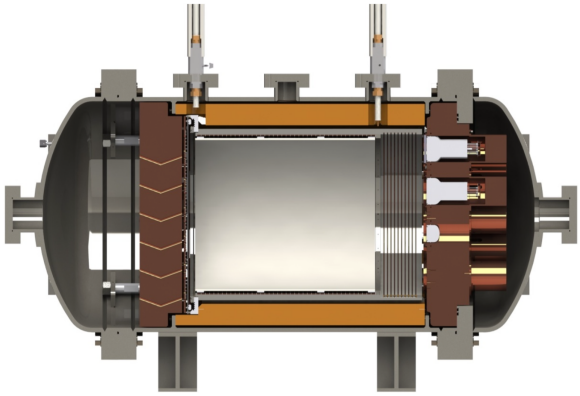

Figure 2.8: Cross-section drawing of the NEXT-White (NEW) detector.

Figure 2.9: NEXT NEW TPC installed at LSC (Canfranc, Spain) and detail of the vessel interior showing the PMTs copper enclosures.

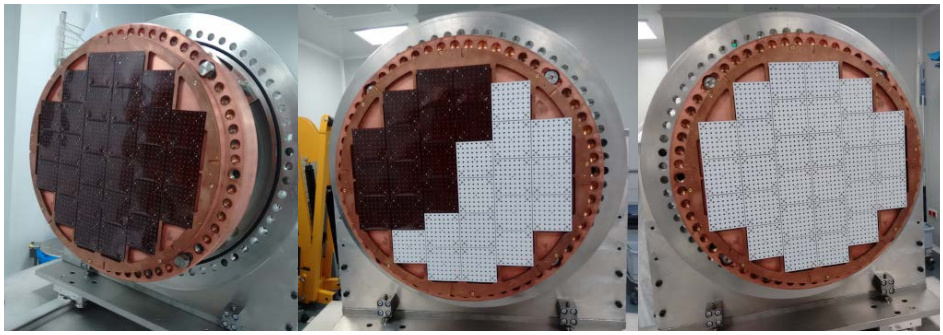

Figure 2.10: NEXT NEW teflon covered DBs.

Table 2.1: Main features and characteristics of the NEXT detectors. Adapted from [50].

	NEXT-DEMO	NEW	NEXT-100
Isotope mass	1 kg, pure Xe	10 kg of 90 % enriched ^{136}Xe	100 kg of 90 % enriched ^{136}Xe
Pressure	10 bar	15 bar	15 bar
Drift length	30 cm	50 cm	1.4 m
Energy plane	19 PMTs	12 PMTs	60 PMTs
Tracking plane	256 SiPMs	1800 SiPMs	7000 SiPMs
Pressure	10 bar	15 bar	15 bar
Radiopure	no	yes	yes
Running period	$2011 - 2014$	$2016 - 2017$	$2017 - 2020$
Localization	IFIC	LSC	LSC

2.4 Silicon Photomultipliers

The developments of solid-state photodetectors, namely with the silicon photomultipliers, allowed a proliferation of this technology through numerous applications. SiPMs became one of the most attractive photodetectors on the market. They are robust and versatile photosensors with an attractive price, turning into one of most promising alternatives for low light level detection, especially for applications where a large number of devices is required.

2.4.1 SiPM principle of operation

A typical SiPM consists of hundreds or thousands of μ-pixels, where each pixel behaves like a Geiger-mode avalanche photodetector (Figure 2.11). The designation silicon photomultiplier results from the resemblance with a PMT operation mode as single photon detector with a very high gain. A single μ-pixel has only two states, *on* or *off*, implying that only one photon can be detected per pixel at the same time. The produced charges from individual pixels sum up in the common anode and the sum charge is proportional to the number of fired pixels, thus allowing to know how many cells have been fired. An incident photon will trigger a Geiger avalanche starting by a discharge of the capacitor until it arrives at breakdown voltage. On normal mode of operation, with a reverse bias below the breakdown voltage the gain obtained is on the order of dozens or several hundreds. On the other side, when a reverse bias above the breakdown voltage is applied, the avalanche photo diode (APD) operating in Geiger mode allows gains of the order of 10^5 to 10^6. In linear mode APDs, the avalanches are mostly started by electrons (almost 100%), developing unidirectionally, from the p to the n layer, and stopping when the charge carriers reach the low field area of the n region.

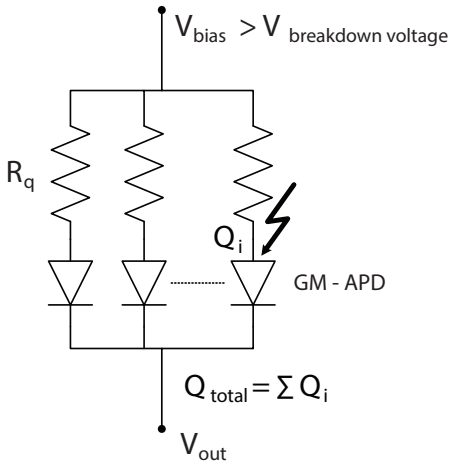

Figure 2.11: SiPM equivalent circuit with i number of Geiger-mode APDs.

2.4.2 SiPM properties

Dynamic range

The dynamic range of the SiPM is related to the number of pixels and the device photon detection efficiency (PDE) and translates the number of fired pixels as a function of the number of incident photons. This means that at high flux rates, SiPM reveal a non-linear behavior. This can be minimized by increasing the number of pixels per active area although at PDE cost due the lower fill factor.

Gain

The gain refers to the ratio of the number of multiplied electrons to one electron ejected by one incident photon on the APD, and can be represented as:

$$G = \frac{C \times (V_{op} - V_{br})}{e \times N_{fired}} \tag{2.1}$$

where C is the device capacitance, V_{op} is the operation voltage, V_{br} is the SiPM breakdown voltage, N_{fired} is the number of pixels fired and e is the electron charge. The SiPM provides a gain for single photoelectrons $\sim 10^6$ with an amplitude of a single cell proportional to the capacitance of the cell and to the overvoltage (the difference between the operation voltage and the breakdown voltage).

Quantum efficiency and photon detection efficiency

The output of the device is the total sum of the outputs from all the pixels and is proportional to the number of incident photons, given that this number is lower than the total number of pixels of the device. The total output charge of the SiPM is:

$$Q_{out} = C \times (V_{op} - V_{br}) \times N_{fired} \tag{2.2}$$

The SiPM charge output should be an integer multiple of the single pixel output, depending on the number of detected photons, but due to several reasons such as small differences between pixels, noise, photon interactions in recharging pixels or in boundary regions between pixels, there are slight variations in the output signals of different pixels.

The quantum efficiency (QE) of the photodetector is the response of the photodetector for a given wavelength and is the fraction of incident photons that contribute to the photocurrent. In practical terms, QE corresponds to the probability of a single photon generate an electron-hole pain in the active region of the device. QE is related to the device photo sensitivity (S) (in A/W units) and depends on the wavelength (λ) (in nm units) of incident photons [51].

The PDE is related to the number of incident photons that are converted into measurable electric charge. PDE is, by definition, the product between the quantum efficiency, the fill factor and the probability of avalanche:

$$PDE = QE \times fill\,factor \times P_{avalanche} \tag{2.3}$$

It depends on the pixel active area, quantum efficiency, geometric factor and avalanche probability (probability of primary electron to trigger the pixel breakdown which depends on the breakdown voltage, in that way, the PDE increases as the bias voltage is increased). In addition, at high light levels, dead time and recovery time also limit PDE. The PDE can be measured by determination of the device response (measured photocurrent) in relation to the incident optical power at a single wavelength. Experimental determination of the PDE can be conducted by the direct current (DC) method by measuring the number of incident photons (N_i) over the number of recorded photons (N_r) using a calibrated photodetector, such as a PMT. Once:

$$N_r = N_{pixels} \times \left(1 - exp^{\left(-\frac{PDE \times N_i}{N_{pixels}}\right)}\right) \tag{2.4}$$

where N_{pixels} is the number of SiPM pixels. For low light levels the SiPM response is linear once $N_i \ll N_{pixels}$. In this regime, the output current of the SiPM (I_{SiPM}) is proportional to N_r and depends on the device gain, such as:

$$N_r = \frac{I_{SiPM}}{gain \times q_e} \tag{2.5}$$

where q_e is the elementary electron charge. The number of incident photons is determined using a calibrated photosensor such an photomultiplier tube (PMT). N_i is obtained from the photocurrent of the PMT collected at its first dynode (I_{PMT}), originated by incident photon on the PMT active area (A_{active}):

$$N_i = \frac{I_{PMT}}{QE_{PMT} \times CE \times q_e} \times \frac{SiPM_{A_{active}}}{PMT_{A_{active}}} \tag{2.6}$$

where QE_{PMT} is the PMT quantum efficiency and CE its collection efficiency. This method doesn't allow to reject the noise contributions (such as cross-talk and after pulsing) leading

to a over-estimation of the PDE. A second method uses pulse counting and is best for low light flux. In this method the number of photons recorded by the SiPM corresponds to the pulse count difference between light pulses and dark pulses.

Noise

The main drawback of the SiPM, particularly for low light level applications, is related to its noise, which comes from three distinct sources:

i) dark pulses

The primary source of noise consists of dark pulses triggered by non-photo-generated charge carriers, mostly thermally generated but also by field-assisted generation (tunneling) of free carriers. The former ones can be reduced only by reducing the electric field.

The temperature dependence is one of the main concerns when operating SiPMs, once the gain is temperature dependent. This is due to the lattice vibrations in the crystal, which become stronger as the temperature rises increasing the probability of a carrier striking the crystal before the accelerated carrier energy has become large enough, making it more difficult for ionization to occur.

ii) cross-talk

The optical cross-talk is the excitation of neighbor pixels due to photon emission during an avalanche discharge in a given pixel. This is observed when photons are produced during the pixel breakdown, some in the infrared region. These photons can travel reasonable distances and penetrate another pixel firing it. In this situation, the SiPM output shows a value higher than the number of photons that were actually input and detected by the SiPM. Besides photons, breakdowns can be triggered by any generation of free carriers. This implies dark currents at a rate up to few MHz per mm^2 (for a threshold of 0.5 p.e.). The cross-talk can be reduced by an optical isolation setting trenches between the μ-cells but this reduces the overall PDE.

iii) afterpulses

Afterpulses are spurious pulses following the true signal, which occur when the generated carriers are trapped by crystal defects and then released at a certain time delay. This results as a second avalanche for the same cell and cause detection errors. Each SiPM pixel requires a short period to recover after breakdown (typically a few ns), so the afterpulse amplitude depends on the time. In addition, the lower the temperature the higher the probability that carriers may be trapped by crystal defects, so afterpulses will increase.

2.4.3 SiPM electrical model

The Geiger operation mode is a three step process: the discharge from a pixel occurs when the pixel is hit by a photon producing an avalanche generating a current proportional to the

cell capacity (C_d) and the SiPM overvoltage (Figure 2.12 (a)). The avalanche is terminated by the quenching resistor in series with the pixel. When the junction breaks down a large current flows through the resistor resulting in a voltage drop across the resistor. If the voltage drop is sufficient, the reverse voltage drops to the breakdown voltage after which there's a recharge to the operating voltage allowing a new cycle. The discharge-and-reset cycle is known as the Geiger mode of operation [51].

A SiPM electrical model has been initially proposed by Pavlov and Meier *et al.* [52], modeling the SiPM micro-cell as a current generator, where C_d is the pixel capacity in series with a quenching resistor, R_q. This model assumes a current pulse with constant amplitude and duration [53]. An updated model was proposed by Corsi *et al.* [54], including the parasitic grid capacitance.

Other SiPM electrical models consider that the micro-cell is modeled by a voltage generator (setting the breakdown voltage), resistor and switch or a self-quenching micro-cell, as proposed by Seifert *et al.* [55] (Figure 2.12 (b)). The closing of the switch defines the start of a breakdown event generating a current through the resistor. The quenching is set by a threshold on the current, such once the current is below the threshold the switch opens. To overcome the fact that trigger generation as a constant switch timing, Marano *et al.* [56] proposed and update to this model also providing equal switching time for all bias voltages (Figure 2.12 (c)). In the proposed model, a negative feedback loop, including a discriminator monitors the diode current and acts upon the switch opening time when this current falls below the current threshold [56]. A new model was proposed by Villa *et al.* [53], (Figure 2.12 (d)), allowing to simulate the SiPM as two macrocells or as an array of individually triggered microcells.

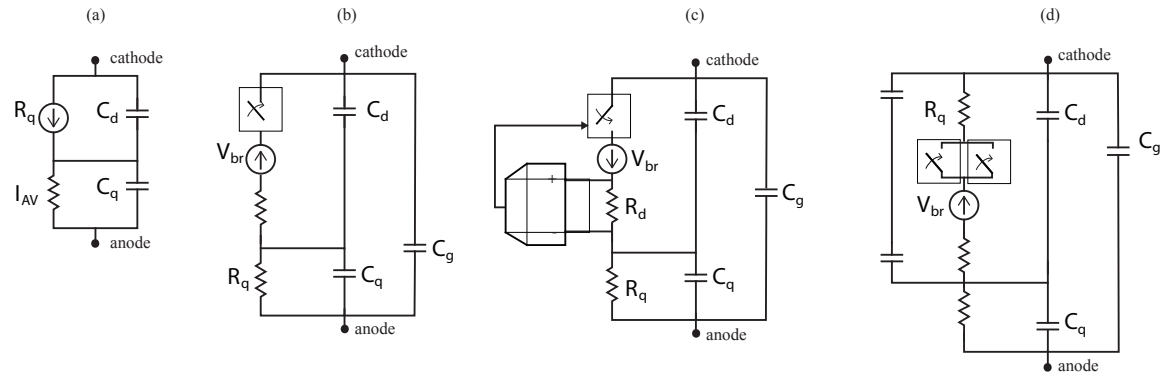

Figure 2.12: SiPM electrical models as proposed by (a) Pavlov and Meier *et al.* (b) Corsi *et al.* [54] (c) Marano *et al.* [56] and (d) Villa *et al.* [53].

2.5 Final remarks

The NEXT detectors are based on a xenon gas time projection chamber offering scalability to large masses of $\beta\beta$ isotope and a low background rate. The first two prototypes, the NEXT DBDM and the NEXT DEMO [44], allowed to perform energy resolution studies and demonstrate the principles of the NEXT-100 detector, namely the tracking capability with SiPMs and track reconstruction. The NEW detector is under commissioning at the LSC, Canfranc (Spain). It is a 1:2 scale detector from NEXT-100, providing technology demonstrator by using the same materials and photosensors.

The NEXT-100 should start taking data in 2017.

The next generation of $0\nu\beta\beta$ experiments is seeking to explore the inverted-hierarchy region, thus requiring $\beta\beta$ isotope masses in the tonne-scale, excellent resolution and low backgrounds. Currently, the most viable path for full background rejection is based on barium-tagging. These new $0\nu\beta\beta$ experiments are under development/planning and new technological challenges are presented.

Chapter 3

Studies on the NEXT Tracking System

3.1 Introduction

SiPMs are a good option for NEXT tracking system, allowing high fill factor at low cost. Silicon is a radiopure material, with activities of ^{238}U and ^{232}Th in the order of μBq/kg [46]. Notwithstanding, other materials used in the SiPM construction can be radioactive. To achieve a low background level is one of the most demanding tasks in NEXT. The screening of radioactivity levels of all components is under going at LSC [12, 46, 57, 58]. To reach the lowest background level, all the electronics are placed outside the chamber. The power consumption is also a concern, considering the large number of channels. Several versions of the SiPM readout for NEXT were developed by the Valencia group at IFIC.

The NEXT-100 detector will use 111 Dice Boards comprising 64 SiPMs each. For the NEXT-DEMO, the tracking plane comprised only four DBs made of Cuflon due to lower radioactivity (Figure 3.1, left). For NEXT-NEW and NEXT-100, the Cuflon boards were replaced by Kapton boards (Figure 3.1, right), allowing oven soldering instead of hand-soldering like in the Cuflon boards.

In this chapter are presented the studies related to the experiment tracking plane, namely related to SiPM characterization, readout and possible alternatives for event topology and tracking in large TPCs.

3.2 SiPMs for the NEXT tracking plane

The Hamamatsu SiPMs, MPPC S10362-11-050U, were the selected SiPMs for NEXT-DBDM and NEXT-DEMO [59]. Although, new SiPMs provided by SensL (MicroFC-10035-SMT) are operated at lower bias voltage and present lower radioactivity. For the SensL SiPM, were obtained activities of 3×10^{-5} mBq and 9×10^{-5} mBq for ^{208}Tl and ^{214}Bi, respectively [12]. For this reason, the SensL MicroFC-10035-SMT was the selected SiPM for the tracking

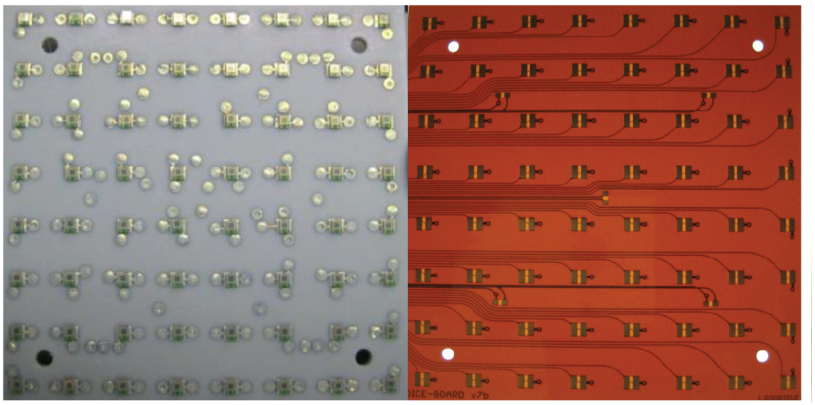

Figure 3.1: NEXT-DEMO Cuflon daughter board with 64 SiPM (left) and the Kapton boards for NEW and NEXT-100 tracking panel (before SiPMs installation) (right).

plane of the NEXT-NEW detector [46, 59]. Other interesting features from the SensL MicroFC-10035-SMT are a fast output and advertised lower dark noise and lower sensitivity to temperature. This new SiPM will be evaluated in the following section and compared with the Hamamatsu MPPC S10362-11-050U.

The SensL MicroFC-10035-SMT and the Hamamatsu MPPC S10362-11-050U are SiPMs with 1 mm^2 active area. The Sensl SiPM has 35 μm$\times$ 35 μm area pixels (504 pixels in total) and the MPPC S10362-11-050U has 50 μm$\times$ 50 μm pixel size (400 pixels in total).

More recently, new VUV-sensitive SiPM prototypes were provided by Hamamatsu. This new SiPM has a 3 mm$\times$ 3 mm active area and 50 μm$\times$ 50 μm pixel size. PDE studies at VUV range where performed and results are presented here and have been published elsewhere [60].

3.3 Evaluation of SiPM readout methods

Specific SiPM readout methods can be employed envisaging better *signal to noise ratio* (SNR), dynamic range and data throughput [61], depending on the applications. The most common readout methods are continuous current, gated integrator and photon counting or pulse mode. In current mode, the SiPM is illuminated with almost steady light level. In this regimes, the SiPM readout circuit is performing a charge amplification and acting like a picoammeter or electrometer by continually measuring the photocurrent and sampling the result over time. When the light level is extremely low, as in some scintillation detectors used in nuclear and particle physics, the SiPM sees discrete single photon events consisting of short duration pulses at random intervals rather than large bursts of photons or the continuous flow of multiple overlapping photons, as mentioned previously. Under these conditions, a threshold is set allowing discriminating the incident light and counting the number of events over a time period.

When several SiPMs are placed in an array, it is possible at some extension to apply

multiplexed readouts scheme at the cost of signal integrity. Notwithstanding, this might represent a significant saving regarding the ∼7000 SiPMs channels used.

The readout schemes developed were based in commercial integrated circuits (ICs). In Table 3.1 are listed the majority of all the ICs evaluated. In the following Sections (3.3.1 and 3.3.2) only the best ICs or the ones with which a stable design was achieved are presented.

Table 3.1: List of evaluated ICs.

Manufacturer	Texas Instruments	Analog Devices	Maxim Integrated	Linear Technologies	Hittite
operational amplifier	OPA656	AD8000		LTC6400	
	OPA657	AD8099			
	OPA847				
transimpedance amplifier					HMC799
current mirror		ADL5317	DS3920		
			MAX4007		
			MAX4008		
log converter		AD8304			
		ADL5303			
		ADL5304			
DC-DC converter			MAX1932		

3.3.1 SiPM pulse mode readout

For SiPM characterization, a dedicated SiPM readout was developed, comprising two ultra-low noise 3.8 GHz AD8099 high speed op-amps from Analog Devices. Further details about the SiPM readout electronics are present in Appendix A. In Figure 3.2 is depicted a typical SiPM pulse amplified (as described in Appendix A, Figure A.2), with pulse rise time (10 - 90 %) of ∼5 ns. It is also observable the afterpulsing. When occurring after the recovery time, these events cannot be distinguished from photon-induced events, thus degrading the device photon-counting resolution.

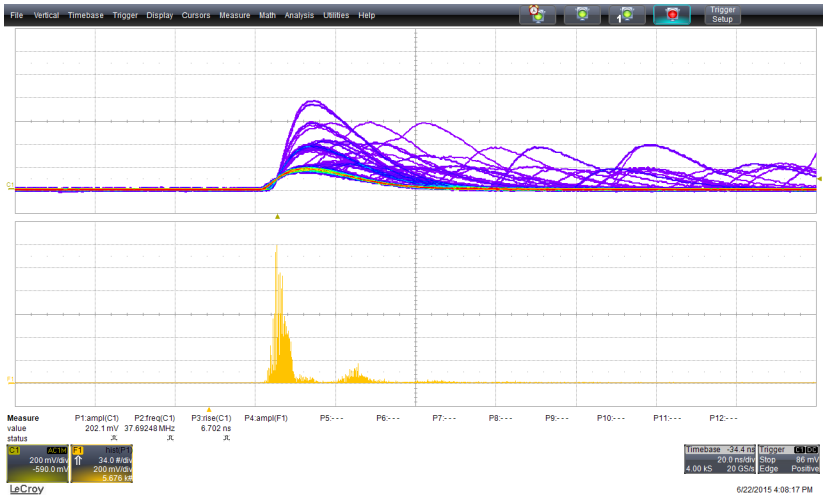

Figure 3.2: Oscilloscope screen captured with triggered SiPM pulse (top) and respective histogram (bottom) from a Hamamatsu MPPC amplified by circuit from Appendix A, Figure A.2.

The SensL MicroFC-10035-SMT SiPM has an additional fast output. In Figure 3.3 is depicted an oscilloscope screen captured (Lecroy Waverunner 625 Zi) with triggered pulse from a SensL SiPM coupled to a 2×2×30 mm^3 LYSO scintillator irradiated with a ^{22}Na radiation source. The two pulses correspond to the fast output (blue pulse), used for triggering the ADC and the anode output (green pulse). Both pulses are amplified by circuit from Figure A.2 (Appendix A).

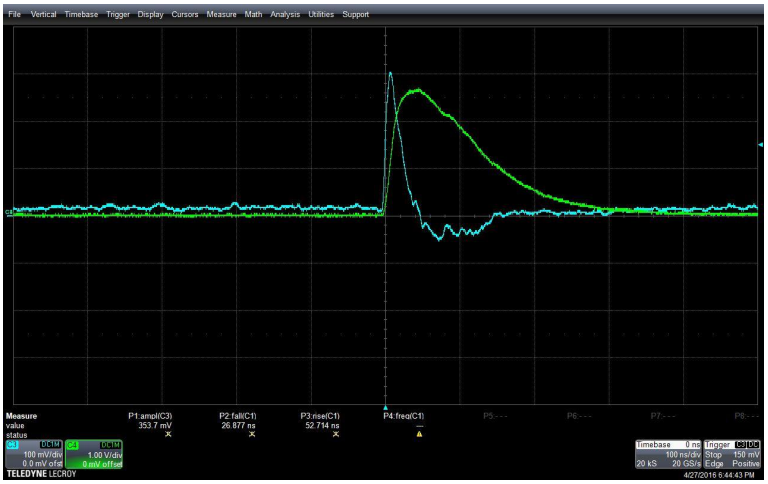

Figure 3.3: Oscilloscope screen captured with triggered pulse from a SensL SiPM coupled to a 2×2×30 mm^3 LYSO scintillator irradiated with a ^{22}Na radiation source. The two pulses correspond to the fast output (blue pulse), used for triggering the ADC and the anode output (green pulse). Both pulses are amplified as circuit from Figure A.2 (Appendix A).

3.3.2 SiPM current mode readout

Evaluation of current mirrors

SiPMs are available with different pixel number, ranging from hundreds to thousands of pixels, allowing higher dynamic range at the cost of the photon detection efficiency. In some conditions, when the light flux is high, the easiest way to read a SiPM is in current mode, whereas one can subtract the dark current. On the other hand, in low light flux the dark current easily masks the signal from incident photons. In these situations, operation in pulse/count mode is recommended. Typically, dark noise pulses go up to 3 p.e. (depending on parameters such as the over-voltage and temperature) making it difficult the identification of spurious signals from incident photons. When operating on a wider range of light flux, the ideal is to use dual mode, reading the SiPM in current and pulse modes simultaneously. This is possible using a Current Mirror. Typically these IC's output is a current proportional to the input current but with lower intensity.

Four current mirrors were evaluated, MAX4007, MAX4008, DS3920 (Maxim Integrated) and ADL5317 (Analog Devices). The devices specifications are summarized in Table 3.2. The MAX4007 and DS3920 Current Mirrors (CM) from Maxim Integrated have 10:1 and

5:1 output mirrors, respectively. MAX4008 is equivalent to MAX4007 but the output is a voltage, with a mirror ratio of 1 mV/mA. The ADL5317 current monitor allows avalanche photodiode bias control.

Table 3.2: Current mirrors evaluated.

	MAX4007	MAX4008	DS3920	ADL5317
Mirror ratio	10:1	1mV/mA	5:1	5:1
Input voltage (V)	2.7 to 76	2.7 to 76	2.97 to 76	6 to 75
Max input current (mA)	20	20	4.4	21
Package	6 SOT23	6 SOT23	6 SOT23	16 LFCSP-VQ

The calibration of the four current mirrors was performed by placing a resistor in the pin corresponding to the voltage output pin, whereas the SiPM is connected. The resistor is connect to the ground. Resistors of 1 MΩ, 10 MΩ, 100 MΩ and 1 GΩ where used. The resistors were shielded in an aluminum enclosure with SMA connectors. The ADL5317 was set in supply tracking mode and Keithley 6487 picoammeter was used as voltage source and for measurement of current output from the current mirror. The measurements performed with the picoammeter correspond to the average of 100 acquisitions in normal rate mode (fast and slow rate modes are also options). The voltage at V_{APD} (output voltage pin) is clamped to 2.0 V below V_{PHV} (input voltage pin). To read the mirrored current with an ADC or voltmeter, a grounded resistor can be placed at the current mirror output to convert the mirrored current into a voltage. When an ADC is used to digitize the signal, the resistor to ground can be selected in such a way to maximize the ADC full-scale voltage to the maximum mirrored current. The results obtained by measuring the devices in both current and voltage are depicted in Figure 3.4.

The best results in terms of linearity where achieved by reading the current mirror response in current mode. However, one should note that the picoammeter provides higher resolution and the acquired measurements correspond to a 100 measurements average. The ADL5317 and DS3920 are the two current mirrors evaluated showing best performance at currents in the tens of nA.

Evaluation of AD8304, ADL5303 and ADL5304 logarithmic converters

The signal of the current mirror can be directly read by an ADC using a resistor connected to the ground. Although, when there's a need for large dynamic range a *log converter* can be used. The output of the log amplifier V_{out} is:

$$V_{out} = Kln\frac{V_{in}}{V_{ref}} \tag{3.1}$$

where K is the scale factor, V_{in} is the input voltage and V_{ref} the normalization constant.

Three log amps were evaluated, all from Analog Devices, being the main characteristics listed in Table 3.3. AD8304 is a 160 dB logarithmic converter optimized for measurement

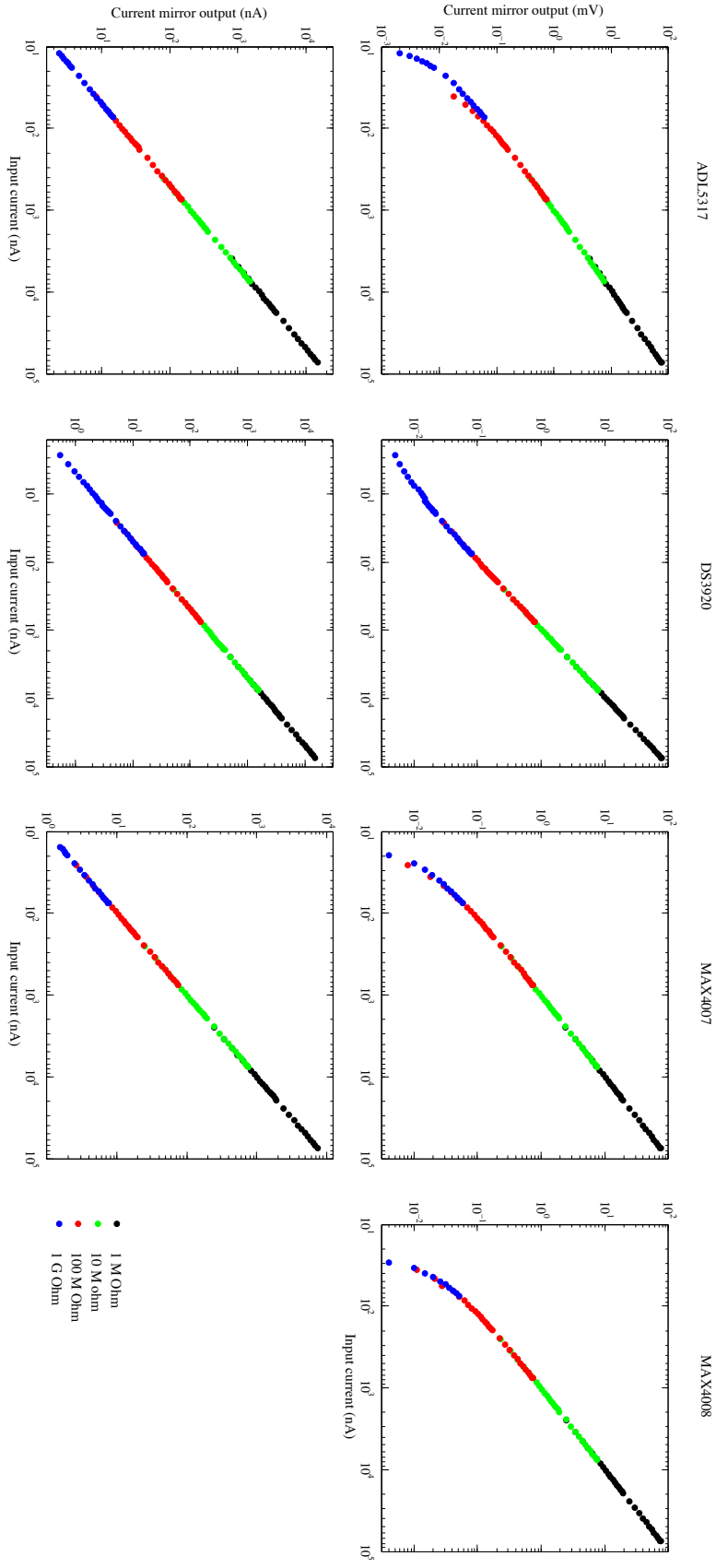

Figure 3.4: Current mirror calibration with 1MΩ-1GΩ resistors.

of low frequency signal power in fiber optic systems. ADL5303 is a 160 dB logarithmic converter, corresponding to 100 pA - 10 mA. ADL5303 is a low cost version of the ADL5304 logarithmic converter with 200 dB range, from 1 pA to 10 mA. ADL5304 has a 25 kHz bandwidth at 1 nA, while the AD8304 and ADL5303 bandwidth at 1 nA is 2 kHz.

Table 3.3: Logarithmic converters evaluated.

	AD8304	ADL5303	ADL5304
Input range	100 pA to 10 mA	100 pA to 10 mA	1 pA to 10 mA
Input range (dB)	160	160	200
Output bandwidth at 1nA	2 kHz	2 kHz	25 kHz (350 kHz at 10 nA)
Max output bandwidth	10 MHz	10 MHz	4 MHz
Package	14 TSSOP	16 LFCSP	32 LFCSP

The three logarithmic converters were calibrated using an 1 GΩ resistor. The resistor was shielded in an aluminum enclosure with SMA connectors. A Keithley 6487 picoammeter was used as voltage source and connected to one pin of the resistor, while the other pin is connected do the logarithmic converters input pin. The output from the logarithmic converter was measured with a Fluke 287 multimeter. Results are plotted in Figure 3.5. From the three devices evaluated, the ADL5304 is the logarithmic amplifier with higher gain of 200 dB, as clearly visible from Figure 3.5. This device is intended for operation in the 1 pA to 10 mA input current range. However, the observed threshold for the device response was 1.6 nA. The responses of the AD8304 and the ADL5303 converters are similar once the devices have the same input range. The measured minimum input for AD8304 was 500 pA while for ADL5303 was 800 pA. All the three logarithmic converters have a default logarithmic slope of 10 mV/dB and basic logarithmic intercept at 100 pA, notwithstanding, both slope and intercept can be adjusted. From the three logarithmic converters evaluated, ADL5304 present higher bandwidth at low currents, making this one the most suitable option for measurements at low light levels.

This study allowed to conclude that the AD8404 is the most suitable device for a wider operation range. For this reason it was the selected logarithmic converter for integration with the ADL5317 current mirror.

ADL5317 current mirror and AD8304 logarithmic converter

A printed circuit board was developed to test the ADL5317 current mirror with a AD8304 logarithmic converter (as described in Appendix A, Figure A.2). The system was evaluated in the $1-100$ V range with a 1 GΩ resistor, allowing currents up to 98 nA (due to the 2 V voltage drop featured in ADL5317). The V_{APD} pin of ADL5317 is connected to a 1 GΩ resistor that is connect to ground. The ADL5317 photodiode monitor current output pin is connected to the AD8304 logarithmic converter. The output of the AD8304 was measured with a Fluke 187 multimeter. Calibration result is plotted in Figure 3.6. The ADL5317 current mirror has an operating threshold corresponding to an input voltage $\sim$ 6 V, corresponding to 4 V at the 1 GΩ resistor. This corresponds to an mirrored current of $\sim$ 800 pA. As one observed from

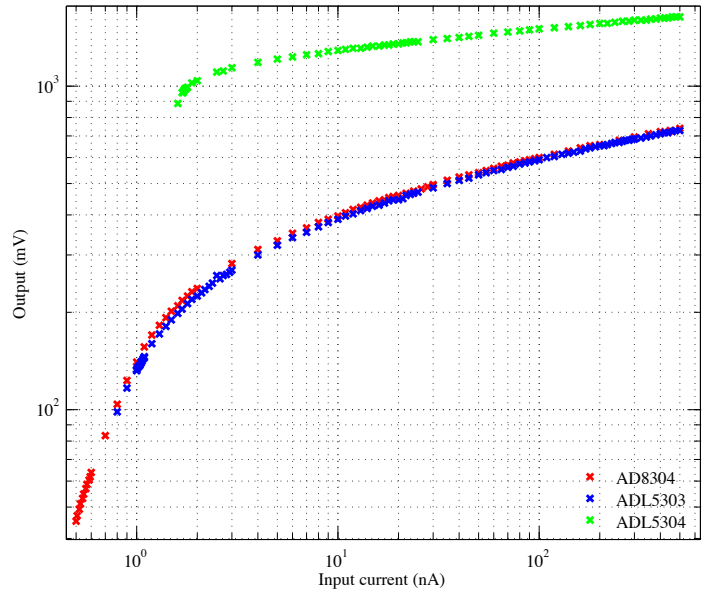

Figure 3.5: Test of the Analog Devices AD8304, ADL5303 and ADL5304 logarithmic converters in the $1 - 500$ nA range, with 1 GΩ resistor.

the previous study regarding the logarithmic converters, the AD8304 operates at currents above 50 nA. As observable in Figure 3.6, small deviations are related to the change on the decade of the logarithmic converter. The observed behavior is belied to be imposed by the AD8304 device. Further studies are required in order to optimize the system.

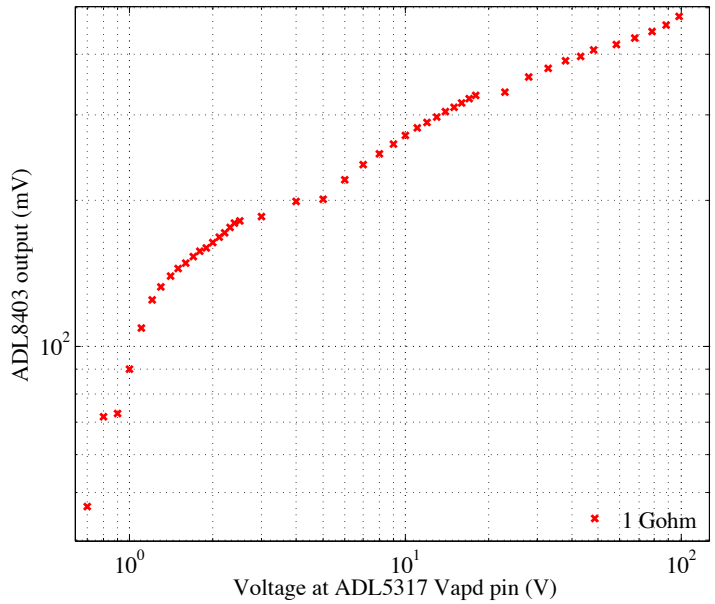

Figure 3.6: Analog Devices AD8304 calibration with 1 GΩ resistor.

3.4 SiPM characterization

The typical parameters required for SiPM characterization are listed in Table 3.4 [62, 63]. Two SiPMs were evaluated, the SensL MicroFC-10035-SMT (recently adopted as the SiPM for the NEXT tracking plane due to their low radioactive footprint) and the Hamamatsu MPPC S10362-11-050, both with an active are of 1 mm^2. For the characterization studies, the SiPMs were biased with a Keithley 6484 picoammeter and voltage source, also used for the SiPM current measurement. The SiPM was placed inside a dark box built for these studies. The box temperature was monitored with a DB18B20 (MAXIM Integrated) digital temperature sensor. The temperature was adjusted with a Peltier cell controlled by an Arduino Mega microcontroller loaded with a motor-shield including a TB6612 dual H-bridge with 1.2 A per channel current capability. The measurements were performed in the 15° to 45 °C temperature range.

3.4.1 I-V curves

The study of the I-V curves is important when SiPMs are operated in continuous light flux or high illumination in periods longer than hundred of nanoseconds. These tests allow to estimate the current range and to identify the breakdown voltage of the SiPM. The dark current was measured over the bias voltage in the $70 - 74.5$ V range for the Hamamatsu SiPM and $22 - 25$ V for the SensL SiPM. The obtained I-V curves for the two SiPMs are depicted in Figure 3.7. From the analysis of the I-V curves, one can determine the breakdown voltage. Besides direct observation of the curves, a more precise method can be performed by calculating the second derivative to identify the inflexion points of the I-V curves. This analysis is presented and discussed in Section 3.4.4 together with the breakdown voltage determined by the SiPM gain study.

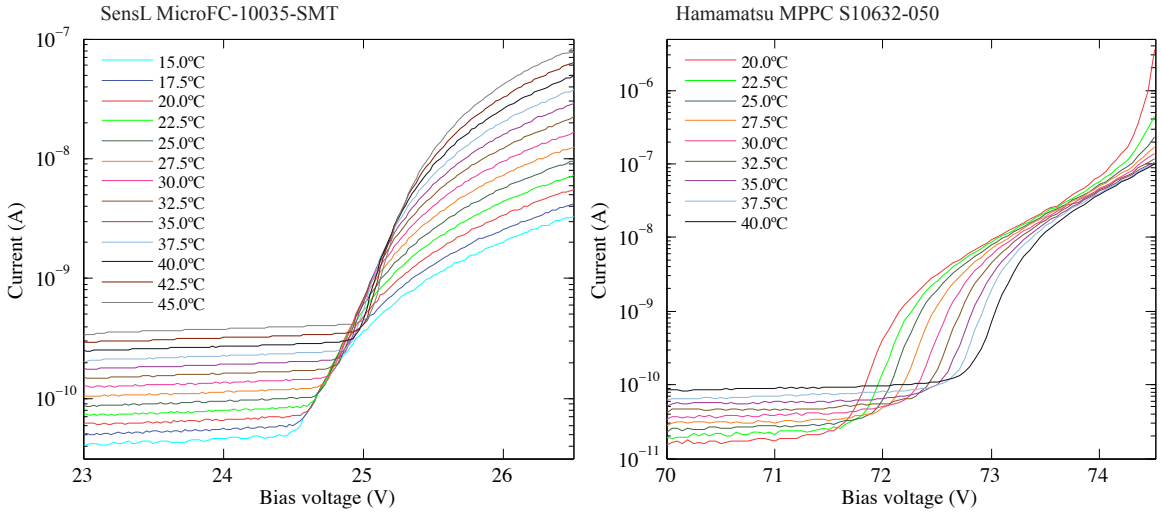

Figure 3.7: Hamamatsu MPPC S10362-11-050U (left) and SensL MicroFC-10035-SMT (right) I-V curves.

Table 3.4: SiPM parameters

SiPM properties	**Study**	**Parameters**	**Measurement**	**Comments**
Breakdown voltage	I-V curve	temperature	dark current	calculate inflexion points (2nd derivative)
		bias voltage		to identify $V_{breakdown}$
Dark noise	DCR	over voltage	counts	
		temperature		
Crosstalk probability	staircase diagram	ADC threshold	DCR	
		bias voltage		
p.e. threshold				
Gain	pulse-high spectrum	temperature	ADC channels	
		over voltage	between adjacent peaks	
PDE (method 1)	Current	light wavelength	current	use calibrated photodetector to
				measure number of incident light flux
PDE (method 2)	Pulse	light wavelength	pulse counts	use calibrated photodetector to
				measure number of incident photons

3.4.2 Dark-count rate and crosstalk probability

The dark-count rate (DCR) has been measured at different reverse voltage values for the temperature range of $20 - 40$ °C. The DCR is measured by performing a threshold scan and registering the mean frequency. The pulse signal from the SiPM is fed into a comparator with threshold adjusted with a digital potentiometer controlled by an Arduino DUE microcontroller. The TTL signal from the comparator output is a digital signal, having only two states, *off* when amplitude of input signal is below the threshold and *on* when the input signal is above the threshold. Considering that the amplified SiPM signal has width between $40 - 100$ ns, a monostable multi-vibrator is used to stretch the comparator output to a fixed width, allowing to measure the signal frequency with an Arduino DUE microcontroller. The curves for the SensL MicroFC-10035-SMT and the Hamamatsu MPPC S10362-11-050U are depicted in Figure 3.8. Due to the observable plateaus corresponding to the 0.5, 1.5, 2.5, etc. photo-electron (p.e.), these curves are typically known as SiPM staircase diagrams or staircase curves.

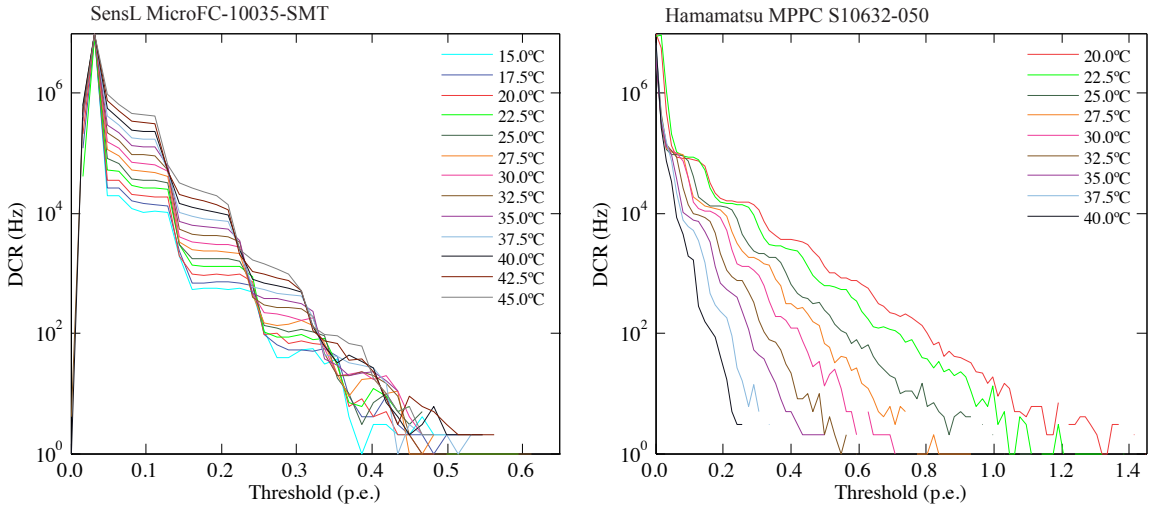

Figure 3.8: Crosstalk study for the SensL MicroFC-10035-SMT (at 2.5 V overvoltage) and the Hamamatsu MPPC S10362-11-050U (at 1.5 V overvoltage).

The same study was repeated at several overvoltage levels for the same temperature ranges. From the resulting staircase diagrams, one can calculate the inflexion point of the derivative, allowing to know the 0.5 p.e. and 1.5 p.e. levels at each temperature. Data are presented in Figure 3.9. One can observe the exponential increase of the DCR with the temperature increase. For an 1.5 p.e. threshold the SensL SiPM presents a DCR one order of magnitude lower than the Hamamatsu SiPM. In addition, for the Hamamatsu SiPM, for a given temperature, it is observable an increase of the DCR as the overvoltage increases. This can be due to a bigger probability of crosstalk and afterpulsing. The crosstalk probability was estimated by computing the ratio between the DCR at 1.5 p.e. and DCR at 0.5 p.e.

threshold (Figure 3.10). The crosstalk probability increases with increasing overvoltage. For the Hamamatsu SiPM, an increase from an average 6% at 1.0 V overvoltage to 25% for 2.0 V overvoltage was observed (Figure 3.10, right).

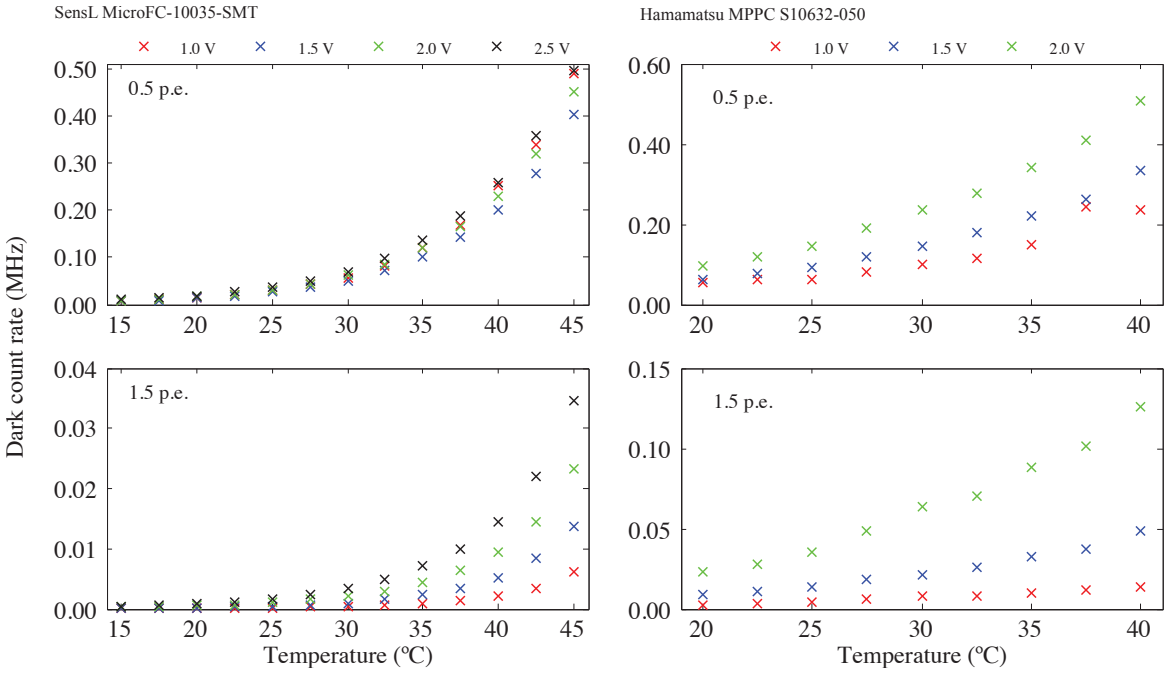

Figure 3.9: Dark Count Rate (DCR) for the SensL MicroFC-10035-SMT and the Hamamatsu MPPC S10362-11-050U at 0.5 p.e. and 1.5 p.e. thresholds for different over-voltage.

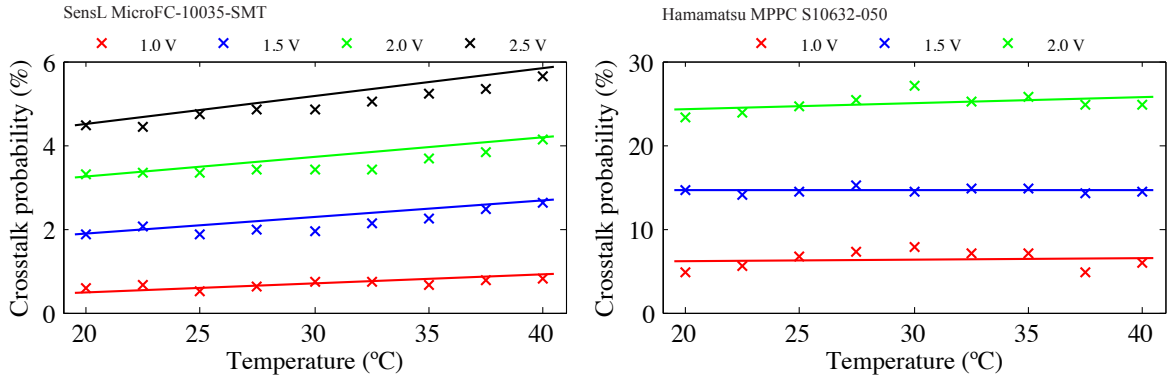

Figure 3.10: Crosstalk probability for the SensL MicroFC-10035-SMT and the Hamamatsu MPPC S10362-11-050U.

3.4.3 Gain

Studies on gain dependence with overvoltage and temperature were performed for both SensL MicroFC-10035-SMT and Hamamatsu MPPC S10362-11-050U SiPMs.

The SiPM gain was measured by illuminating the SiPM with a low photon flux from a blue LED, with emission peak at $\sim$ 474 nm (measured with USB4000-UV-VIS spectrometer,

Ocean Optics). Both LED and SiPM temperature were constantly monitored with a DS18B20 (Maxim Integrated) digital thermometer. DS18B20 is programmable providing $9-12$ bit and $\pm 0.5°$ accuracy from $-55°$ to $+125°$. The SiPM was placed inside a light tight aluminum enclosure (Figure 3.11) with temperature controlled by a Proportional–integral–derivative (PID) controller system with a large Peltier Cell placed below the aluminum enclosure. The signal from the SiPM was amplified by the 2-stage readout described in Section 3.3.1. The acquisition of the pulses was done with a CAEN V1724, 14 bit 100 MS/s digitizer, with an external trigger from the pulse generator used to power the LED. The LED was biased with an Agilent pulse generator, using pulses of 90 ns width and 8.4 ns egde time, at 100 kHz. The pulse amplitude for the LED was selected in order to optimize the best descrimination between the photopeaks in the spectrum. A pulse amplitude of 875 mV amplitude was set for the Hamamasu SiPM and 1.150 V for the SensL SiPM.

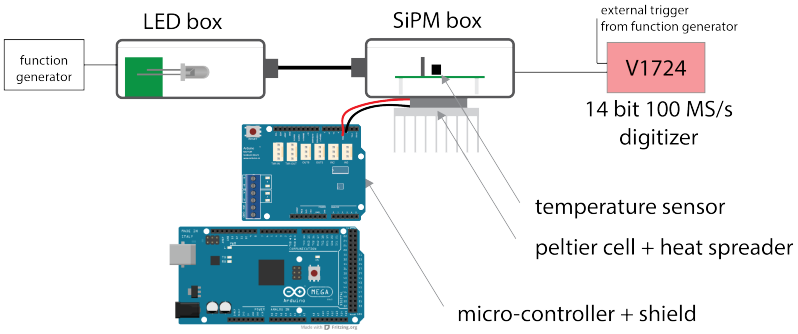

Figure 3.11: Experimental setup for the studies of the SiPM gain with overvoltage at several temperatures.

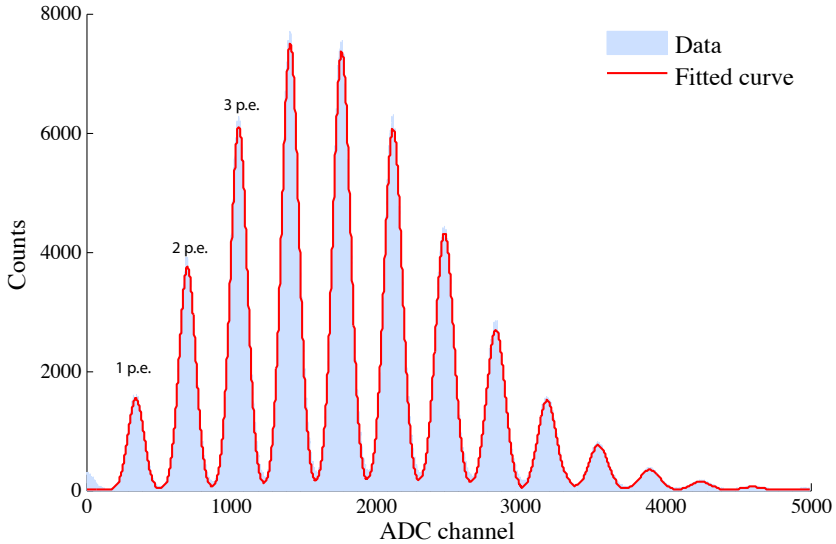

Figure 3.12: SensL MicroFC-10035-SMT pulse-high spectrum when illuminated by a blue LED, showing multiple peaks. The SiPM was at 25.0 °C, biased at 26.0 V.

Measurements were performed with a 2.5 °C step in the 20° to 40 °C range for the Hamamatsu SiPM and in the 15° to 45 °C range for the SensL SiPM. At each temperature, a pulse high histogram was obtained in the $73.0 - 74.5$ V bias voltage range with a 100 mV step, in a total of 144 histograms for the Hamamatsu SiPM and in the $25.5 - 27.0$ V bias voltage range with a 100 mV step, in a total of 208 histograms for the SensL SiPM. The pulse high histograms were analyzed with MATLAB, using *find peaks* function to identify photoelecton before performing gaussian fit. The number of ADC channels between adjacent peaks was used to calculate the gain value for each spectrum. Results are presented in Figure 3.12. This number of ADC channels between adjacent peaks increases with gain and is expected to be the same between adjacent peaks for the same spectrum, corresponding to the charge from a single Geiger discharge. Once known the charge of a single discharge, one can calculate the SiPM gain using Eq. 2.1. The gain from the electronics and the ADC was determined using a 6.8 pF capacitor using a fast pulse in the $0.1 - 1$ V amplitude range from a pulse generator.

In Figure 3.13, one observes a variation on the SiPM pulse-height spectrum over temperature even with gain correction by bias voltage adjustment using the temperature coefficient determined experimentally. Although the SiPM gain variation is small, at higher temperatures the spectrum moves to the left, meaning that the pulse amplitude is lower. The possible explanation is the increase of crosstalk and afterpulses within the gate window, resulting in the broadening of the p.e. peak in the spectrum.

The SiPM gain for each temperature at different overvoltage was calculated and is depicted in Figure 3.14.

3.4.4 SiPM temperature coefficient and gain stabilization

As mentioned in previous chapter (Section 2.4.2), the gain of the SiPM is the ratio between the total charge from a Geiger discharge and the electron charge. The total charge generated by a single discharge corresponds to the pixel capacitance times the over voltage. As verified above (Section 3.4.1), the breakdown voltage has a strong dependence on temperature. The breakdown voltages over temperature were extracted from both I-V curves (Figure 3.7) and Gain study (Figure 3.14), for the Hamamatsu MPPC S10362-11-050U and the SensL MicroFC-10035-SMT. The first method consists of obtaining the second derivative to identify the inflexion points of the I-V curves. The second method from the SiPM gain study is achieved by obtaining the x-axis intercept of the linear fit which returns the SiPM breakdown voltage [64]. The data resulting from the two methods are depicted in Figure 3.15.

The temperature coefficient can be obtained from the slope of the breakdown voltage over the temperature (Figure 3.15). In Table 3.5 are listed the temperature coefficients obtained from the I-V curves and from the gain over temperature studies.

For the SensL SiPM, the reference value is closer to the value obtained for the gain method while for the Hamamatsu SiPM the temperature coefficient obtained from the IV-

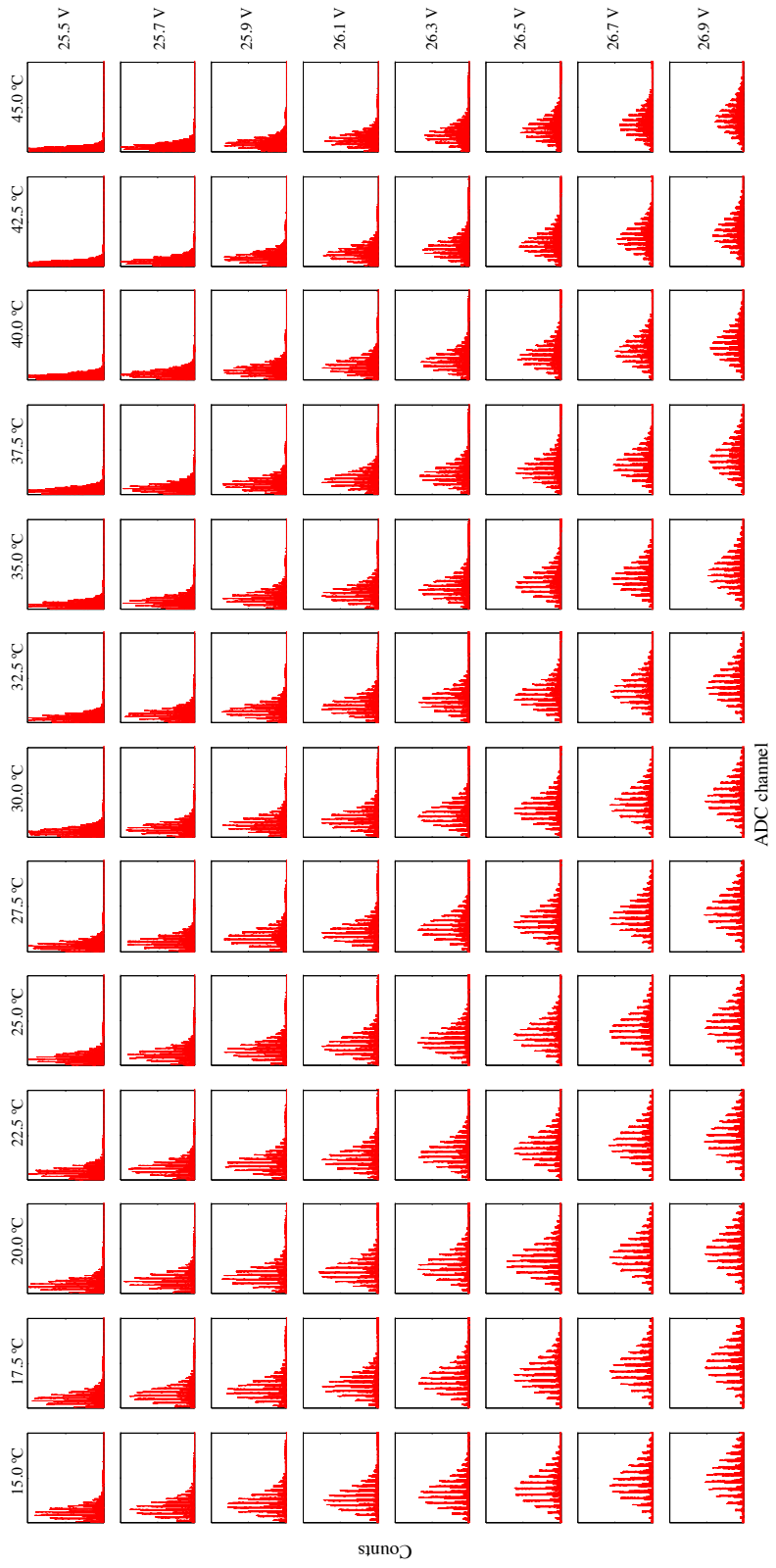

Figure 3.13: Pulse-height spectrum for the SensL MicroFC-10035-SMT for different temperatures and bias voltages.

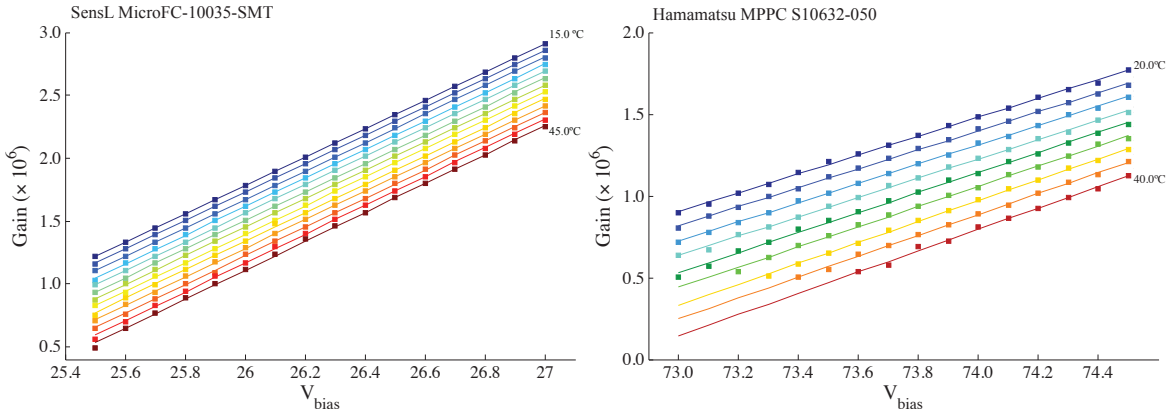

Figure 3.14: SiPM gain variation as a function of the bias voltage for the SensL MicroFC-10035-SMT (left) and the Hamamatsu MPPC S10362-11-050U (right).

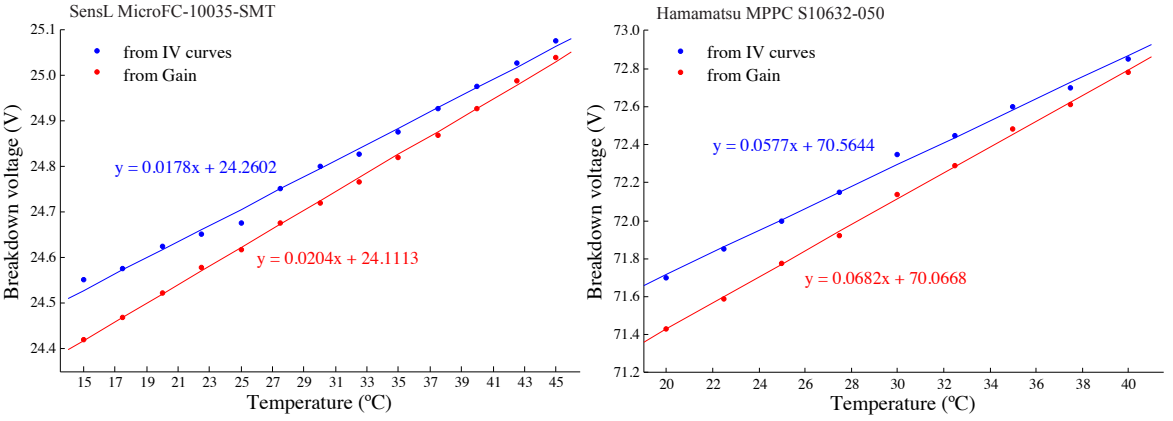

Figure 3.15: Breakdown voltage at several temperature for SensL MicroFC-10035-SMT (left) and the Hamamatsu MPPC S10362-11-050U (right), determined from IV curves (blue) and from Gain curves (red).

curves is in agreement with the reference value. For both SiPMs, a higher temperature coefficient was obtained with the gain method. The main reason can be justified by the contribution of crosstalk and afterpulses, which is not verified in the gain method due to the use of an external trigger to the ADC. For the SensL SiPM, the temperature coefficient obtained in the gain method is in accordance with the data provided from the manufacturer, although for the SiPM the temperature coefficient resulting from the I-V curve method is the closest to the value provided from the manufacturer. More studies should be addressed

Table 3.5: SiPM breakdown voltage and temperature coefficient obtained from the I-V curves and Gain variation over temperature methods.

	breakdown voltage (V) at 25 °C		Temperature coefficient (mV/°C)		
	I-V curves	Gain	datasheet	I-V curves	Gain
SensL MicroFC-10035-SMT	24.71	24.62	21.5	17.8	20.4
Hamamatsu MPPC S10362-11-050U	72.01	71.77	56	57.7	68.2

in order to evaluate the two methods and access which one should be considered, once SiPM temperature coefficients allow to set a constant gain with temperature variations by bias voltage adjustment.

Once known the SiPM temperature coefficient one can set a system to perform bias adjustment to overcome temperature fluctuations. SiPM gain correction by bias voltage adjustment was performed for the SensL MicroFC-10035-SMT and the Hamamatsu MPPC S10362-11-050U silicon photomultipliers according to the temperature coefficients listed in Table 3.5. The experimental apparatus is the same as described in the previous section. For the SensL SiPM, four sets of measurements were taken, one of them using the temperature coefficient obtained by the IV-curves and the other three using the temperature coefficient obtained by the gain measurements. For the Hamamatsu SiPM, two sets were taken for temperature coefficient obtained by I-V curves and one set using the temperature coefficient from the gain measurements. Results are plotted in Figure 3.16. For reference, the uncorrected gain values are included for both SiPMs, corresponding to the overvoltage of 2.5 V at 25 °C.

As one can see from Figure 3.17, the best results for the SensL SiPM show a $\Delta G/G$ below 1% in the $15 - 45$ °C range using the temperature coefficient obtained by the gain method. For the Hamamatsu SiPM, a $\Delta G/G$ higher than 5% was obtained for both cases. For the last one, the gain stabilization was not very well succeeded, revealing some problem with the experimental setup. New studies are required. Using the same correction methods, Marrocchesi *et al* [65] obtained a stability $\Delta G/G$ below $\pm 1\%$ in the range $9 - 31$ °C for the Hamamatsu MPPC.

Li *et al* [66] implemented a voltage-controlled current sink module with temperature compensation using thermistors, achieving a drift in the gain lower than 0.3%/°C in the temperature range $5.1 - 33.3$ °C. Licciulli *et al* [67] implemented a method where a second blinded SiPM is used for pulse-high monitoring, allowing the tracking in gain variation. The detector is enclosed in a negative feedback loop which automatically adjust bias voltage,

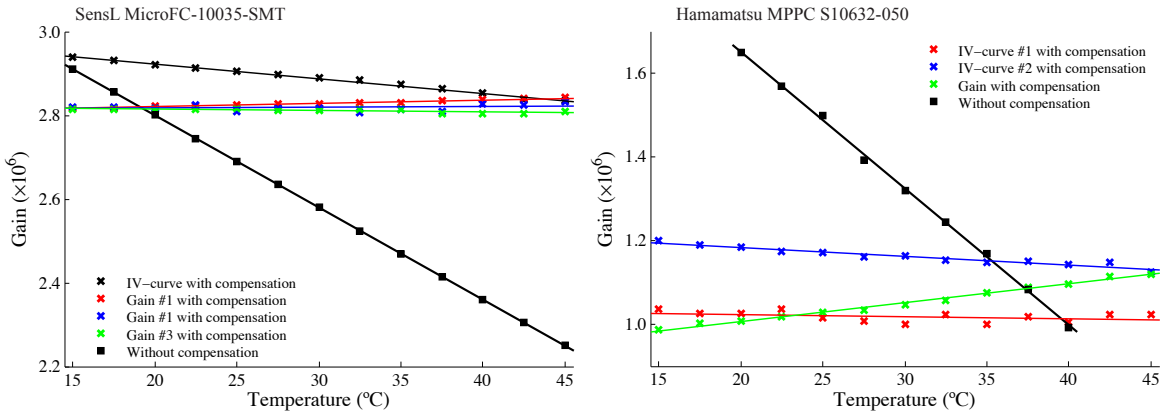

Figure 3.16: SiPM gain fluctuations as a function of temperature for the SensL MicroFC-10035-SMT (left) and the Hamamatsu MPPC S10362-11-050U (right).

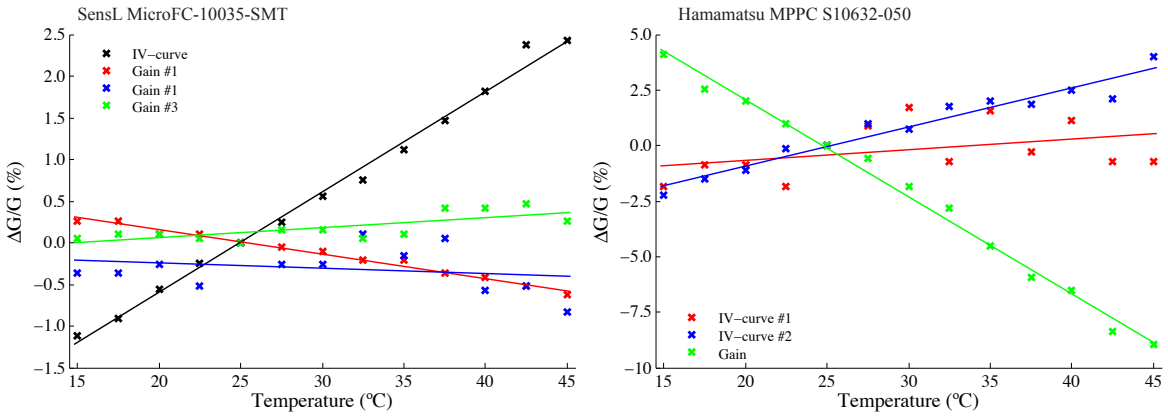

Figure 3.17: SiPM gain fluctuations as a function of temperature for the SensL MicroFC-10035-SMT (left) and the Hamamatsu MPPC S10362-11-050U (right).

having the advantage of not requiring the knowledge to the SiPM parameters, although, the two SiPMs must have the same temperature sensitivity. The authors reported a $\Delta G/G$ ~5%. For the SensL SiPM a $\Delta G/G$ ~0.5% was observed. From the pulse high spectrum obtained for the SensL SiPM (Figure 3.18), one can verify that the gain slightly diminished at higher temperature. The possible explanation to this observation is the possible variation of room temperature affecting the LED and/or electronics, since the acquisition of all pulse high spectrum takes ~4 hours. Future studies will be conducted to access possible factor leading to gain variation even when the system is automated in order to compensate temperature variations with SiPM bias voltage adjustment.

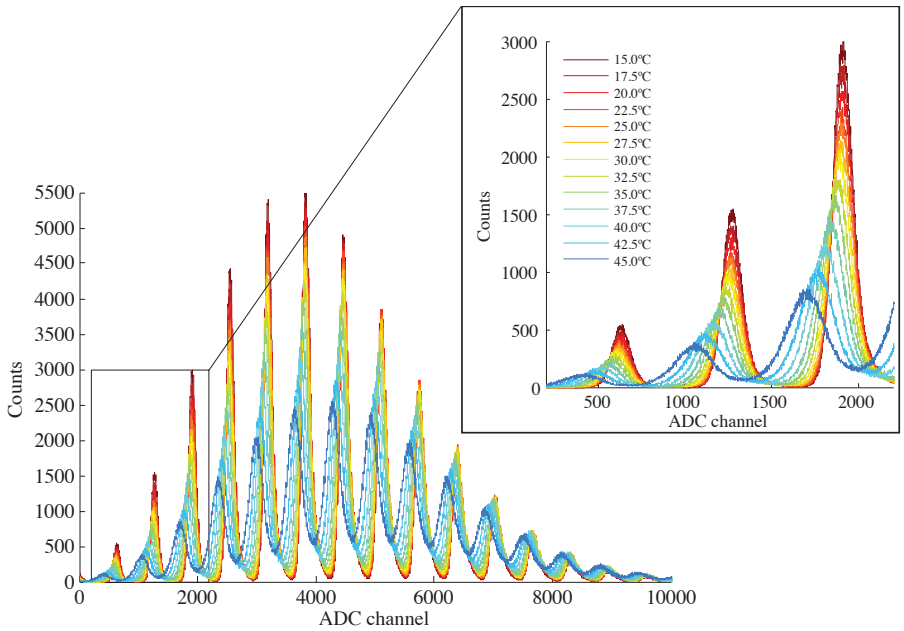

Figure 3.18: Pulse-height spectrum's for the SensL MicroFC-10035-SMT for several temperatures with gain correction in the 15 - 45 °C temperature range.

3.4.5 Photon-detection efficiency of VUV-sensitive SiPM prototypes

Several applications envisage the detection of UV or VUV light. Common solutions require a WLS material to match the photodetector highest quantum efficiency. Similar to the NEXT experiment, experiments with SiPMs for imaging in noble gas detectors, namely for $\beta\beta$ decay and Dark Matter experiments are pushing to the development of VUV-sensitive SiPMs [60].

PDE measurement for the SensL SiPMs

New SiPMs prototyped by SensL with improved PDE in the UV range were characterized. This characterization was performed by the photocurrent method, by measuring incident light flux with a calibrated PMT and determining the number of incident photons, as described in [68]. For the purpose, a xenon lamp (Hamamatsu Photonics E7536, 150 W) was used, coupled to a monochromator. To obtain the spectrogram of the input light an optical fiber was coupled to the monochromator output and coupled to an integrating sphere. A Hamamatsu Photonics Multichannel Analyzer C10027 spectrometer with a monochromator was used. The SiPMs were placed inside a dark box built for the purpose. The light from the monochromator is guided into the dark box by a quartz optical fiber. To control the illumination level, a diffraction lens and various collimators were used [69]. A polished Polytetrafluorothylene (PTFE) reflector was placed facing the light entrance port from the quartz optical fiber. The SiPMs and PMT are facing the PTFE plane and the distance can be adjusted. In these studies the photodetector plane was at 850 mm distance from the PTFE plane. The measurements were performed at room temperature (25 °C). The setup was intended for a preliminary characterization of the PDE response range of these SiPMs. Afterwards, it was verified that the illumination conditions weren't ideal. For that reason no absolute values of the PDE are presented.

These SensL SiPM samples present a window cap that can be removed so that the silicon layer can be exposed directly to the light. The PDE was measured for the SensL SiPMs with (CAP) and without the cap (NO-CAP). The normalized response as a function of the wavelength is depicted in Figure 3.19. For comparison, preliminary data provided from the vendor is included. The samples show higher sensitivity to the visible region of the spectrum, mainly in the blue region as the majority of the SiPMs available in the market. As expected, by removing the window (CAP) the sensitivity at lower WLs is improved. The measured sensitivity over the analyzed wavelength range is ∼10% lower than the data provided by SensL. The PDE depends of three factors: geometrical efficiency, quantum efficiency and triggering probability (see Eq. 2.3). In a practical way, PDE changes with the photon wavelength and overvoltage level. As mentioned in Section 2.4.2, the photon detection efficiency can be measured by photo-current method or pulse-mode method. Typically the PDE obtained by the current method is overestimated due to the contribution of the after-pulsing and crosstalk to the total number of photons measured. This could explain the difference from the obtained results and the ones provided by the manufacturer.

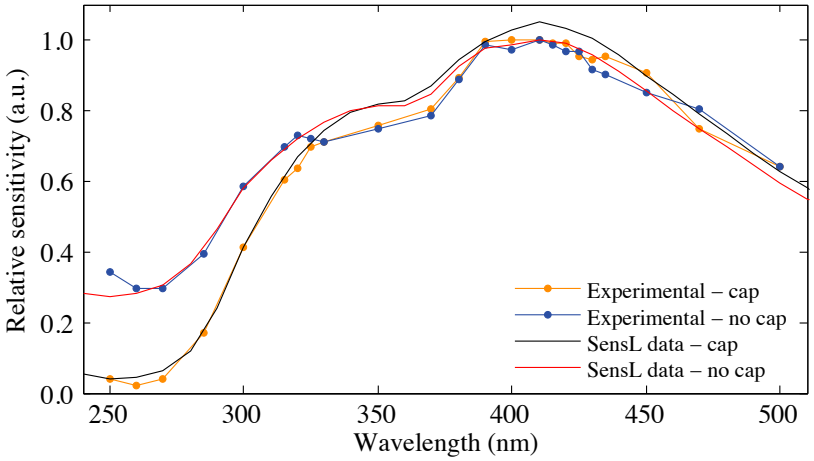

Figure 3.19: Experimental PDE measurements for SensL SiPM samples and comparison to the manufacturer provided data.

Hamamatsu VUV-sensitive MPPC prototypes

Two Hamamatsu VUV-sensitive MPPC samples, of 3×3 mm^2 sensitive area and 50×50 μm^2 pixel, with manufacturer references VUV2-A0023 (sample 1) and VUV2-A0024 (sample 2) were evaluated. The relative photon detection efficiency study was performed in the 160 − 300 nm spectral range using a deuterium lamp. The lamp is coupled to a vacuum monochromator (VM-502, Princeton Instruments). The SiPMs were placed in a vacuum chamber coupled to the monochromator (Figure 3.20). For light diffusion a fused silica diffuser sanded with 220 grit polishes (DGUV10-220, Thorlabs) was used. At a pressure of 10^{-4} mbar, the number of incident photons was measure with a PMT (R8520-0SEL, Hamamatsu) and the output current was read at the first dynode (no gain). The SiPMs were biased at recommended voltages (∼67 V) with a gain of 1.25×10^6 at 25° C. To identify the linear response of the SiPMs, the light intensity was varied by adjusting the monochromator slits. The number of incident photons was determined with the calibrated PMT (R8520-0SEL, Hamamatsu). PDE measurements were performed for SiPMs gain of 1.25×10^6 at 25 °C.

Results shown that SiPMs response was linear for low light levels, corresponding to slit apertures lower than 1.5 mm (Figure 3.21). For a 1 mm slit aperture, the VUV-SiPM relative PDE was measured using the same method as before. The results obtained show a 25% PDE at 170 nm, which is lower than the reference value of 30%, as claimed by the manufacturer (also determined using the photo-current method).

To improve the PDE measurements, a new setup is being prepared, allowing to perform the PDE study in pulse mode, thus allowing to discard the contribution from crosstalk and afterpulsing, which highly contribute to the PDE measurement. In addition, a complete characterization of this new SiPMs will be performed soon.

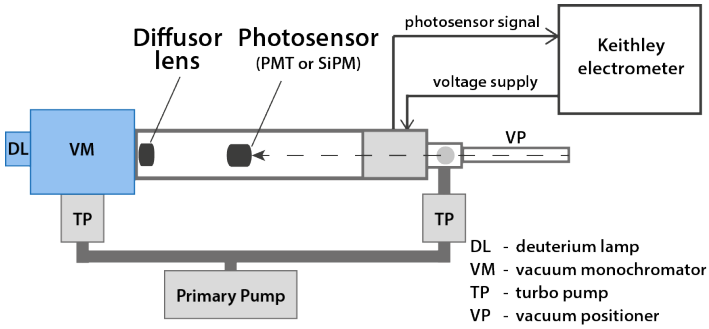

Figure 3.20: Schematic of the experimental setup to measure relative PDE of VUV-sensitive SiPM samples.

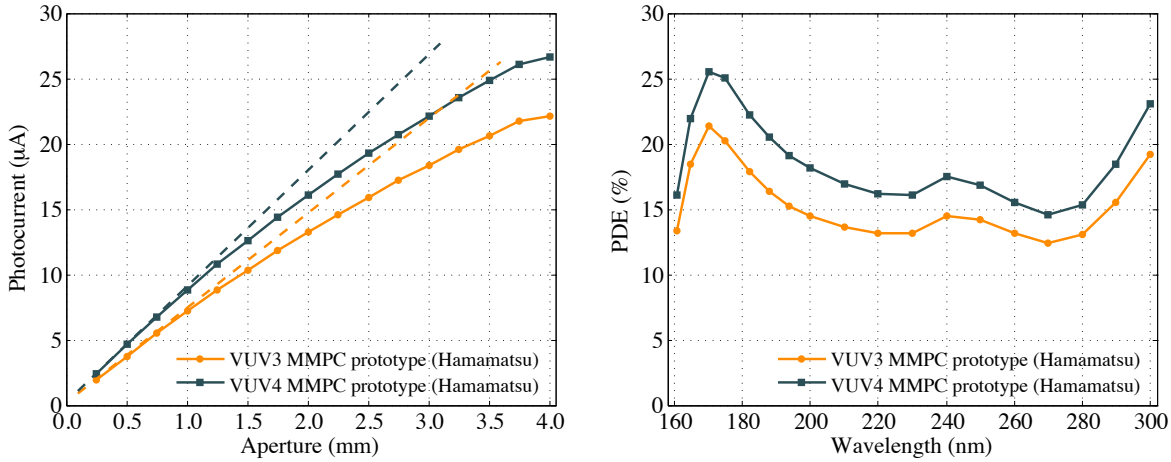

Figure 3.21: VUV-SiPM response at 170 nm for different light intensities (left) and VUV-SiPM relative PDE in the 160 – 300 nm region.

3.5 Studies on scintillating optical fibers

The application of scintillating optical fibers in high energy physics namely for particle detection has been well studied. Examples of applications are charged particle tracking [70] or hadronic calorimeters [71]. Other works use WLS optical fibers for 2D imaging [72, 73]. In concept, a large area tracking plane based on scintillating optical fibers would be feasible for application in a large gaseous TPC. Introductory studies on SOF and WLS fibers are presented here.

3.5.1 BCF12 emission spectrum

The characterization of the BCF-12 scintillating optical fiber emission spectrum was performed by irradiating the fiber with X-rays. The X-ray tube used was an Oxford Instruments series 5000, with molybdenum anode, 125 μm Be window and 25° cone angle. The voltage was set to 50 kVp and the current to 800 μA. A BCF-12 fiber, 15 cm long was placed at 2 cm from the X-ray tube window and perpendicularly to it, so only a small portion of the fiber was irradiated. An Oceans Optics USB4000 portable spectrometer was used for

the measurements of the scintillation emission of the fiber.

From the obtained emission spectra (Figure 3.22), the BCF-12 scintillating optical fiber reveals a maximum emission at 430.9 nm, followed by a second peak at 475.2 nm. Notwithstanding that the manufacturer data sheet indicates a value of 435 nm without this second peak, other studies presented a similar behavior. Therriault-Proulx *et al.* [74] obtained for the BCF-12 scintillating optical fiber an emission spectrum in the $400 - 600$ nm range, with a maximum at 450 nm and a secondary maximum at 525 nm. Archambault *et al.* [75] experimentally measured the emission spectra for BCF-12, obtaining an emission peak at 438 nm and an apparent second peak at ∼460 nm. The possible explanation for the result obtained in this study can be related to the improved resolution of the Oceans Optics USB4000 portable spectrometer, with 16-bit ADCs, over other spectrometers.

For comparison, the measurements were repeated for a wavelength shifting fiber, BCF-91A (Saint-Gobain) and the obtained spectrum is depicted in Figure 3.23. For BCF-91A a similar response has been previously observed for the same WLS fiber [76]. Jang *et al.* evaluated the fast BCF-92 WLS optical fiber, equivalent to the BCF-91A WLS fiber but with a shorter decay time (2.7 ns). The author's irradiated a sensitive probe consisting in an

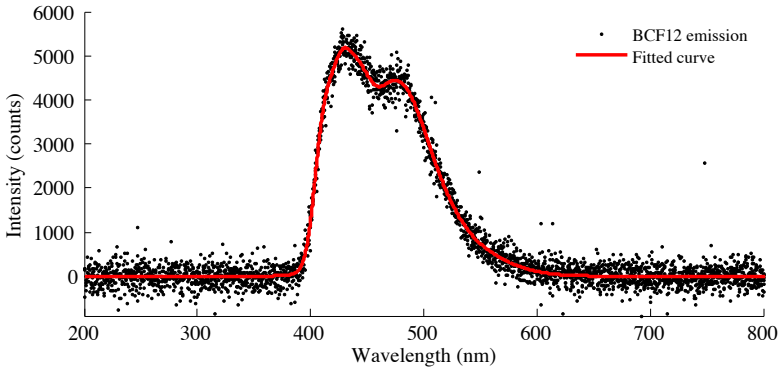

Figure 3.22: Emission spectrum for the BCF-12 scintillating optical fiber when irradiated with 50 kVp X-rays.

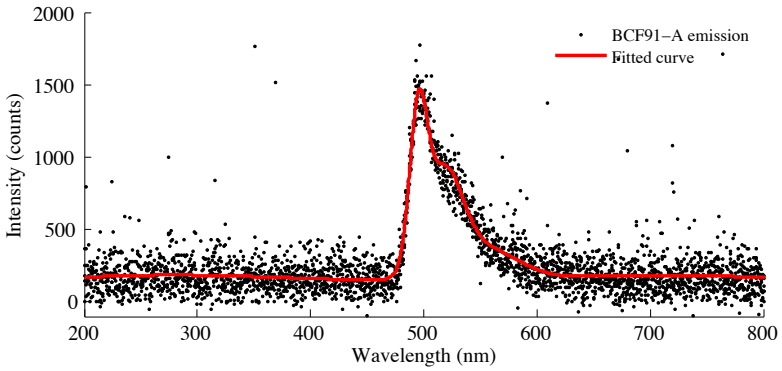

Figure 3.23: Emission spectrum for the BCF-91A scintillating optical fiber when irradiated with 50 kVp X-rays.

Ø1 mm and 1 cm long BCF-92 fiber coupled to a 20 m long PMMA optical fiber (SH4001). The probe was irradiated with 88 keV γ-rays from a ^{109}Cd source. The author's presented data show the same behavior has the one observable in this study, and therefore the double emission peak of the BCF-12 shouldn't be related to the spectrometer.

3.5.2 Readout of scintillating optical fiber in coincidence mode

This configuration uses two MPPCs that read in coincidence the light output at each extremity of a 1.5 m-long BCF-12 single-clad scintillating fiber. A ^{137}Cs source with an activity of 4.25 μCi was used and aluminum filter was added for beta particle blockage. The reference voltage of the comparators was set as low as 0.5 photoelectrons (p.e.). For coincidence operation, a dedicated electronics readout system was developed, including a transimpedance amplifier, units for threshold detection and signal coincidence. Due to the fast scintillation decay time of 3.2 ns, fast electronics are needed to allow a pulse rise time as close as possible to the scintillation decay time. The circuit developed consists of an OPA656 at the 1st stage for charge-to-voltage conversion followed by an OPA847 for a 40 V/V gain at the 2nd stage. Two MAX9011 (MAXIM Integrated) fast comparators (propagation delay of 5 ns) were used. The logic unity is a SN74AUC1G08 single 2-input positive AND gate (Texas Instruments). A MCA 8000A (Amptek) was used for signal acquisition. The experimental system used for the coincidence measurement is presented in Figure 3.24.

The results obtained when operating the system both with and without the coincidence circuit are presented in Figure 3.25. For comparison, dark noise spectra were also obtained (without the presence of the radioactive source). All spectra were obtained with the same acquisition time. Acquisition without the radiation source shows that thermal noise is mainly below 4–5 p.e. at 26 °C but with a strong impact on the spectral distribution, contributing

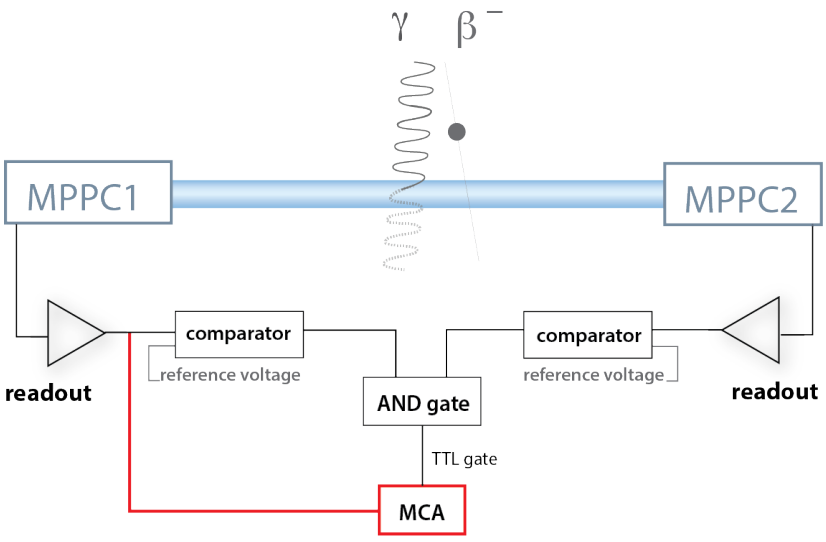

Figure 3.24: Experimental setup for tests of the coincidence mode readout electronics and future TOF tests.

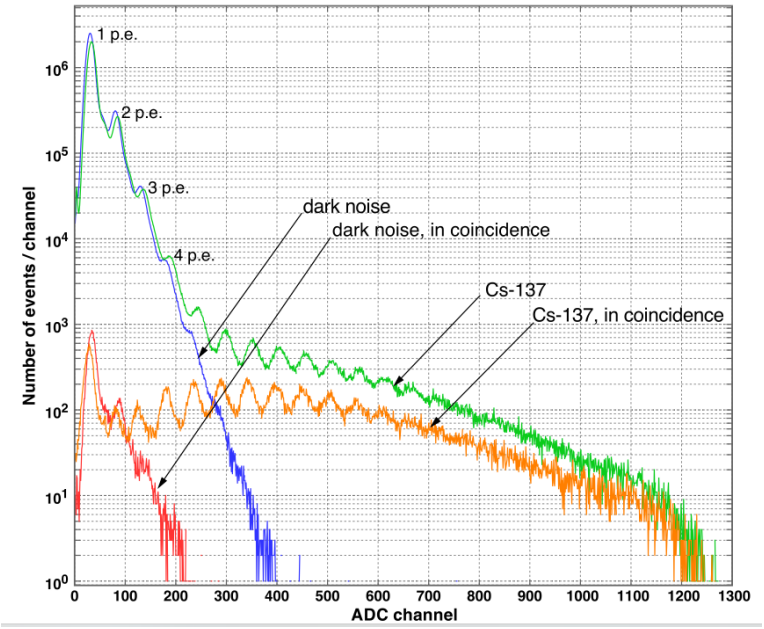

Figure 3.25: Coincidence mode pulse-high histograms with and withoud radiation.

with a large number of false events. The strong reduction of dark noise events down to residual values is clearly visible when operating in coincidence mode. Considering the symmetry of the electronic circuitry (both MPPC1 and MPPC2 could initialize the coincidence), the rate of these accidental coincidences (N_{acc}) is below the rate given by $N_{acc} = 2N_1N_2\tau$, where N_1 and N_2 are the rates of MPPC1 and MPPC2, respectively, and τ is the AND gate width. Because N_1 is approximately equal to N_2, $N_{acc} = 2N_1\tau$. When the radiation source is used in coincidence mode, only events from the source are detected, and most of the dark noise events are rejected. In coincidence mode, also some of the scintillation events are undesirably rejected, suggesting the need for optimization of the electronic coincidence system.

3.6 Final remarks

These first three Chapters complete the Part I of this document. The work described is related to the NEXT experiment and the SiPMs which are the main component of the tracking plane. During Ph.D period I participated in R&D tasks abroad, namely a 3-month period at LBL (Berkeley, USA) and several month-periods at IFIC (Valencia, Spain). As NEXT collaborator, I have co-authored several works published elsewhere [12, 34–36, 42, 44–46, 57–60, 77–82].

A high energy resolution and low background are the two essential factors for a $0\nu\beta\beta$ experiment. The components for the NEXT detector are tested for radioactivity levels. The Hamamatsu MPPC S10362-11-050U was the initial SiPM chosen for the NEXT tracking plane. Notwithstanding, the SensL MicroFC-10035-SMT was recently adopted has the SiPM for the NEXT tracking plane due to their low radioactive footprint. The gammas emitted in

^{208}Tl and ^{214}Bi decays are the the main source for background. For the SensL SiPM, were obtained activities of 3×10^{-5} mBq and 9×10^{-5} mBq for ^{208}Tl and ^{214}Bi, respectively [12].

The studies here presented are a first analysis to the new SensL SiPM. Some features reveal the evolution of the SiPM technology. The SensL SiPM is a new generation SiPMs showing lower operation voltage, lower crosstalk and lower dark noise. The dark noise includes primary pulses (uncorrelated) mainly due to carriers thermally generated in the depletion regions of MPPC μcells and secondary (correlated) pulses due to afterpulsing and crosstalk effects [83]. In the studies here performed, afterpulsing wasn't evaluated. Further studies should address this aspect.

Hamamatsu provived samples of a new SiPM with improved sensitivity for the VUV range and with expected lower radioactivity. Further studies will be conducted for characterization of these samples and PDE measurement in the VUV range for all the SiPM candidates for integrating the NEXT tracking plane.

Part II

Applications of the developed technologies

Chapter 4

Application case: Dosimeter for Brachytherapy

4.1 Motivation

The growing cancer incidence is a major public health concern and a subject of wide attention. Nowadays, cancer is the leading cause of disease worldwide and accounting 14 million new cases are diagnosed each year. Prostate cancer is the fourth cancer of highest incidence worldwide and the most common cancer in European men. The *World Health Organization* (WHO) forecast a 75% increase of new cancer cases until 2030, which translates into about 22 million new cases per year. Despite the high incidence of prostate cancer, the survival rate is high due to a prompt diagnosis combined with innovative therapies. Nowadays a screening test like *prostate specific antigen* (PSA) blood test allows an early stage detection [84, 85]. Typically, in low or medium risk prostate cancers PSA levels are below 20 ng/mL, being eligible for less severe treatment options such as prostate brachytherapy. Prostate brachytherapy has several modalities that translate into different systems and techniques of radiation delivery to the patient [86, 87]. The two most common are *Low-Dose-Rate* (LDR) also know as seed brachytherapy and *High-Dose-Rate* (HDR) brachytherapy.

LDR brachytherapy is one of the most safe and efficient treatments [88–91], although several deviations from treatment plan can occur. One issue is the possibility of radioactive material misplacement, that besides increasing the risk of tumor under-dosage and normal tissue over-dosage [92–95], will induce higher risks to the patient by increasing treatment side effects such as bleeding, urinary incontinence, infertility, etc. In addition, cases have been reported of radioactive seed migration (*e.g.* to the chest) in patients treated for prostate cancer by LDR brachytherapy [96–98]. Other issues result from needle displacement, prostate deformation [99], seed drifting along the needle path, blood flow, oedema, seed migration, gland motion and anatomic changes (e.g., colorectal gas, stomach filling, and bowel distension) [100].

In a study conducted by Able *et al* [101] the procedures of HDR brachytherapy were evaluated in order to assess the quality of treatment delivery. The authors stated that the potential for error is relatively high due to the many individual tasks which must be interwoven into a team approach for successful treatment delivery. The recommended *quality assurance* (QA) procedures for HDR brachytherapy only test whether individual aspects of HDR brachytherapy treatment (source strength, catheter length, and other factors) are within set tolerance values. The 1997 American Association of Physicists in Medicine (AAPM) Task Group 56 [102] recommends a dose delivery accuracy of 5-10% and a positional accuracy of ± 2 mm. Almost twenty years later, there is no device in the market capable to perform *in-vivo* dosimetry in real-time and integration with treatment planning software, which would allow performing real-time corrections during brachytherapy treatments. Over the last decades, technological advances allowed new treatment options and imaging techniques using low doses of ionizing radiation [103]. Vaz [103] identifies several topics which the *International System of Radiological Protection* (ISRP) should address, namely accidents in HDR brachytherapy, patient exposure tracking, radiation risk assessment in radiotherapy and hybrid modalities and development of strategies and methodologies for radiation risk communication to patients.

Incorrect dose delivery during treatments is a reality and currently there is no device capable of performing real-time *in-vivo* dose measurements, making it impossible to perform real-time dose correction. The prostate periphery and apex are regions of high-dose gradient being prone to treatment delivery errors. Dosimetry has a major importance in the efficiency of ionizing radiation treatments. It can be challenging in some modalities, such as in Prostate LDR-brachytherapy, where nowadays the only possible quality control is by postoperative imaging techniques such as Computed Tomography (CT) for seed distribution mapping [104] or ultra-sound imaging during treatment procedures [105]. Interest in real-time *in-vivo* dose monitoring has grown with the increase of complex and time-dependent radiotherapy modalities [100]. The QA through *in-vivo* dosimetry in radiation therapy is mandatory in some countries and largely recommended for some radiotherapy modalities [106]. However, due to the specificity of these prostate brachytherapy techniques, there is no commercial device capable of doing so.

The interest for *in-vivo* dosimetry in brachytherapy is growing and the effort from research teams and companies translates this need. The *in-vivo* and *in-situ* measurement of the radiation dose administered during brachytherapy faces several technical challenges, requiring a very compact, tissue-equivalent, linear and highly sensitive dosimeter, particularly in low-dose rate brachytherapy procedures, which use radioactive seeds with low energy and low dose deposition rate. Dosimeters based on fiber optic probes are the most promising approach up to this date and are a trend in research for small field dosimetry and *in-vivo* dosimetry in radiotherapy, namely for brachytherapy, *external beam radiotherapy* (EBRT),

Intensity-Modulated Radiation Therapy (IMRT) and 2D scintillation dosimetry for beam characterization in linear accelerators.

In the context of these Ph.D. studies, a dosimeter employing disposable sensitive probes based on a scintillating optical fiber was developed. The low size and high flexibility of the disposable probe allows the introduction in the region to treat and subsequent monitoring of the dose in key areas such as areas of high dose gradients where the tumor is located and areas where excessive radiation dose can damage healthy organs and tissues. In addition, the developed dosimeter allows *in-vivo* and real-time dose measurements opening the possibility for real-time dose correction.

4.2 Dose

4.2.1 Dose quantities

Guidelines regarding dosimetry and dosimetric quantities are mainly provided by the *International Commission on Radiation Units and Measurements* (ICRU) and *International Commission on Radiological Protection* (ICRP). While ICRU is related to the operational quantities and to the physical aspects of dosimetry, ICRP considers the biological effects of radiation in human body, providing recommendations related with radiation protection and establishing radiation protection quantities [107].

These protection quantities are primarily limiting dose quantities and take into account human body properties, while operational quantities refer to monitoring of external exposure. These protection and operational quantities are both related by the directly measurable physical quantities: *fluence* (Φ), *kinetic energy release per mass (KERMA)* (K) and *absorbed dose* (D). Φ relates to the number of particles or photons crossing over a sphere of unit cross section, KERMA to the ionizing effect of the radiation field and D to the deposited energy per unity of mass (Figure 4.1).

For a monoenergetic ionizing radiation beam, the particle *fluence* (Φ) can be used to characterize the radiation field. By definition, Φ is

$$\Delta\Phi = \frac{dN}{dA} \tag{4.1}$$

where dN corresponds to the number of incident particles in a small sphere with differential cross-sectional area dA [109, 110] and is expressed in m^{-2} units (SI). The energy fluence (Ψ) (in $\mathrm{J.m}^{-2}$) can be calculated from the particle fluence [110],

$$\Psi = \frac{dN}{dA}E = \Phi E \tag{4.2}$$

where E is the particle energy and dN the number of particles with energy E [110]. For polyenergetic particle beams particle fluence spectrum ($\Phi_E(E)$) and energy fluence spectrum

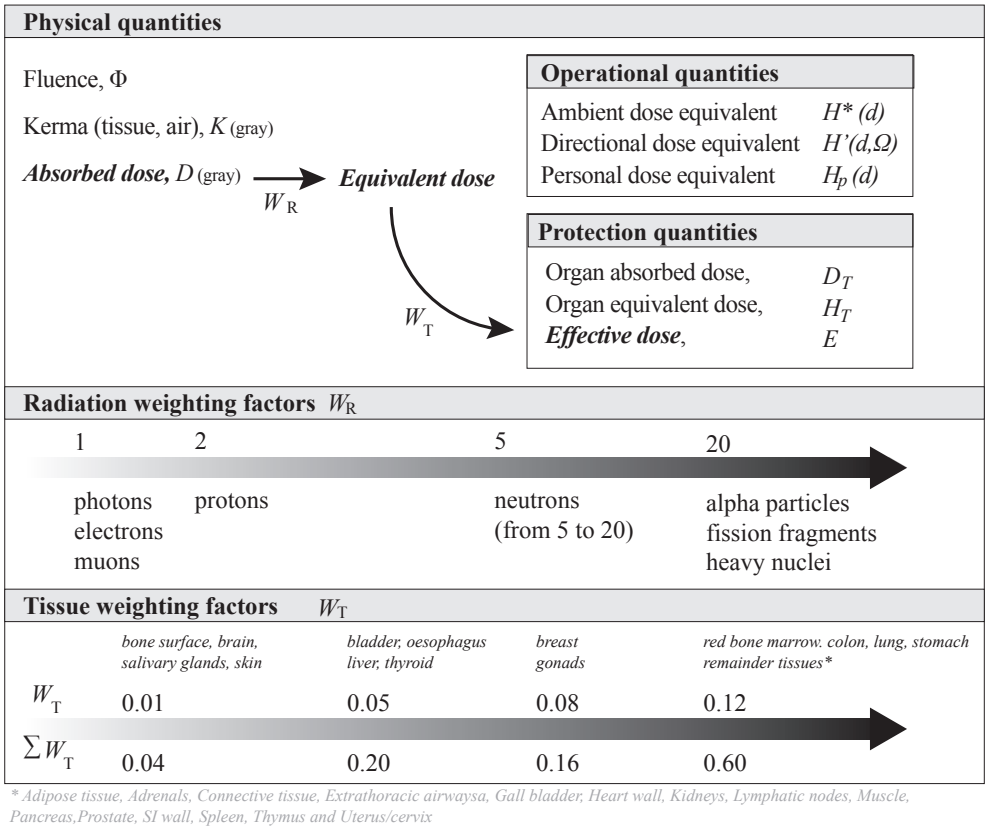

Figure 4.1: Relationship between reference radiation fields, physical protection and operational quantities. Adapted from [107, 108].

$(\Psi_E(E))$ are considered. By definition, particle fluence spectrum in energy E is

$$\Phi_E(E) \equiv \frac{d\Phi}{dE}(E) \tag{4.3}$$

and the energy fluence spectrum is

$$\Psi_E(E) \equiv \frac{d\Psi}{dE}(E) = \frac{d\Phi}{dE}(E)E \tag{4.4}$$

KERMA is the initial kinetic energy of all charged particles originated by ionizing radiation corresponding to the energy given by a photon per unit of mass for a given material. The SI unit of KERMA is gray (Gy) corresponding to 1 joule per kilogram.

Although KERMA dose and absorbed dose are expressed in the same units they are different quantities, KERMA is a measure of the whole transfered energy by an uncharged particle (photon or neutron) to primary ionizing particles while the absorbed dose is a measure of the absorbed energy by unit of mass [111].

According to *American Brachytherapy Society* (ABS) orientations, the air KERMA strength of each new source should be independently measured and compared to vendor specifications. Dose calculation should be performed in accordance with the TG43 (1995)

[112] and TG43U1 (2004) [113] formalisms. The prescribed dose will be the intended minimum dose delivered to the planning target volume (PTV).

The energy fraction of a radiation field that is absorbed in the body is energy dependent, so it is useful to distinguish radiation exposure from *absorbed dose* (D). Regarding dosimetry, the main physical quantity is D, expressed in gray (Gy) units, as mentioned before. The absorbed dose corresponds to the energy deposited by ionizing radiation per unit of mass of a material:

$$D = \frac{\Delta E}{\Delta m} \tag{4.5}$$

The radiation effects in the human body are not well defined from the absorbed dose point of view, since these effects depend on the nature of radiation, how it distributes in the body and on the radio-sensitivity of the tissues and organs. By these reasons, other quantities are defined. According to the *International Atomic Energy Agency* (IAEA) [108], radiation can be characterized as weakly or strongly penetrating as a function of which dose equivalent is closer to its limiting value. For strongly penetrating radiation the limiting quantity is the effective dose equivalent, while for weakly penetrating radiation the dose equivalent to the skin and to the lens of the eye is the limiting quantity.

Protection quantities

Protection quantities are not directly measurable, nevertheless they can be calculated from the absorbed dose by using weighting factors (dimensionless) for radiation (W_R), tissue (W_T) or anthropomorphic phantoms (*effective dose*, E_{eff}). ICRP recommended values for the tissue-weighting factors can be found in [114, 115]. These quantities are used as reference for observed radiation effects on the body, allowing to set exposure limits. In the scenario of full body irradiation, W_R is the only weighting factor to consider since the sum of W_T corresponds to the unit ($\sum W_T = 1$). The *organ equivalent dose* (H_T) and E_{eff} are weighted averages of absorbed dose and are related to stochastic health effects of radiation. These two quantities are expressed in *sievert* units (Sv).

To obtain E_{eff}, one calculates the *absorbed dose* (D) (in *gray*) corrected for the radiation type (obtaining H_T) and then the former is corrected for the tissue or organ. The organ or tissue equivalent dose (H_T) is defined by

$$H_T = \sum_R W_R . D_{T,R} \tag{4.6}$$

where $D_{T,R}$ is the absorbed dose in tissue T by radiation type R [116]. The effective dose, E_{eff} is defined as

$$E_{eff} = \sum_T W_T . H_T = \sum_R W_R . D_{T,R} \tag{4.7}$$

Operational quantities

To relate the protection quantities to instruments and dosimeters, operational (or dosimetric) quantities based on point doses determined at defined locations in specific phantoms are used [107]. These quantities are personal ($H_p(d)$), directional (H',(d,ω)) and ambient ($H^*(d)$) dose equivalent and have the same unit, *sievert* (Sv).

The *ambient dose equivalent* ($H^*(10)$) is the operational quantity for area monitoring. By definition, it is the dose equivalent produced at a point of interest in the real radiation field by the corresponding aligned and expanded radiation field in a 300 mm diameter sphere of unit density tissue (ICRU-sphere phantom [116]) at a depth of 10 mm in the radius vector opposing to the direction of the aligned field [107].

The *directional dose equivalent* ($H'(d,\omega)$) allows the calculation of equivalent dose to tissue or organ for the different radiation types. By definition, the directional dose equivalent at a point of interest in the actual radiation field, is the dose equivalent that would be produced by the corresponding expanded radiation field, in the ICRU sphere at a depth d. The point is lying on a radius which has the direction ω [107]. Typically, a depth (d) of 0.07 mm, 3 mm and 10 mm are used for dose equivalent in skin, eye lens and deeper laying organs, respectively [107].

The *personal dose equivalent* ($H_p(d)$) is the operational quantity for individual monitoring and corresponds to the dose equivalent in soft tissue (ICRU-sphere phantom [116]) at a point located at a certain depth, d, and can be used at both surface or organ dose [107, 117]. As highlighted by Bartlett [117], this quantity is defined at a location where the detector cannot be placed, causing difficulties in the definition of both the point of test and dosimeter reference point for calibration.

4.2.2 In-situ dosimetry and the Cavity theory

Radiation detectors typically mismatch the composition (atom-number, density) of the medium for which dose value is desired. When a detector doesn't provide a direct measure of the dose in the medium, the dose determination relies on both measurements and calculations.

The cavity theory assumes that the presence of the detector originates a cavity in the medium. This allows relating the absorbed dose by a dosimeter (D_{cav}) to the absorbed dose in that medium (D_{med}) in the absence of the detector. If the detector material has radiation absorption properties similar to those of the tissue, one can rely on the Bragg-Gray cavity theory for measuring tissue dose directly [111].

The Bragg-Gray theory was the first cavity theory proposed. This theory is based on the assumption that the wall cavity must be small when compared to the range of secondary charged particles produced by photons in the cavity medium, so that the presence of the detector does not perturb the fluence of charged particles in the medium [110, 118]. Considering that this theory doesn't consider photon interaction, the only contribution to the

absorbed dose is due to charged particles, meaning that no secondary electrons are produced inside the cavity and that no electrons stop within the cavity volume [110]. By the Bragg-Gray cavity theory, the *dose in the medium* (D_{med}) relates to the *dose in the cavity* (D_{cav}) as follows [110]:

$$D_{med} = D_{cav}\left(\frac{\overline{S}}{\rho}\right)_{med,cav} \tag{4.8}$$

where $(\overline{S}/\rho)_{med,cav}$ is the ratio of the average unrestricted mass collision stopping powers of the medium and the cavity [119]. The Bragg-Gray cavity theory assumes that the particle fluence does not change over the cavity and that the deposited energy is only due to charged particles and does not consider secondary electrons with sufficient energy to produce further ionization in the detector volume. The deviation of measurements from the Bragg-Gray theory was severe for smaller cavities, such as the ionization chambers with small air cavities and high-Z walls [118].

The Spencer-Attix cavity theory [110] takes into account delta electrons. The Spencer-Attix cavity theory relates D_{med} to D_{cav} as

$$D_{med}/D_{cav} = S_{med,cav} \tag{4.9}$$

where $S_{med,cav}$ is the ratio of the mean restricted mass collision stopping powers of the medium to that of the cavity. Considering the medium electron fluence spectrum $\Phi^{e-e}_{med,E_K}(E_K)$, $S_{med,cav}$ is [110]

$$S_{med,cav} = \frac{\int_{\delta}^{E_{K0}} \Phi^{e-e}_{med,E_K}(E_K)(L_{\delta,med}/\rho)d(E_K) + TE_{med}}{\int_{\Delta}^{E_{K0}} \Phi^{e-e}_{med,E_K}(E_K)(L_{\Delta,cav}/\rho)d(E_K) + TE_{cav}} \tag{4.10}$$

where TE_{med} and TE_{cav} are track end terms and account for a part of the energy deposited by electrons with initial kinetic energies between Δ and 2Δ [110]. A deeper analysis of the Spencer-Attix cavity theory can be found in [110] and revisions can be found in [120] and [121].

An extended cavity theory, the Burlin theory, considers both electron and photon absorption in the cavity and is applied to intermediate size cavities. This theory introduces a weighting parameter d as a cavity limit to the Spencer–Attix equation [110]. This method has been considered too simplistic and the Burlin cavity theory in no longer used in practice [110].

4.2.3 Dose formalism

The AAPM Task Group No. 43 report [112] provides the protocol for the dose calculation to brachytherapy sources. The dose rate $\dot{D}(r,\theta)$ at a point of interest $\mathrm{P}(r_0,\theta_0)$ due to a sealed

brachytherapy source can be determined in two dimensions 2D, as [112, 110]:

$$\dot{D}(r,\theta) = S_K.\Lambda.\frac{G_L(r,\theta)}{G_L(r_0,\theta_0)}.g_L(r).F(r,\theta_0) \tag{4.11}$$

with $r = \sqrt{d_a^2 + x^2}$ and $\theta = \arctan(d_a/x)$ where r is the distance (cm) from the origin to the point of interest P, θ is the angle between the direction of radius vector r and the long axis of the source, θ_0 defines the source transverse plane and is equal to $\pi/2$ radians, S_K is the air kerma strength of the source ($\mu Gy\text{m}^2\text{h}^{-1}$) and $G_L(r,\theta)$, $g_L(r)$ and $F(r,\theta)$ are the geometric, radial dose and anisotropy functions, respectively. Λ is defined as the dose rate to water at a distance of 1 cm on the transverse axis per unit air kerma strength source in water [110]:

$$\Lambda = \frac{\dot{D}(r,\theta)}{S_K} \tag{4.12}$$

4.3 Challenges in dosimetry for prostate brachytherapy

4.3.1 Prostate LDR and HDR Brachytherapy

Brachytherapy is a minimally invasive technique in which the radioactive material is placed near (intracavitary) or inside (interstitial) the treatment area, making it a common treatment for breast, prostate and melanoma cancers. This is the main treatment option for prostate cancer when it is diagnosed at early stages. In addition, brachytherapy is also applied as a boost therapy in advanced stage prostate cancers [122]. Prostate brachytherapy has the particularity of placing the radioactive material inside the prostate, allowing a localized irradiation of the tumor, seeking to minimize damage to healthy tissues and organs. This treatment is divided into two different modalities based on isotope and dose rate (Figure 4.2).

LDR prostate brachytherapy uses permanent implantation of small ^{125}I, ^{103}Pd or ^{131}Cs radioactive seeds (with a size close to that of a grain of rice) with energy close to 30 keV. HDR prostate brachytherapy uses higher energy isotopes, typically ^{192}Ir radioactive wires for temporary ($\sim$ 15 min) implantation.

Contrary to LDR prostate brachytherapy, HDR treatments are usually divided in up to three sessions, with a typical duration of 15 min each [122]. Both treatments are ultra-sound guided. The typical isotopes used in prostate brachytherapy are listed in Table 4.1 [123]. The *relative biological effectiveness* (RBE) for low-energy X-rays was found to be very similar to the low-energy gamma-ray brachytherapy isotope ^{125}I [124]. Low-energy X-rays ($40 - 50$ kVp) are used as electronic brachytherapy source (EBS) for ^{192}Ir brachytherapy replacement. The use of ^{131}Cs in prostate brachytherapy is relatively recent (introduced in 2004 [125]). This isotope emits photons with the higher energy (29 keV) and lower half-live (10 days) in LDR prostate brachytherapy.

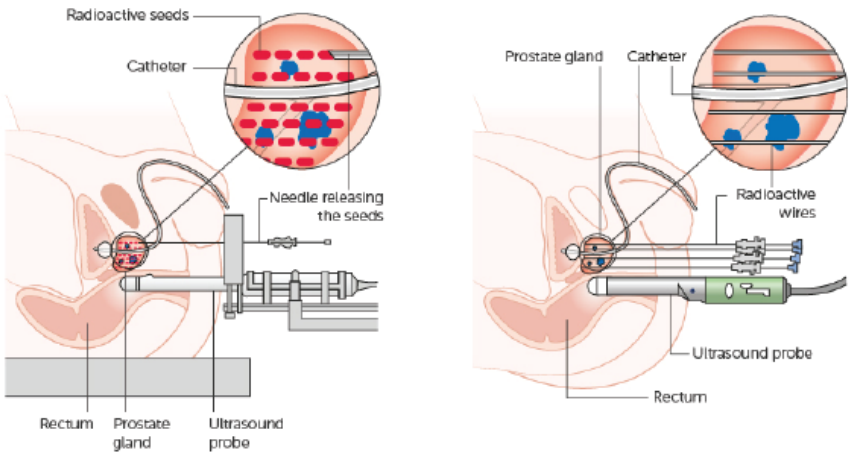

Figure 4.2: (left) LDR prostate brachytherapy treatment scheme, with permanent implantation of small radioactive seeds inside the prostate; (right) HDR prostate brachytherapy using radioactive wires. The wires are introduced in the transperineal region through brachytherapy needles. From [126].

Table 4.1: Most common isotopes for LDR and HDR prostate brachytherapy.

	^{125}I	^{103}Pd	^{131}Cs	^{192}Ir
Year introduced	1965	1986	2004	1960s (afterloader)
Half-life (days)	59.4	16.97	9.7	73.83
Photon energy (average) (keV)	28	21	29	350
Seed spacing	not critical	<1.7 cm		n.a.
Total dose Monotherapy	144 Gy	125 Gy		9.5 Gy BID × 2 6 Gy × 3 fractions × 2
Initial dose rate	7 cGy/hr	18-20 cGy/hr		
Total dose EBRT + BT	108 cGy	100 Gy		9.5 Gy × 2 6 Gy × 3

4.3.2 The ideal dosimeter

Dosimetry is essential for quality assurance and quality control in prostate brachytherapy, allowing real-time verification of the treatment and conceptually making it possible to perform real-time dose correction thus optimizing the irradiation of cancer cells. In addition, radio-sensitive organs must be spared to overdoses resulting from inaccurate source placement. The main concern regarding *in-vivo* dosimetry is patient perturbation, so in that sense the dosimetric system should not add complexity to the treatment. It should give real-time information about dose distribution, envisaging real-time dose correction. Compatibility with imaging systems, such as *Computed Tomography* (CT) and *Magnetic Resonance Imaging* (MRI) is desired in order to establish and monitor both dosimeter and source positions [127]. An ideal dosimeter should present the following characteristics:

- high sensitivity;

- high spatial resolution - brachytherapy sources produce high dose gradients due to their small size [128];
- no dependencies on beam parameters/particle type independence for photons and electrons;
- energy independence;
- real-time dose measurement;
- universality (ability to function with proton and electron beams);
- dose-rate independence;
- dose linearity;
- temperature independence;
- tissue equivalence;
- easy to use and calibrate;
- detectable in the anatomic volume to allow checking its position;
- not expensive, disposable use of its implantable part;
- insensitive to radio-frequency and magnetic fields;
- real-time readout.

In the following section, dosimetry tools and techniques are analyzed, envisaging the best option for real-time *in-vivo* dosimetry in prostate brachytherapy.

4.3.3 Dosimetry tools and techniques

A dosimeter is a device capable of providing a reading correspondent to the dose deposited by ionizing radiation in a sensitive volume. Based on different material properties, the most common dosimetry techniques are *radio-luminescence* (RL), *optically stimulated luminescence* (OSL), *thermoluminescence* (TL), ionization chambers, diodes, diamond and *metal-oxide semi-conductor field effect transistor* (MOSFET).

The ionization chamber is the golden standard for dosimetry, being used for beam calibration in radiotherapy equipments. It has high sensitivity and linearity over a wide energy range. However, its large volume, interference with imaging techniques, high cost and reduced flexibility make it less suitable for *in-vivo* dosimetry applications.

Technologies based on delayed signals like the OSL or the *thermoluminescence dosimeter* (TLD) have limited performance in *in-vivo* and real-time dosimetry. TLDs have to be thermally annealed to erase the residual signal. Semiconductor based dosimeters, such as the MOSFET or the diodes allow a real-time readout and currently are the most suitable options for *in-vivo* dosimetry [129–131]. However, MOSFET dosimeters are prone to radiation damage and have limited life-time. In addition they are not water equivalent.

The first diamond dosimeters are now in the market [132]. These dosimeters are nearly water equivalent for all beam energies, having precise and accurate measurements in photon, electron and proton fields, radiation hardness, minimal energy, temperature and directional dependence and a very small sensitive volume (0.004 mm^3), being suitable for small field dosimetry. Notwithstanding their outstanding properties for beam assessment and small field dosimetry, they are still too bulky for *in-vivo* and *in-situ* dosimetry in brachytherapy.

Currently, the trend for *in-vivo* and real-time dosimetry is towards optical fiber dosimeters. These dosimeters have a sensitive probe consisting of a small volume radio-sensitive material coupled to an optical fiber light guide to the photodetector. The use of scintillators as detection medium is one of the most common options in radiation physics, mainly when fast timing is desired.

Organic scintillators, usually consisting of a fluor dissolved in an organic polymer such as polymethylmethacrylate (PMMA) or polystyrene (PS), are well known for their fast response, low-cost, flexibility, excellent spatial resolution and near-tissue/water equivalence (Figure 4.3). These properties make them a straightforward option for *in-vivo* and real-time dosimetry. Notwithstanding, a non-linear response of organic scintillators has been reported for energies below 200 keV [133–141] as well as a temperature dependence lower than 0.5% per °C [141–143].

In Table 4.2 are listed the main characteristics of the most common techniques for radiation detection. Weighting the *pros* and *cons* of the available techniques for radiation detection, the most suitable technologies for *in-vivo* dosimetry in brachytherapy are the devices based on radioluminescent and scintillator materials, typically applied in fiber optic dosimeters. The main disadvantage of the fiber optic dosimeters is the noise, know as *stem effect*, in the light guide. This effect and the state-of-the-art in fiber topic dosimetry are discussed in the following sections.

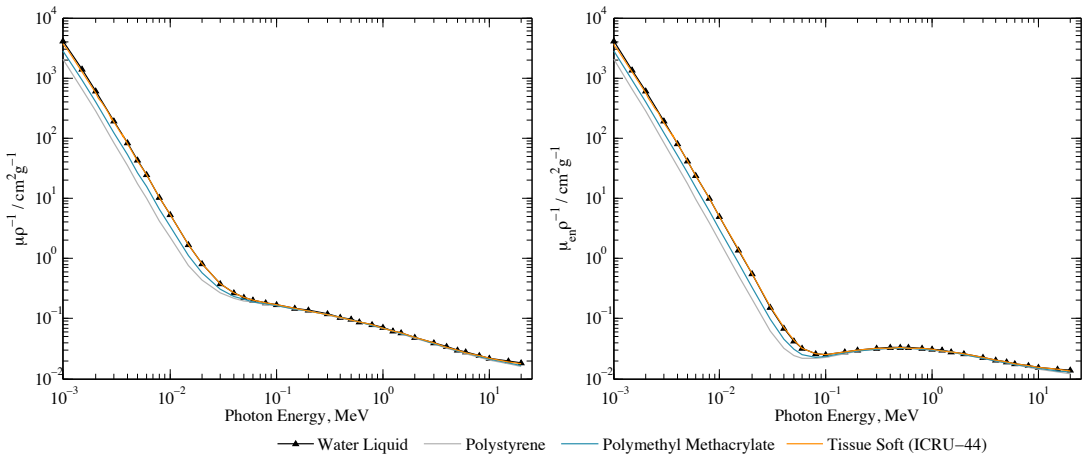

Figure 4.3: X-ray mass attenuation coefficients (left) and mass absorption coefficients (right) for water, soft tissue, polystyrene and polymethyl methacrylate. From [144].

Table 4.2: Radiation detection technologies and their suitability for *in-vivo* dosimetry

Dosimeter type	Pros	Cons
Ionization chamber	fast reference dosimeter	not tissue equivalent requires correction factors bulky expensive
Diode	small dimension real-time readout low cost	not tissue equivalent temperature dependence directional effects dose rate dependence not tissue equivalent
MOSFET	very small size good spatial resolution direct readout low directional effects	not tissue equivalent expensive short life-time
Diamond	almost tissue equivalent radiation hard no directional effects small volume	expensive pre-irradiation energy dependence temperature dependence (small)
OSL TLD	stability no directional effects dose rate independence	laser readout non real-time readout Cherenkov
Radiographic film	2D dosimetry good spatial resolution permanent info low cost	non real-time readout no linearity calibration prior usage
Organic scintillators	small volume good sensibility good spatial resolution dose rate independence fast readout direct readout no need for correction factors	Cherenkov slight temperature dependence [142, 145] dependence at low energies
Inorganic Scintillators	slower than organic scintillators	temperature dependence

4.4 State-of-the-art in fiber optic dosimeters

4.4.1 Introduction

The first works on fiber optic sensors for ionizing radiation detection are dated from the decade of 1990 [134, 146–149]. Typically, these dosimeters use a radio-sensitive material for conversion of gamma radiation into visible light, that in turn is transmitted to a sensitive photodetector through the fiber optic. Such dosimeters can be scintillation dosimeters (organic) or radioluminescent dosimeters. Typical works on fiber dosimeters use polyvinyl toluene (PVT) based scintillators and scintillating optical fibers. Other fiber dosimeters employ aluminum oxide doped with rare-earth elements, presenting RL and OSL signals. OSL was first suggested as a dosimetry tool in the 1950s−1960s by Antonov-Romanovskii *et al.*, Braunlich *et al.* and Sanborn and Beard [150].

OSL materials also emit prompt RL signal during irradiation. This signal can be

used for dosimetry as the scintillator luminescence emission [151]. RL/OSL optical fiber dosimeters, based on doped SiO_2, Mg_2SiO_4:Tb and Al_2O_3:C have been studied for application in brachytherapy and for photons, electrons and protons in the MV range [152–158]. These materials present relevant temperature dependence [157, 158] and usually there's a need for pre-irradiation for stabilization [159, 160] or annealing to eliminate prior irradiation history. Some works report on thermoluminescence properties of doped SiO_2 for LDR and HDR brachytherapy [161–163], although not suitable for real-time and *in-vivo* dosimetry.

Fiber optic dosimeters with organic scintillators are the most promising devices for *in-vivo* and real-time dosimetry and have been extensively explored over the last decades. The most significant works on fiber optic dosimeters are listed in Table 4.3.

Up to the date, the Exradin W1, from Standard Imaging, is the only optical fiber based dosimeter available in the market, making a mark in a 25 year research period on the subject. The Exradin W1 scintillator is near-water equivalent thus minimizing beam perturbation and artifacts in imaging devices. The device is based on organic scintillators. Studies on pre-commercial and commercial versions have been reported [164–170]. The device consists of a scintillating optical fiber (SOF) (1 mm diammeter by 3 mm long, outer diammeter 2.8 mm) coupled to a PMMA optical fiber with a 2.2 mm diameter jacket. The light is measured by a RGB photodiode (MCSiAT, Mazet, Germany) [164] and the green and blue channels are connected to a SuperMAX dual-channel electrometer (Standard Imaging). The detector nominal response is 60 pc/Gy.

Up to this date, the main challenges regarding *in-situ* dosimetry with fiber optic dosimeters in prostate brachytherapy are the probe volume, temperature dependence [141–143, 255–257], position information, large range of dose and dose rate [127] and the noise generated in the optical fiber cable (*stem effect*) [217, 142]. In addition, brachytherapy dose distributions present high gradient [127] so uncertainties in the detector position may generate substantial dose uncertainties [258]. In the following section, causes for *stem effect* and the techniques to overcome this issue will be presented.

4.4.2 *Stem effect* in fiber optic dosimeters

The *stem effect* in a fiber optic dosimeter has two major contributions: Cherenkov radiation and the fluorescence and phosphorescence generated in the fiber by electron excitation [134, 221, 255, 258]. Fluorescence may occur in the light guide due to the intrinsic scintillation properties of the material constituting the optical fiber [154]. In addition, defects in the matrix, which act as electron traps, can originate phosphorescence [155], which is caused by charge trapping and detrapping phenomena.

The fluorescent light emission is isotropic, while the Cerenkov effect is characterized by anisotropic emission [171].

Cherenkov radiation is the light emitted when a charged particle, such as a beta-particle,

Table 4.3: Studies on fiber optic radiation detectors for medical application.

Reference	Detection principle	Sensitive material	Optical fiber	Photosensor	Cherenkov removal	Energy range	In-vivo Real-time
Akselrod et al [150]	OSL/RL	Al_2O_3:C	SiO_2	PMT	Subtraction	IMRT 6 MV $23-35$ kV X-rays	****
Alhabdan et al [171]	Organic scintillator	EJ-200 ø3 mm	SiO_2, PMMA	Si-photodiode	Optical filtration	6 MV X-rays	****
Andersen *et al* [172]	OSL/RL	Al_2O_3:C	PMMA (GH2001-P)	ME03 luminescence readers	Delayed readout	LINAC 6 and 18 MV photons	****
Andersen *et al* [173]	OSL/RL	Al_2O_3:C	PMMA (GH2001-P) ø0.5 mm	ME03 luminescence readers	Delayed readout	HDR-brachytherapy	*****
Archambault *et al* [174, 175]	SFO	BCF-12, BCF-60	POF	CCD	background subtraction optical filtration chromatic removal	IMRT, 6 MV	*****
Archambault and Klein *et al* [100, 176]	SFO	SCSF-3HF	POF ϕ 0.5 mm	CCD	Chromatic removal	Proton beams, 6 MV	*****
Arnfield *et al* [177]	Plastic scintillator	BC-408	SiO_2	PMT	Background subtraction	HDR-brachytherapy	*****
Aznar *et al* [178]	OSL/RL	Al_2O_3:C	PMMA (SK-40)	PMT	Delayed readout	(6, 18) MV photons	****
Bartesaghi *et al* [179, 180]	SFO	BCF-10, BCF-12	PS	PMT	Subtraction	electrons (6-20 MeV) photons (6, 18 MV)	****
Beddar *et al* [146, 134, 181–186]	Organic scintillator	BC-400	SiO_2 Multi-core	PMT (R1635)	Subtraction	MV range, photons electrons, protons	*****
Beierholm *et al* [166, 187–190]	SFO	BCF-60	PMMA (GH-4001)	PMT (H5784)	Chromatic removal	6 MV X-rays, 6-15 MV photons	*****
Benoit *et al* [191–193]	OSL/RL	SrS:Ce,Sm 3 mm	SiO_2 ϕ 0.6 mm	PMT (H5784)		$6-18$ MV, $9-12$ M3V 24 GeV/c protons	*****
Boivin *et al* [194]	SOF	BCF-60 ϕ 1 mm	PMMA (GH-4001)	PMT, Pin photodiode	Subtraction	$120-220$ kVp, (6, 23) MV photons	******
Buranurak *et al* [143]	SFO	BCF-12 and BCF-60	PMMA (GH2001-P)	PMT (MP982)	REVER	electrons (6-20 MeV) photons (6, 18 MV)	****
de Boer *et al*[195]	Plastic scintillator	BC-400	SiO_2	PMT	Chromatic removal	125 kVp X-rays, 20 MeV electrons	*****
Carrara et al [157, 158]	RL	Ce^{3+} doped SiO_2	SiO_2	PMT (R7400P)	Background subtraction	HDR-brachytherapy (urethral)	*****
Carwright et al [196]	Plastic scintillator	BC-400	PMMA	CCD	negligible	192Ir HDR-brachytherapy	*****
Chen [197]	Plastic scintillator	BC-430(red), EJ-260(green)	PMMA ø1 mm	Photodiode (BPW21)	Optical filtration	6 MV	****
Clift *et al* [198–200]	Plastic scintillator	BC-444G, BC-428, BC-430	PS ø5 mm	Photodiode	Temporal gating	16 MeV	*****
Correia *et al* [201]	SFO	BCF-60 ø1 mm	PMMA	SiPM	Subtraction	^{192}Ir HDR-brachytherapy	****
Chiodini *et al* [153, 154]	RL	Ce^{3+} doped SiO_2	SiO_2 ø200 μm	PMT (R7400 P)	Background subtraction	20 kV X-rays, 6 MeV, 6 MV 38, 138 MeV protons	*****
Dilcher *et al* [202]	RL	Cu^{1+} doped SiO_2	SiO_2 ø400 μm	PMT		^{192}Ir, ^{90}Sr/Y, ^{32}P	*****
Dusseau *et al* [203]	OSL	MgS	SiO_2 ø600 μm	PMT			****
Fernandez *et al* [204]	Inorganic scintillator	CsI(TI)	PMMA ø1 mm	PMT		^{60}Co	****
Frelin *et al* [205]	SFO	BCF-60 ø1 mm	PMMA	CCD	Optical filtration	$8-15$ MV, $8-21$ MeV	*****
Fontbonne *et al* [206]	SFO	BCF-60	Photodiode MAZeT	Photodiode	Optical filtration	$6-24$ MV X-rays	*****
Gaza *et al* [151]	OSL	Al_2O_3:C ø500 μm	SiO_2 (FT-600-UMT)	PMT (P10PC)		6 MV	*****
Guillot *et al* [207]	SFO	BCF-60	POF	CCD	Optical filtration	6 MV, ^{90}Sr	*****
Ishikawa *et al* [208, 209]	Plastic scintillator	BC490	PMMA (MH4001)	PMT (H7155)	Optical filtration	^{192}Ir	*****
Ismail *et al* [210]	RL	GaN	ø350 μm		n.a. below threshold	^{125}I, $90-150$ kVp X-rays	*****
Jang *et al* [211]	SFO	BCF-60 ø1 mm	POF	CCD (SDZ-160)	Wavelength discrimination	LINAC 6 MV, 6 MeV	*****
Jang *et al* [212]	SFO	BCF-12	PMMA (SH2001)	PMT	Background subtraction	^{60}Co	*****
Huston and Justus *et al* [213–216]	OSL	Cu^{1+} quartz	SiO_2 ø400 μm	PMT (HC-124-03)	Gated	6 MV X-rays	*****
Kertzscher *et al* [217, 218]	OSL/RL	Al_2O_3:C	PMMA ø1 mm	PMT (MP-983)	Background subtraction	^{192}Ir PDR/HDR-brachytherapy	*****
Konnoff *et al* [219]	SFO	BCF-12	PMMA (GH4001)	SiPM	Air-core	6, 18 MV	*****
Lambert *et al* [220, 221]	Plastic scintillator	BC-400 ø1 mm	PMMA	PMT		^{192}Ir HDR-brachytherapy	*****
Lambert *et al* [222–224]	Plastic scintillator	BC-400 ø1 mm	PMMA	PMT	Air core	(6, 18MV) photons (6, 20) MeV electrons	*****
Lee *et al* [225]	Plastic scintillator	BC-400 ø1 mm	PMMA	PMT (H3164–10)	Air core + shutter	6 MV photon beam	*****
Lee *et al* [128, 226–228]	SFO	BCF-12 ø1 mm	PMMA (SH-4001)	Si photodiode (S1336–18 BK)	Background subtraction	^{192}Ir HDR-brachytherapy	*****
Lee *et al* [141]	SFO	BCF-12 ø1 mm	PMMA (GH-4001)	SiPM (S10362-11-100U)	n.a.	$50-150$ kVp X-rays	*****
Molina *et al* [229, 159]	RL	Mg_2SiO_4:Tb	PMMA	PMT (H9319)	Background subtraction	$^{Co}60$	*****

(continues on next page)

(continuation from previous page)

Reference	Detection principle	Sensitive material	Optical fiber	Photosensor	Cherenkov removal	Energy range	In-vivo Real-time
Mattia *et al* [230, 231]	RL	Yb^{3+} doped SiO_2	SiO_2 ø200 μm	InGaAs APD	Optical filtering	6 MV photons	*••••
Moutinho *et al* [232–234]	SFO	BCF-12	PMMA	SiPM	n.a. (below threshold)	LDR-brachytherapy X-rays $15-50$ kVp	****•
Nascimento *et al* [235, 236]	OSL, RL	Al_2O_3:C	PMMA (GH4001)	PMT (P30USB)	Optical filtration	(6, 16) MeV electrons (6, 15) MV photons Carbon beam 290 meV/n	*••••
Naseri *et al* [237]	Organic scintillator	BC-400	PMMA ø1 mm	PMT (H3164-10)	Air-core	IMRT, LINAC 6 MV	*••••
Peralta and Rego [139]	Organic scintillator SOF	RP-200A ø3 mm BC-404 ø3 mm BCF-10 ø2 mm BCF-60 ϕ 2 mm	PMMA ø2 mm	PMT (R647P)	n.a. (below threshold)	X-rays $25-100$ kVp	*••••
Pittet *et al* [238]	RL	GaN	SiO_2	PMT (H7260M-04)	Subtraction	LINAC 6 MV and 18 MV X-rays	**•••
Rego *et al* [239]	SOF	BCF-60, ø2 mm	PMMA	Photodiode (S9195)		X-rays, $30-50$ kV	*••••
Rego *et al* [240]	SOF	BCF-10, ø2 mm	PS (BCF-98)	Photodiode (S9195)		HDR-brachytherapy	*••••
Santos *et al* [241]	RL/OSL	BeO, ø1 mm	SiO_2	OSL, PMT (H7360-01)		LINAC, 6 MV X-rays	*••••
Stefanowicz *et al* [242]	SFO	BCF-12, BCF-60	PMMA	PMT (MP-982)		MR-LINAC	*••••
Suchowerska *et al* [243, 244]	Plastic scintillator	BC-400 ø1 mm	PMMA	PMT	Background subtraction	^{192}Ir HDR-brachytherapy	***••
Tanyi *et al* [245, 246]		Cu^{1+} doped quartz,ø4 μm	SiO_2	PMT	Gated extra fiber for trigger	EBRT, $6-20$ MV	•••••
Therriault-Proulx *et al* [74]	SOF	multi-point SOF (BCF-10/12/60) ø0.6 mm	PMMA (GH-4001)	CCD	Chromatic removal	X-ray 125 kVp LINAC 6MV photons	**•••
Therriault-Proulx *et al* [164, 247]	Scintillating fiber	BCF-60 ø1 mm	PMMA (GH-4001)	RGB photodiode	Chromatic removal	HDR-brachytherapy	*••••
Mattia *et al* [231]	RL	Yb^{3+} doped SiO_2, ø200 μm		SiPM / Si-APD	Optical filtration	LINAC 6 MV, 20 kV X-rays	*••••
Mones *et al* [152]	RL	Ce^{3+} doped SiO_2, ø200 μm		PMT (R7400 P)		^{60}Co, 6 MV LINAC	*••••
Veronese *et al* [155]	Phosphorescence / RL	Ce^{3+} doped SiO_2	SiO_2	PMT (EMI 9125QB)		X-ray (32 keV) LINAC (6 MV photons, 6 MeV electrons)	*••••
Veronese *et al* [156]	Phosphorescence / RL	Eu doped SiO_2		CCD		X-ray (20 kV) LINAC (12 MeV electrons)	*••••
Wang *et al* [248]	RL	GaN	SiO_2 ø0.6 mm	SiPM (MPPC C11208)		HDR-brachytherapy	**•••
Watanabe *et al* [249]	OSL	$BaFBr:Eu^{2+}$		PMT	Chromatic removal	X-rays (65 keV), ^{60}Co	*••••
Williamson *et al* [133]	Plastic scintillator	BC400	PMMA	PMT	Chromatic removal	X-rays, ^{192}Ir	*••••
Wootton [250]	Scintillating fiber	BCF-12, BCF-60	PMMA	CCD	Chromatic removal	EBRT (^{60}Co) IMRT for prostate cancer Proton beams	***••
Yoo *et al* [251]	Scintillating fiber	BCF-10 ø1.5 mm	POF (SH-6001)	PMT (H5784)	n.a. (below threshold)	Entrance surface dose $50-120$ X-rays	*••••
Yoo *et al* [252]	Scintillating fiber	BCF-12 , ø0.5 mm	POF (SH-2001)	PMT (R7600U-03-M4)	Subtraction	LINAC, EBT	•••••
Yoo *et al* [253]	Scintillating fiber	BCF-12, ø1 mm	POF (GH-4001)	SiPM (MPPC S10362-11-100U)	n.a. (below threshold)	Entrance surface dose $75-150$ kVp X-rays	***••
Yoo *et al* [254]	OSL	LYSO:Ce	POF, ø3 mm	PMT	not considered	Gamma-Ray Spectroscopy	•••••
Yukihara *et al* [160]	OSL	Al_2O_3:C	PMMA	PMT	Chromatic removal	IBT dosimetry, ^{60}Co	*••••

crosses a dielectric medium with velocity higher than the velocity of light propagation in that medium:

$$\beta n > 1 \tag{4.13}$$

where n is the refractive index of the medium and β is the ratio of the velocity of the particle in the medium to that of light in vacuum [109]. The particle generates a cone of light spreading out at the Cherenkov angle κ

$$\kappa = \arccos\left(\frac{1}{\beta}\right) \tag{4.14}$$

which projection gives the ellipse or ring of the ring-imaging Cherenkov (RICH) detectors. The Cherenkov radiation contribution to the *stem effect* depends on the type of the radiation and on the volume of the dosimeter in the radiation field. For photon beams, the Cherenkov background might be negligible but not for electron beams [146, 134]. Considering Eq. 4.13, the energy threshold (E_{th}) for Cherenkov radiation production in a given material depends on the refractive index (n) of that material:

$$E_{th} = m_0c^2\left(1 - \sqrt{1 + \frac{1}{n^2 - 1}}\right) \tag{4.15}$$

where the m_0c^2 corresponds to the electron rest-mass energy of 511 keV.

The Cherenkov emission spectrum covers the entire visible domain and the energy threshold of production depends on the refractive index of the medium and on the type of charged particles. For electrons, this threshold energy is 178 keV in PMMA and 144 keV in PS [207], typical materials used in plastic optical fibers.

The emissions of the most common radioactive sources used in LDR prostate brachytherapy (^{125}I, ^{103}Pd, ^{131}Cs) present an average energy of about ∼30 keV, i.e. below the energy threshold for Cherenkov radiation production in common plastics such as PMMA or PS used in optical fibers. However, in the case of HDR prostate brachytherapy, the photon energy spectrum for ^{192}Ir is between 0.136 and 1.06 MeV with an average energy of 380 keV, which is above Cherenkov radiation production threshold for PMMA or PS. For this reason, dosimeters using plastic optical fiber cables should take into account the Cherenkov radiation contribution to *stem effect*. Cherenkov radiation is mainly produced by Compton electrons. The Cherenkov light emission occurs during the time required for the electron to slow down, reaching an energy value below the threshold energy, so Cherenkov light emission decay time is usually in the order of picoseconds in solids. The number of photons emitted per electron in common Cherenkov media is only several hundred per MeV [109]. The yield of Cherenkov photons per unit of wavelength (λ) is proportional to $1/\lambda^2$ [109]. The spectral distribution of Cherenkov radiation is broad, covering the entire visible range but it is stronger in the blue region (400-480 nm) where typical plastic scintillators emit their light. Since the magnitude of the Cherenkov radiation emitted depends on the optical fiber extension being irradiated, optical fiber cross section and its numerical aperture [259], Cherenkov radiation is particularly

relevant in external beam dosimetry [146, 260] and both primary radiation beam and stray radiation present in the treatment room contribute to the *stem effect* [255].

4.4.3 Techniques for *stem effect* removal

The two main contributions to *stem effect*, the radioluminescence of the material and Cherenkov radiation, are both related to the material properties and the *stem effect* intensity is related to the portion of the cable being irradiated. Several studies have proposed different solutions to overcome this issue. The main options are based on the subtraction of the background signal, timing differences between scintillation and Cherenkov radiation and chromatic removal (Figure 4.4).

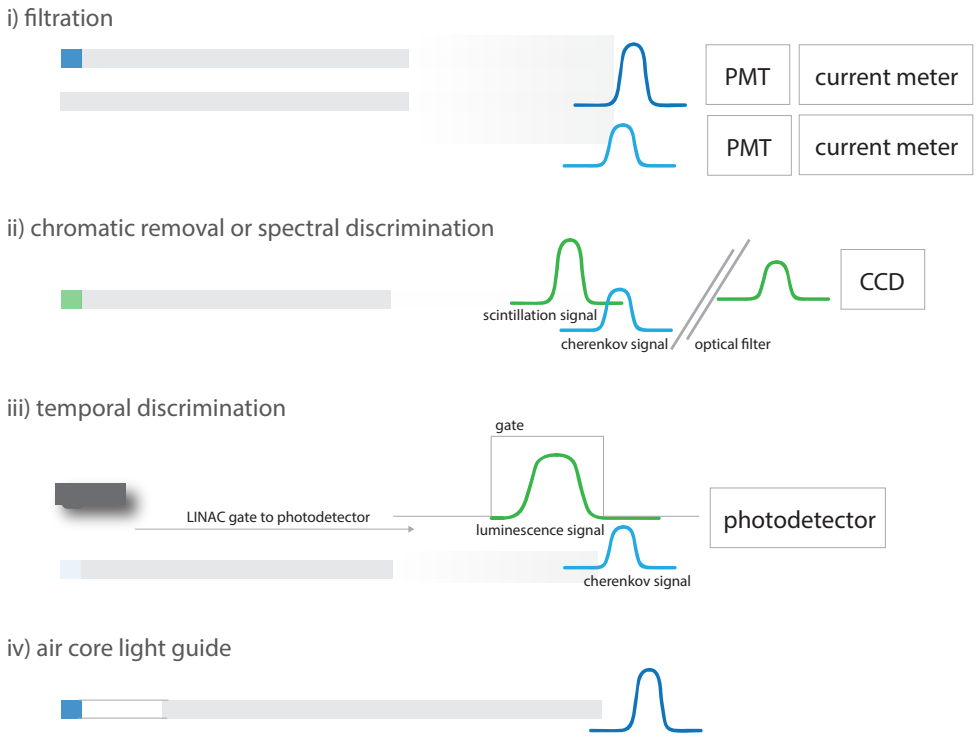

Figure 4.4: Techniques for Cherenkov radiation removal.

i) background removal

A simple solution for background removal was initially proposed by Beddar *et al.* [146, 186], consisting on the use of a second optical fiber but without the scintillator. This would allow to quantify the amount of *stem effect* generated in the light-guide fiber. In this solution the current signal generated in the dummy fiber, containing no scintillator, is subtracted to the signal of the fiber with the scintillator. The main inconvenience of this

technique is the limitation for high gradient dose fields due to the very small size of the radioactive sources used in HDR brachytherapy [128] and the doubling of the probe volume due the the addition of a second dummy fiber.

ii) chromatic removal or spectral discrimination

Optical filtration and chromatic analysis have been proposed by de Boer *et al.* [195], in 1993. If the scintillation light has an emission wavelength out of the Cherenkov radiation range, it is possible to remove the *stem effect* contribution by filtration using dichroic mirrors. However, there are some technical difficulties regarding this technique since typical organic scintillators have emission in the blue region.

Guillot *et al.* [207] evaluated the spectral method in situations where the Cherenkov light is dominant over the scintillation light, with 6 MV photon beam from a medical linac. The authors found that the accuracy of the spectral method depends on the procedure used to determine the calibration factors of the plastic scintillator dosimeter and on the attenuation properties of the optical fiber used. They reported that the spectral method can correct the Cherenkov light effect with an accuracy level of 1%.

iii) temporal discrimination

Temporal discrimination is based on the temporal discrepancies between RL signal in Al_2O_3:C crystal and the produced Cherenkov. The Cherenkov emission is prompt emission, in the picoseconds range and the fluorescence is in the nanoseconds range. Both are very short-lived when compared with the RL signal that is a delayed process [158]. A temporal filtration based method has been proposed by Clift *et al.* [198–200] for pulsed mega-voltage electron and photon beams that are commonly used in radiotherapy treatment. The dosimeter comprises the scintillator long decay time constant (264 ns) BC-444G (Saint-Gobain) coupled to a polystyrene core optical fiber. However, this method is only applicable in pulsed radiation sources where the trailing edge of the incident pulse is shorter than the decay time of the scintillator used. Clift *et al.* [200] concluded that the temporal method of minimizing the *stem effect* (Cherenkov and fluorescence) is more efficient than optical filtration methods.

Similar approach was proposed by Andersen *et al.* [261]. This method is based on gated counting in connection with pulsed linear accelerator radiation beams.

iv) air core light guide

Lambert *et al.* [223, 224], Suchowerska *et al.* [243, 244] and Liu *et al.* [259] developed a Cherenkov-free scintillation dosimeter with an air core light guide for external beam radiotherapy. The setup comprises a BC400 (Saint-Gobain) scintillator coupled to a silvered air core light guide with 200 mm length. The air core is connected to a PMMA optical fiber. A second fiber with the same length is used to subtract the *stem effect* produced in the PMMA waveguide. Both PMMA fibers are outside the primary radiation field. Although Cherenkov radiation production is highly suppressed since it is not generated in the air core due to

refractive index of the air (close to that of vacuum), the remaining PMMA optical guide may suffer from stray radiation. The dosimeter was evaluated in 6 MV and 18 MV photon beams and 6 MeV and 20 MeV electron beams, in both static and dynamic fields. The depth dose measurements for the photon beams agreed with ionization chamber measurements to within 1.6%, except in the build-up region due to positional uncertainty. For the 6 MeV and 20 MeV electron beams, the percentage depth dose measurements agreed with the ionization chamber measurements to within 3.6% and 4.5%, respectively. For field sizes of 1×1 cm^2 and greater, the air core dosimeter readings agreed with diamond detector readings to within 1.2%.

v) other techniques

In a similar approach to the temporal discrimination, Lee *et al* [225] developed a solution which adds shutter mechanisms to block the signals quantifying the residual background signal. The shutter is placed outside the primary beam and is connected to a 20 m, 1 mm core PMMA optical fiber coupled to a Hamamatsu H3164–10 photomultiplier unit located outside the radiation room. The background signal is subtracted from the total measurement acquired in a subsequent irradiation, enabling the luminescence signal to be extracted. The tested LCD shutter version presented large uncertainty (±2.4%) and the mechanical shutter version was in close agreement (±0.29%) with output factors measured with an ionization chamber.

4.5 Development of the brachytherapy dosimeter prototype

4.5.1 The dosimeter concept

Currently, prostate brachytherapy procedures are performed without proper quality assurance and quality control [262]. The presented studies and results of this work envisage the development of a dosimeter prototype for both LDR and HDR prostate brachytherapy. Although these treatments present some similarities, when referring to *in-vivo* dosimetry, different challenges arise mainly concerning the automation of HDR afterloaders whereas LDR procedures require manual loading of the radioactive seeds. Besides these operational difficulties, technical challenges regarding *stem effect* removal are a major concern in HDR brachytherapy. It is intended that the dosimeter can be inserted into the human body throw standard catheters or typical brachytherapy needles of gauge 17 (nominal inner diameter of 1.067 mm) and perform in-situ real-time dosimetry (Figure 4.5). In addition, complementary probes can be used and inserted with urinary catheters into the urethra. Besides providing a tool for both quality assurance and control, dosimetric data will be acquired in real-time which in turn will allow performing real-time dose correction and treatment adjustments.

The dosimeter comprehends two main parts, a disposable probe and the photodetector and readout electronics (Figure 4.6). A low cost disposable probe is an attractive feature

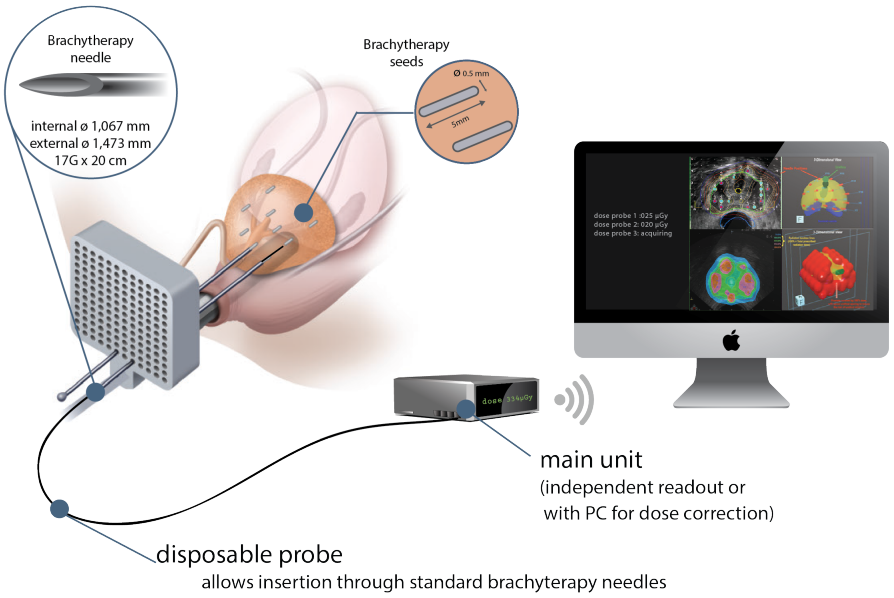

Figure 4.5: Concept of the prostate LDR-brachytherapy dosimeter.

for this type of device, as it is intended for insertion into the human body, avoiding time consuming sterilization procedures and storage logistics. The disposable probe consists of a radiation sensitive tip made with a scintillating optical fiber which is optically attached to a clear PMMA core plastic optical fiber for scintillation light guidance into the photodetector. SiO_2 optical fibers are known for lower attenuation (up to 10 times lower at 650 nm), however plastic optical fibers present some advantages over the SiO_2 fibers, namely higher numerical aperture and higher acceptance angle thus allowing higher light collection from the scintillators and minimum bending radius [171]. Notwithstanding,the lower density and larger numerical aperture and acceptance angle of the PMMA fibers make them more prone to be affected by Cherenkov radiation when compared to the SiO_2 fibers.

Two versions were developed, with 0.5 mm and 1.0 mm PMMA waveguides, as depicted in Figure 4.7. A standard ionization chamber, a MOSFET based dosimeter (typically used for dose assessment in the rectum in prostate brachytherapy) and a brachytherapy needle gauge 17 (ga17) are also included for size comparison. The dosimeter is intended for application in both LDR and HDR brachytherapy. Considering the low-light level of scintillation light produced in LDR regimes, a high-gain photodetector and low noise electronics are required. The SiPMs were the natural choice for photodetector due to their versatility, small size, robustness and lower cost when compared with the standard photomultiplier tubes.

The developed system allows simultaneous current and pulse mode operation (based on the same electronics previously described in Section 3.3) and in Appendices A and B. In the following sections, works related to the dosimeter probe and initial tests in clinical environment are presented. Up to this date no solution for *stem effect* removal

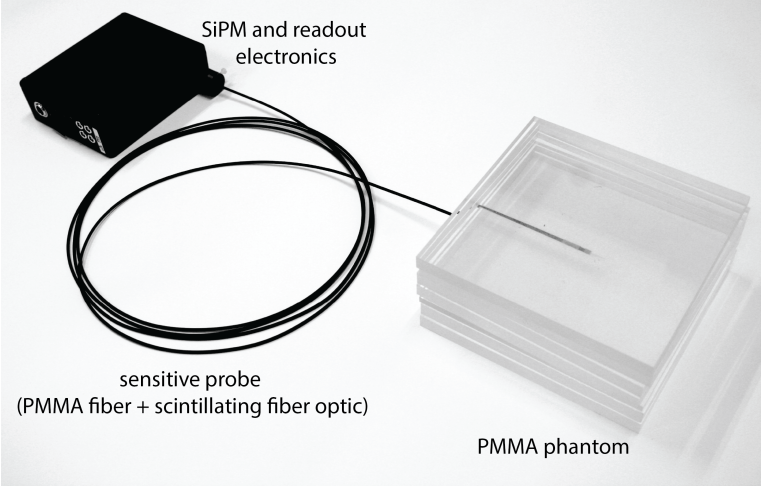

Figure 4.6: Prototype of the dosimeter showing the optical fiber probe placed in a PMMA phantom.

Figure 4.7: Prototype of the dosimeter probes with 0.5 mm and 1.0 mm diameter showing the relatively small size in comparison with an ionization chamber, a MOSFET dosimeter and a brachytherapy needle gauge 17.

was implemented and initial studies were performed to assess the magnitude of this effect in the plastic optical fibers.

4.5.2 Sensitive probe development

Temperature dependence

The response of scintillating optical fibers and clear optical fibers was evaluated in the $20 - 40$ °C temperature range. Several optical fibers 9 cm long (Table 4.4), hand-polished on both sides, were inserted into a copper rod and placed inside a light tight aluminum enclosure. The fibers under evaluation were coupled to two optical fibers, one for blue light input from a *light emitting diode* (LED) and the other one for light output, connected to a

Table 4.4: Measured optical fibers light loss for the BCF-12, BCF-91A, Avago HFBR-R/EXXYYYZ and ESKA HMCKU-1000PW optical fibers.

Optical fiber	Core material	Light loss (%/°C)	other studies (%/°C)
Saint-Gobain BCF-12	PS	−0.01	-0.13 (light generated) [142] -0.15[143] -0.263 [141]
Saint-Gobain BCF-91A	PS	-0.50 – 0.55	
Avago (HFBR-R/EXXYYYZ)	PMMA	-0.01 – 0.04	
Multi-core (HMCKU-1000PW)	PMMA	0.19 – 0.20	

SiPM biased and read by a picoammeter (Keithley 6487). The temperature was monitored with two digital temperature sensors (DS18B20, Maxim Integrated) and controlled by a Peltier cell with a PID system composed by a micro-controller (Arduino Mega) and a motor shield (Adafruit) (Figure 4.8). Both SiPM and LED temperature were monitored and kept constant. Four fibers were evaluated, a BCF-12 (Saint-Gobain) scintillating optical fiber, a BCF91-A (Saint-Gobain) WLS fiber, a clear optical fiber (Avago) and a multicore POF (HMCKU-1000PW, 19 cores, from Asahi Kasei, Japan). Measurements were performed by increasing the temperature from 20 up to 40 °C and decreasing the temperature from 40 down to 20 °C. Results are depicted in Figure 4.9 and summarized in Table 4.4.

The Avago (HFBR-R/EXXYYYZ) PMMA optical fiber has low temperature coefficient for blue light. Similar results had been reported elsewhere [141]. The multicore fiber (HMCKU-1000PW) presented a high temperature coefficient in the conditions of this study. The core and clad materials are PMMA and fluorinated polymer, respectively. The observed high temperature coefficient might be related to separation between cores due to thermal expansion with the temperature increase.

The scintillating optical fiber (BCF-12, Saint-Gobain) and the clear optical fiber (PMMA core, Avago) showed little dependence on temperature, of about -0.01%/°C and -0.01 – 0.04%/°, respectively. The BCF91-A WLS fiber presented a -0.50 – 0.55%/°C variation in the amount of transmitted light. This value is similar to temperature dependence

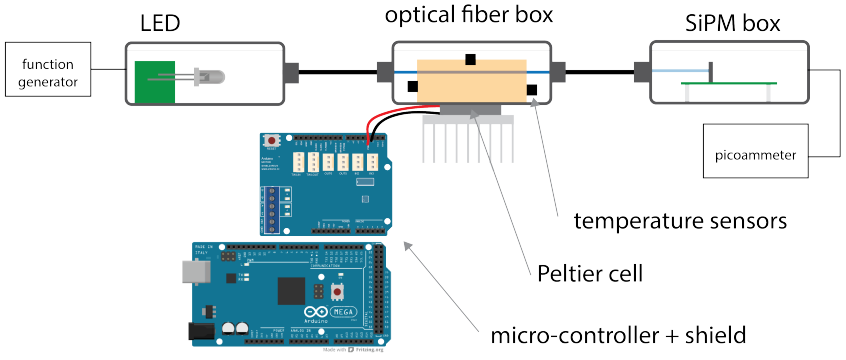

Figure 4.8: Experimental apparatus for the study of scintillating fiber optics temperature dependence.

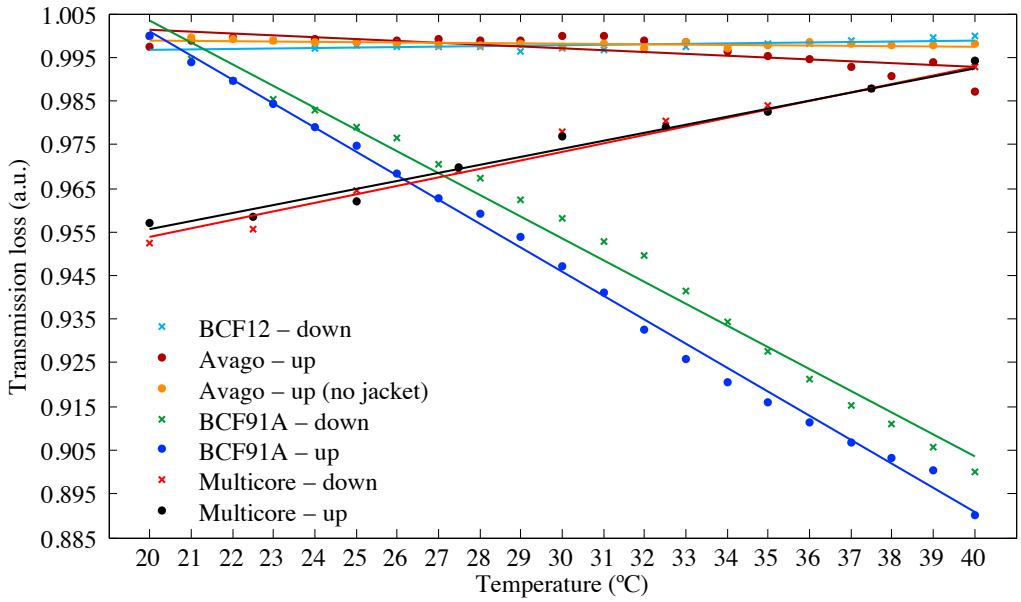

Figure 4.9: Fiber optics dependence on temperature.

observed by Wootton and Beddar [142] for the BCF-60 green scintillating optical fibers (Saint-Gobain). The author's [142] examined the temperature dependence of the BCF-60 and BCF-12 scintillating fiber (both from Saint-Gobain) and two reference optical fibers without the scintillator. The variation on the intensity and spectral distribution of light was quantified with a spectrometer. The authors verified that the total intensity of the light generated by the BCF-60 and the BCF-12A decreased by 0.32% and 0.13% per °C, respectively. By measuring the temperature dependence of the scintillating fibers with blue light from a LED we are assuring that the possible temperature dependence is a property of the plastic solvent and not of the fluor. In addition, this study allows the assessment of the possible contribution of the optical fiber light guide to the dosimeter temperature dependence. Studies on temperature dependence of organic scintillators (or RL dosimeters with Al_2O_3:C) from Andersen *et al.* [256], Lee *et al.* [141] and Wootton and Beddar [142] evaluate the temperature dependence of the dosimetric probe, accounting for the contribution of the optical fiber guide. The majority of these studies immerse the sensitive tip of the dosimeter in a beaker with water that is heated gradually and the dosimeter is irradiated with X-rays or with a linear accelerator in the MeV range. Buranurak *et al.* [143] evaluated the temperature dependence of four scintillating fibers (BCF-12 and BCF-60 from Saint-Gobain and 81-0083 and 81-0087 from Industrial Fiber Optics, 2 mm long and coupled to a 10 m long GH2001-P ESKA PMMA optical fiber) by placing the dosimeter probe directly on top of the thermo electric cooler plate. The fibers were tested in the $15 - 40$ °C range with a 50 kV X-ray source. In a second test, a 10 cm long BCF-60 scintillating fiber was coupled to a PMMA fiber cable to ensure that only the scintillating fiber was exposed to the X-ray beam. The authors used four different band pass filters and verified that the temperature

effect depends on the emission wavelength. For the emission peak of the scintillators, the authors reported a temperature coefficient of -0.15 ± 0.01 %/K for the BCF-12 and -0.55 ± 0.04 %/k for the BCF-60 fiber and concluded that the optical fiber cable didn't present temperature dependence.

The BCF-91A wavelength shifting fiber revealed a larger dependency with temperature, in comparison with the BCF-12 blue scintillating optical fiber. Both fibers core is made of PS, in BCF-12 a fluor shifts the ultraviolet light to blue and in BCF-91A a second fluor shifts this blue light into green light. The emission spectrum of the BCF-91A is similar to the BCF-20 green scintillating optical fiber [263] and both present similar temperature dependence. The probable cause is due to the fluor responsible for the blue to green shift. Because the setup used in this study does not excite the BCF-12, we're not able to evaluate the contribution of the first fluor to the possible temperature dependence of the fiber. This can be the reason for the different results obtained in comparison with other works. Also this is in agreement with the results from Lee *et al.*[141], attributing the temperature influence to the scintillation kinetics. New studies will be performed using a UV-LED or radioactive source.

Irradiation of the optical fiber cable in a Linac with ^{60}Co photons

The BCF-12 emission is in the $400 - 600$ nm range (Figure 3.22), with a peak emission at 435 nm. It is known that the Cherenkov emission wavelength range is broad and in the blue region. To verify if there is a superposition of the scintillating light with the *stem effect*, the optical fiber cable was irradiated with ^{60}Co photons in a LINAC. A 25 m long spool of optical fiber was placed in a 20×20 field and a source to surface distance of 20 cm. The irradiation rate was set to the maximum value of 900 MU/min. A spectrometer USB-4000 from Ocean Optics was used. The resulting spectrum is presented in Figure 4.10.

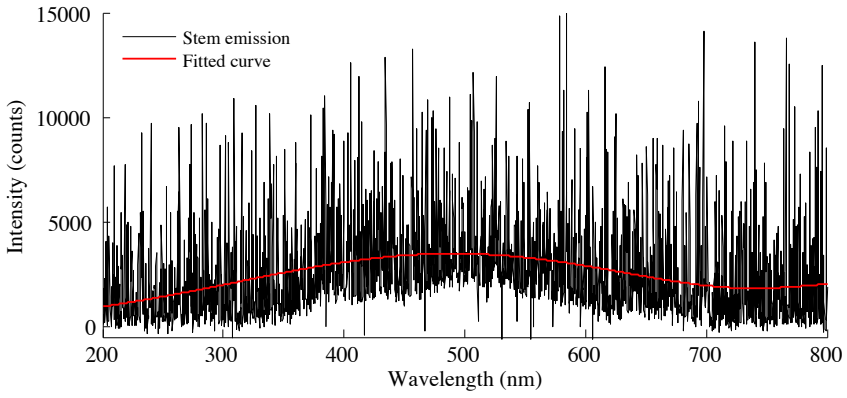

Figure 4.10: Wavelength range of the *stem effect* light produced in the optical fiber cable when irradiated by ^{60}Co photons in a LINAC.

The wavelength range of the *stem effect* light produced is wide and in the $300 - 700$ nm range with an apparent peak at ∼500 nm. This is in agreement with other studies

[136, 217, 74, 257, 264, 265]. However one should note that the length of the optical fiber is enough due to the different attenuation (dB/km) with λ. Typically a step-index POF presents lower attenuation at green, yellow and red wavelengths. Nowotny *et al.* [266] reported the lower *stem effect* of the PMMA fibers in comparison to PS or silica fibers, although it is not negligible once the *stem effect* emission spectrum overlaps the emission of the BCF-12 scintillating optical fiber. Further studies on the *stem effect* contribution to the total signal are presented in Section 4.5.4.

Dosimeter response under low energy X-ray beam

The dosimeter response when irradiated with a low energy X-ray beam was evaluated using a 0.5 mm diameter probe (5 mm long BCF-12 scintillating fiber and 3 m long DC-500 PMMA optical fiber). This probe allows insertion into standard stainless steel brachytherapy needles, gauge 17 (17ga) (see Figure 4.7). The brachytherapy needle was placed inside a PMMA phantom, at 3.5 cm depth, as schematized in Figure 4.11. The X-ray tube used was an Oxford Instruments series 5000, 50 kVp and 1 mA max, with a 125 μm Be window and a 25° cone angle. The dosimeter probe was inserted into the brachytherapy needle. The fiber optic probe was shielded from ambient light. Measurements were performed in the $15 - 50$ kVp range, by varying the X-ray tube current in the $0.1 - 1.0$ mA range. The same measurements were repeated by removing the brachytherapy needle and placing the dosimeter probe in the same configuration in the PMMA phantom. Results are plotted in Figure 4.12. The dosimeter response is 30 times lower when placed inside the brachytherapy needle, for the 50 kVp X-ray beam. At lower tube voltages of 40 and 30 kVp, the dosimeter response when placed inside the brachytherapy needle is almost 50 and 100 times lower, respectively. For the lower energy X-ray tube voltages of 15 and 20 kVp, the beam is fully filtered.

The brachytherapy needles (17ga) have a nominal thickness of 0.203 mm. At 15 and 50 kVp, the X-ray mass attenuation coefficients (μ/ρ) for the titanium are 35.87 and 1.213 cm.g^{-2} and for iron 57.08 and 1.958 cm.g^{-2} [144], respectively. Attenuation ranging from 96% to 10.5% is expected for 15 kVp and 50 kVp X-rays, for a titanium target with 0.203

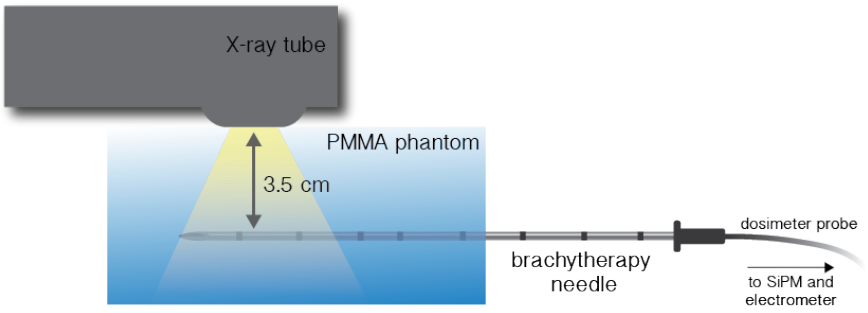

Figure 4.11: Illustration of the experimental setup for the study of the dosimeter response under low energy X-ray beam with and without brachytherapy needle.

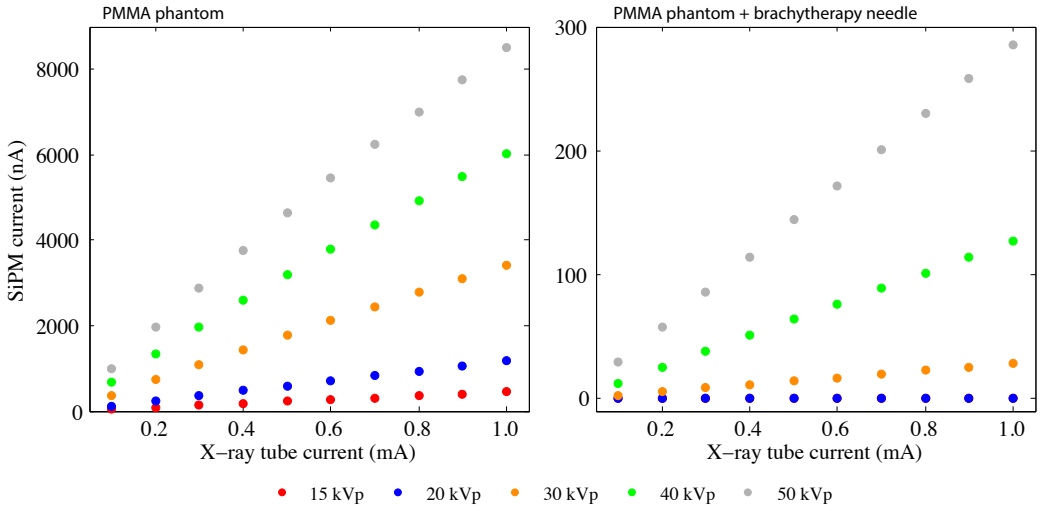

Figure 4.12: Dosimeter response for $15-50$ kVp X-rays in PMMA phantom (left) and inserted in a stainless steel brachytherapy needle (right).

mm length. For a iron target of 0.203 mm, the attenuation is in the $99.98-26.86\%$ range for the $15-50$ kVp energy range. This fact must be taken into consideration regarding applications such as LDR brachytherapy, where the average isotope decay energy is 30 keV and the brachytherapy needles are made of stainless steel or titanium. The X-ray beam attenuation due to the stainless steel brachytherapy neddle is depicted in Figure 4.13.

For a 15, 20 and and 30 kVp X-ray beam, the beam attenuation is above 99%. Although, for a 50 kVp X-ray beam an average attenuation of 96.8% was observed, whereas a $\sim$27% was estimated. This is mainly justified by the strong component of low energy X-rays even at 50 kVp voltage. To verify this, the X-ray tube spectrum was acquired placing aluminum filters in front of the X-ray tube window. An Amptek XR-100SDD silicon thermo-electrically

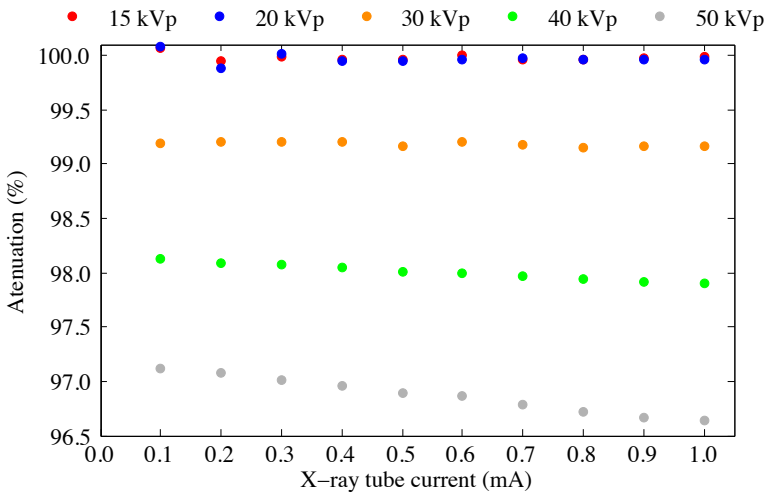

Figure 4.13: Variation of the dosimeter response for $15-50$ kVp with X-ray beam hardening due to filtration resulting from the brachytherapy needle.

cooled solid-state silicon drift detector with Be window was used. This detector doesn't allow to obtain the X-ray spectrum at energies above ∼30 kVp, for that a CdZ detector would be required. The X-ray spectra without Al filter and for 0.5, 1.0 and 1.5 mm Al filters are plotted in Figure 4.14, showing a strong attenuation of low energy X-rays, justifying the results presented in Figure 4.13.

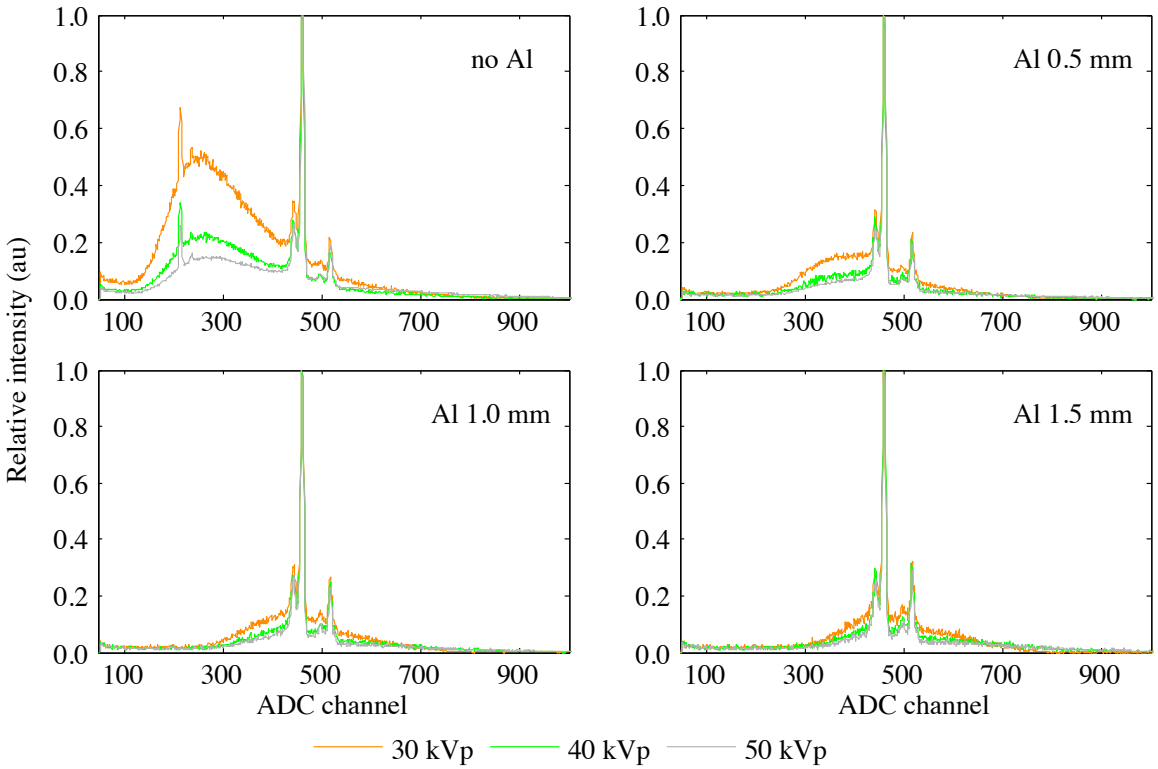

Figure 4.14: X-ray emission spectrum with and without Al filters of different thickness for $30 - 50$ kVp tube voltage.

4.5.3 Dosimeter calibration

An initial evaluation of the dosimeter response to low energy X-rays was performed. The X-ray tube used was an Oxford Instruments series 5000, 50 kVp and 1 mA max, with a 125 μm Be window and a 25° cone angle. The measurements were taken for 30, 40 and 50 kVp with 0.5, 1.0 and 1.5 mm Al filters for X-ray beam hardening.

The measurement of the dose rate was performed using an ionization chamber (RaySafe Xi Transparent). The ionization chamber was placed in a PMMA phantom, at 10 mm depth and in line with the X-ray window at 10 cm distance (Figure 4.15). The measurements were repeated for phantom depths of 10 to 30 mm, in 5 mm intervals and during the measurements the X-ray tube voltage was kept constant, while the current varied from 0.05 to 1.0 mA. The measurements were repeated by replacing the ionization chamber with the optical fiber dosimeter. The fiber optic dosimeter probe consisted of a 5 mm BCF-12 (Saint-Gobain) scintillating optical fiber, coupled to a 3 m long PMMA 1 mm diameter core optical fiber.

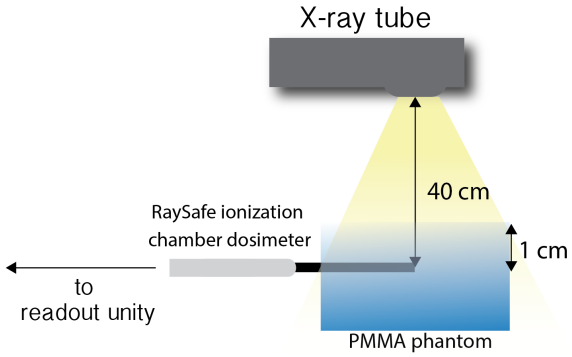

Figure 4.15: Illustration of the experimental setup for the dosimeter calibration to low energy X-ray beams.

The light was read by a Hamamatsu S10362-11-100U MPPC. The MPPC was biased at 73.5 V and read using a Keithley 6487 picoammeter. The SiPM temperature was kept constant at 21°C with a peltier cell. The dosimeter response is presented in Figures 4.16 and 4.17 related to the dose rate measured with the ionization chamber.

From Figure 4.16, one observes a linear response of the dosimeter for all the energies and dose rates. When there is no aluminum filter for beam hardening, for X-rays at higher tube voltages it is observable a strong attenuation. For a 50 kVp tube voltage, a 72% beam absorption was observed for a PMMA depth variation of 20 mm. For a PMMA depth in the range $10 - 30$ mm, the estimated attenuation ranges from 22.40% up to 53.29% [144]. The data obtained with the fiber optic dosimeter are in agreement with the data obtained with the ionization chamber, corresponding to a dose rate variation of 7.1 cGy/s to 2.0 cGy/s (Figure 4.18), translating into a 72% absorption also measured with the ionization chamber. When a 1.5 mm Al filter is used for beam hardening, the observed attenuation due to the PMMA ($10 - 30$ mm) was ∼57%. For a 50 keV X-ray beam, the estimated X-ray attenuation due to a 1.5 mm Al filter is ∼14%, while for a 30 keV X-ray beam it is ∼37% [144]. For the same PMMA thickness of 10 mm, for a 50 kVp voltage an attenuation of ∼73% was observed for the ionization chamber while for the fiber optic dosimeter a ∼59% attenuation was observed and for a 30 kVp voltage a ∼81% attenuation was observed with the ionization chamber and ∼72% with the fiber optic dosimeter. The deviation of the experimental data from the expected attenuation are justified by the strong contribution of the low energy X-rays where no filtration is used (Figure 4.14).

Figure 4.17 depicts the dosimeter response in terms of the dose rate, measured with the RaySafe Xi Transparent ionization chamber for the same conditions. The measurements range from dose rates of hundreds nGy/s to hundreds of μGy/s. The ionization chamber is specified for a dose range of 100 nGy/s to 20 mGy/s with an uncertainty of 5% ($60 - 150$ kVp). This ionization chamber has a 7.5 mm diameter while the dosimeter probe has a sensitive volume of 3.9 mm^3, corresponding to a BCF-12 SOF 1 mm diameter, 5 mm length.

From the results, one can observe that the dosimeter dependency with energy is low for

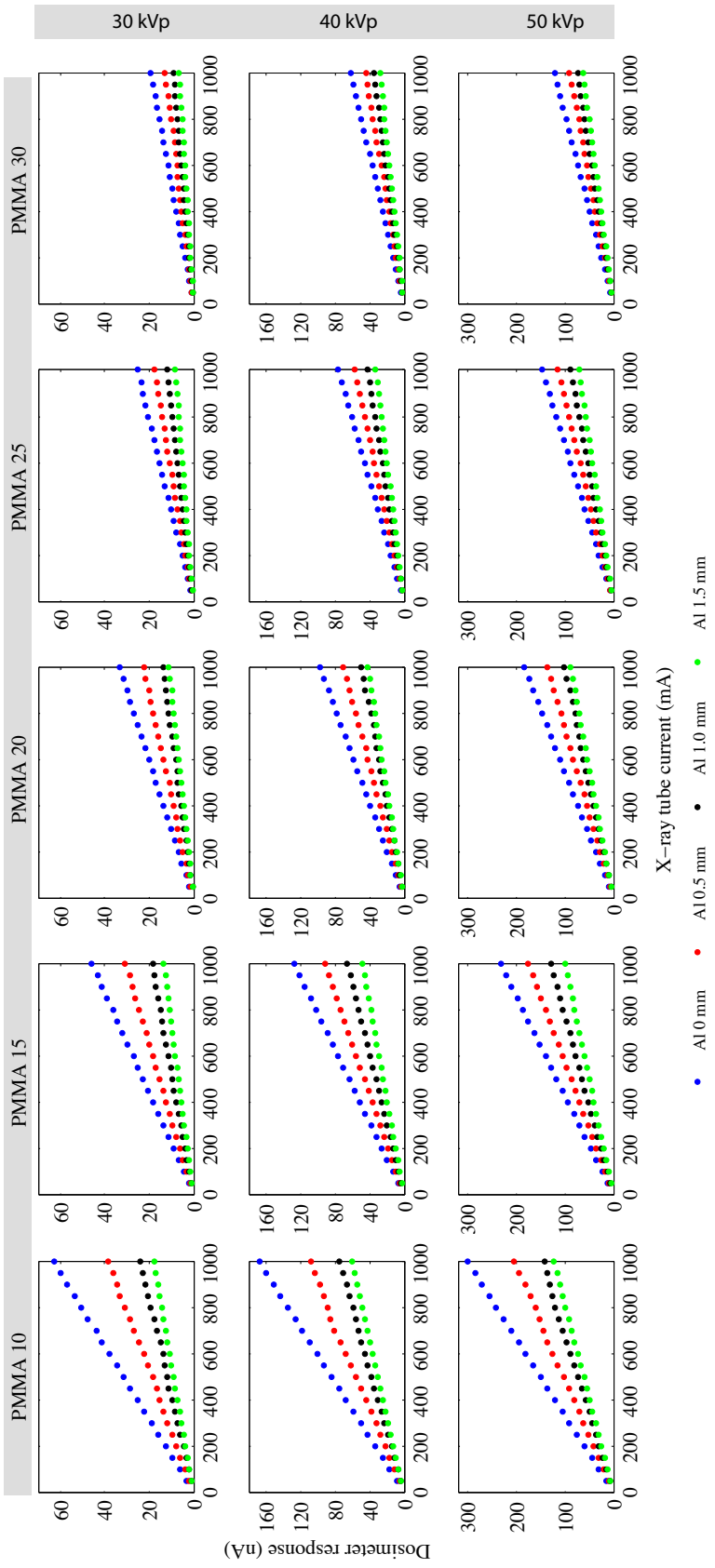

Figure 4.16: Optical fiber dosimeter response to 30 kVp (top), 40 kVp (middle) and 50 kVp (bottom) X-rays.

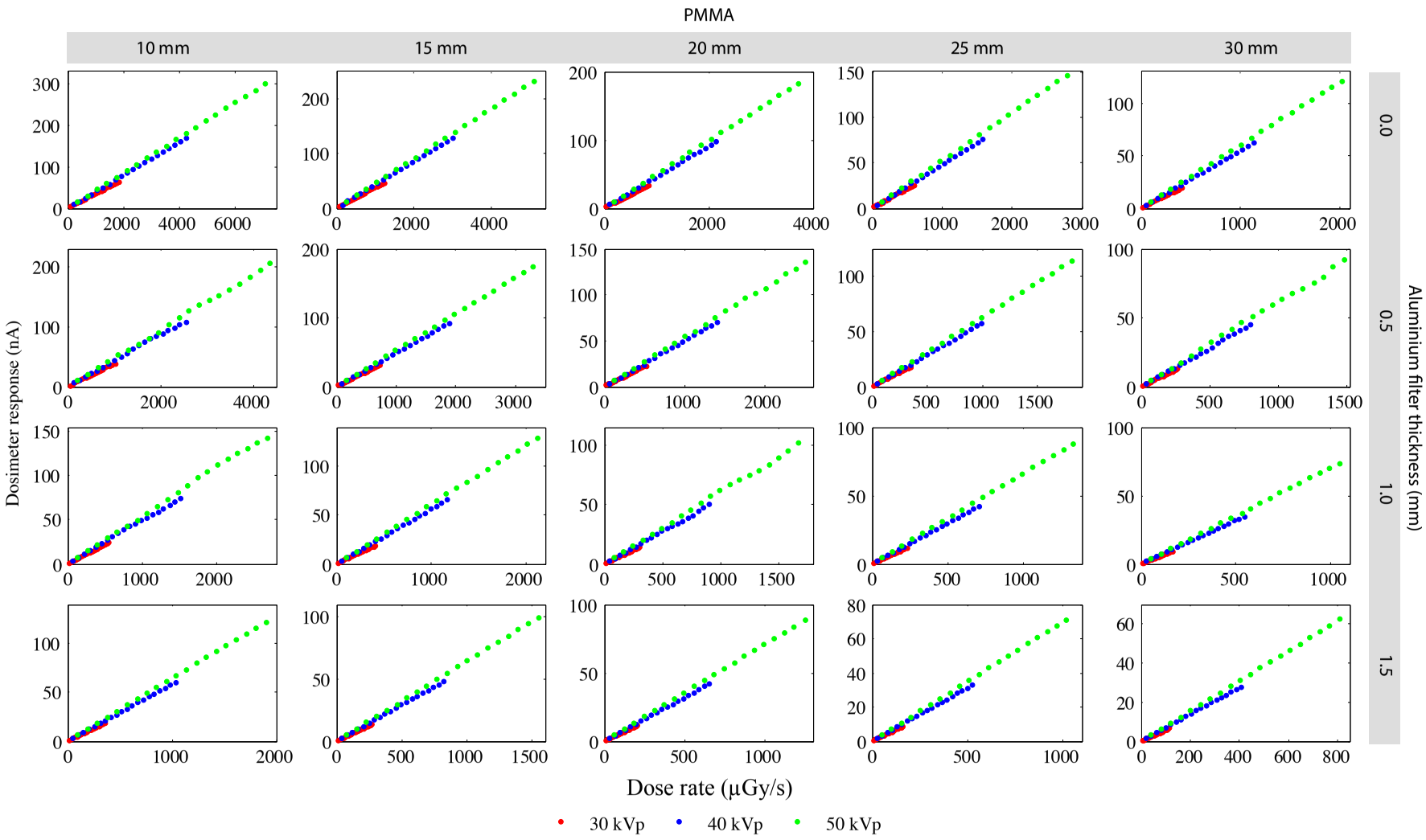

Figure 4.17: Optical fiber dosimeter response as a function of the dose rate measured with an ionization chamber.

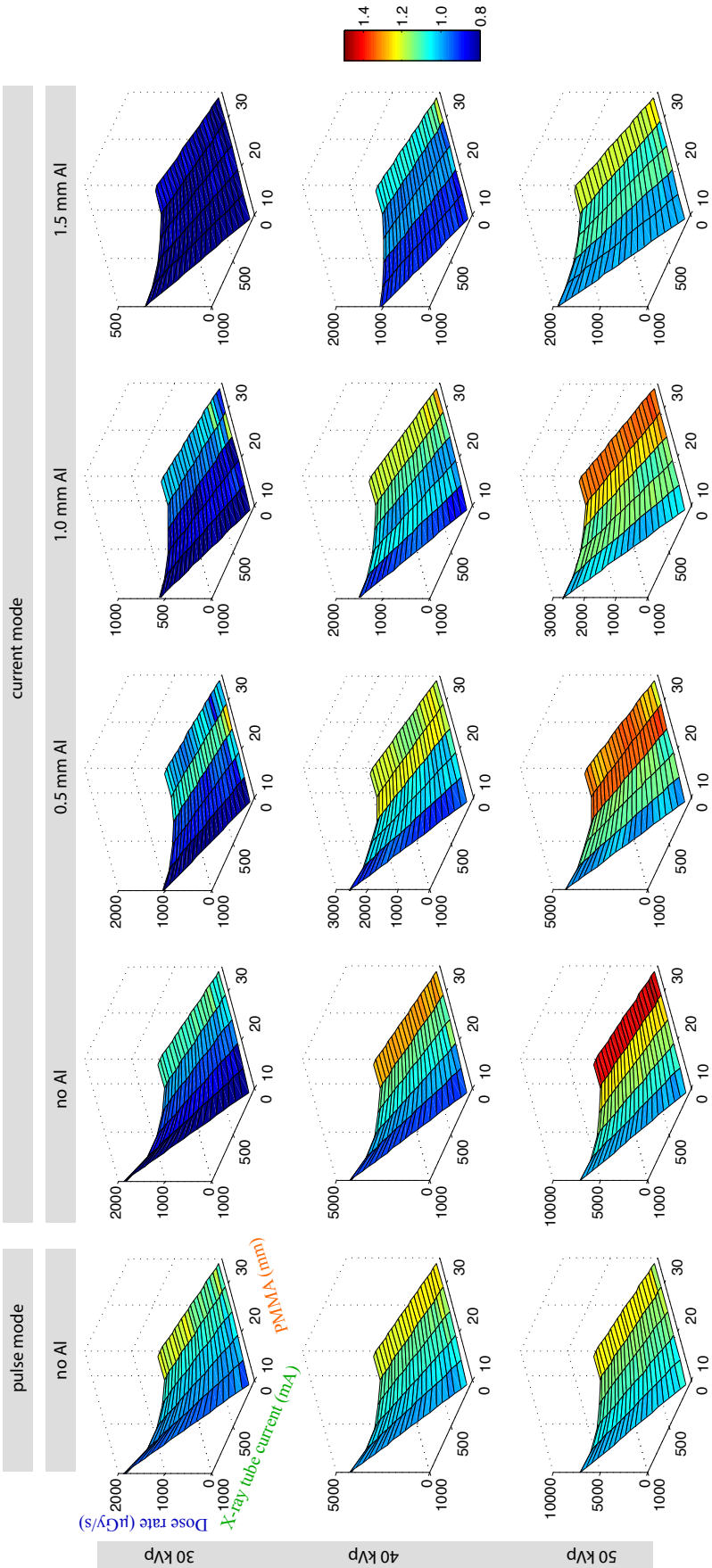

Figure 4.18: Optical fiber dosimeter response relative to the ionization chamber for 30 – 50 kVp X-ray tube.

X-ray beams at tube voltages > 40 kVp at dose rates below 1 μGy/s but it presents some dependency at higher dose rates. This behavior is observable at PMMA depth ranging from 10 to 30 mm and for the different aluminum filtering conditions, so it should not be related to the X-ray beam hardening.

The developed fiber optic dosimeter can be operated in both pulse and current mode. Measurements were repeated for pulse mode readout at 30, 40 and 50 kVp voltages without aluminum filtering. The color map is obtained by dividing the normalized response of the fiber optic dosimeter by the normalized response of the ionization chamber. From the color map of the plots on the left (pulse mode, no Al filter) and the ones on the right (current mode, with additional Al filters) of Figure 4.18 one can observe that the pulse mode readout presents a sensitivity closer to the one of the ionization chamber. This analysis also shows that, for the same PMMA depth, the response of the dosimeter reveals low dependency on the dose rate for both pulse and current operation modes.

For the same filtration conditions, PMMA depth and Al filtering, one can observe that for the $30-50$ kVp voltages (columns) the pulse mode data presents lower variation than the current mode. This is mostly significant at extreme values corresponding to higher PMMA depths and no Al filtration.

Lee *et al.* [141] developed a dosimeter comprehending a 10 mm long, Ø 1.0 mm BCF-12 SOF, coupled to a PMMA optical fiber (GH-4001). The author's evaluated the dosimeter response in count mode in the $25-60$ °C temperature range, for a $50-150$ kVp X-ray tube potential. The dosimeter revealed a non-linear behavior, with the count rate increasing exponentially as the X-ray tube potential increases. The author's compared the optical fiber dosimeter sensitivity to a semiconductor dosimeter, obtaining a linear relation corresponding to a 0.678% increase across the X-ray tube potential. The comparison is not reliable since the semiconductor dosimeter was rated for operation in the $15-35$ °C temperature range and also revealed nonlinear behavior.

Lambert *et al.* [220] evaluated a dosimeter comprehending a organic scintillator (BC-400) coupled to an 1.0 mm Ø core optical fiber for the $50-125$ kVp energy range. The dosimeter showed linear response in the energy range.

Boivin *et al.* [194] evaluated a dosimeter comprehending a SOF, BCF-60 Ø 1.0 mm coupled to a PMMA POF. The calibration was performed in a 120-kVp and 220 kVp orthovoltage unit beam. The authors evaluated several photodetectors, namely PMT, APD and PIN photodiode. The authors compared the signal to noise ratio of the several versions. Although the behavior is linear as the dose rate increases, the presented data reveal high deviations in the PMT and APD readout versions when compared with the commercial Exradin W1 and PIN photodiode.

In comparison with other works related to SOF and plastic dosimeters, the results here presented reveal an improvement in terms of sensibility, linearity and low dependency with energy by operation in pulse mode. This is mainly due to the stability achieved with the developed system.

4.5.4 *In-vitro* studies with ^{192}Ir HDR-Brachytherapy source

The dosimeter response was evaluated under HDR regimes by irradiation with an ^{192}Ir HDR-brachytherapy source from an afterloader (Nucletron, Figure 4.19). The gamma-ray emission from the ^{192}Ir source ranges from 50 to 800 keV with peaks at 316 keV and 468 keV and 380 keV average energy [128, 220].

The studies were performed at the installations of Serviço de Radiologia of CHUC. The afterloader is placed in a treatment room (bunker) and for safety reasons the Afterloader equipment is controlled remotely throw a control room. During brachytherapy treatments only the patient stays inside the treatment room. This required to prepare a remote system to control the dosimeter prototype. A portable PC, used for data acquisition and control of the dosimeter was placed inside the bunker to communicate via a network cable with a second laptop at the control room. The dose measurements were performed with an ionization chamber (PTW 31010 Semiflex Chamber 0.125 cm^3) read by an electrometer (PTW UNIDOS Universal Dosemeter) also controlled remotely.

The dosimeter optical fiber probe was placed in a PMMA phantom on top of a microSelectron (Nucletron) source position check ruler, as depicted in Figure 4.20.

The measurements were repeated for the ionization chamber. The measurements of the dosimeter response were performed using two probe setups of Ø 0.5 mm and Ø 1.0 mm versions, both with 5 mm long BCF-12 scintillating optical fibers of the corresponding diameter. For reference and *stem effect* quantification a passive plastic optical fiber Ø 0.5 mm and with the same length (but without scintillator) was used. Results are plotted in Figure 4.21. Both Ø 0.5 mm and Ø 1.0 mm versions present similar response. The observed difference of these relative to the ionization chamber is mainly due to the higher volume of the ionization chamber.

The *stem effect* is generated from direct irradiation of the waveguide optical fiber but also due to stray radiation. When operated in current mode, a simple approach for *stem*

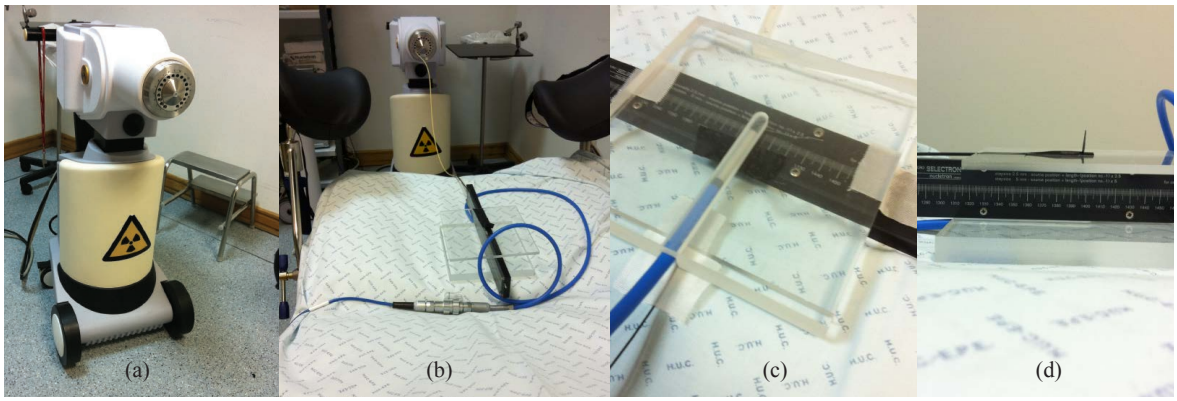

Figure 4.19: (a) Nucletron microSelectron ^{192}Ir afterloader used at CHUC (b) treatment bead with the calibration ruler and ionization chamber (c) detail of the ionization chamber in a PMMA phantom, 15 mm thick (d) detail of the calibration ruler with the SOF dosimeter placed in a PMMA phantom.

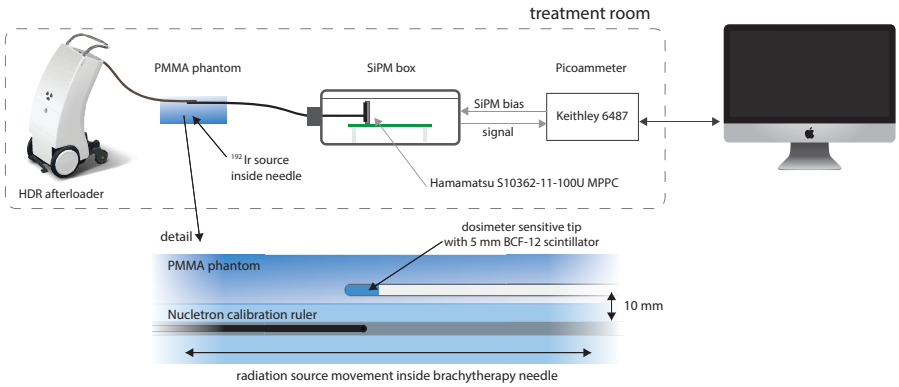

Figure 4.20: Schematics of the setup used for the HDR tests with an afterloader using an ^{192}Ir source.

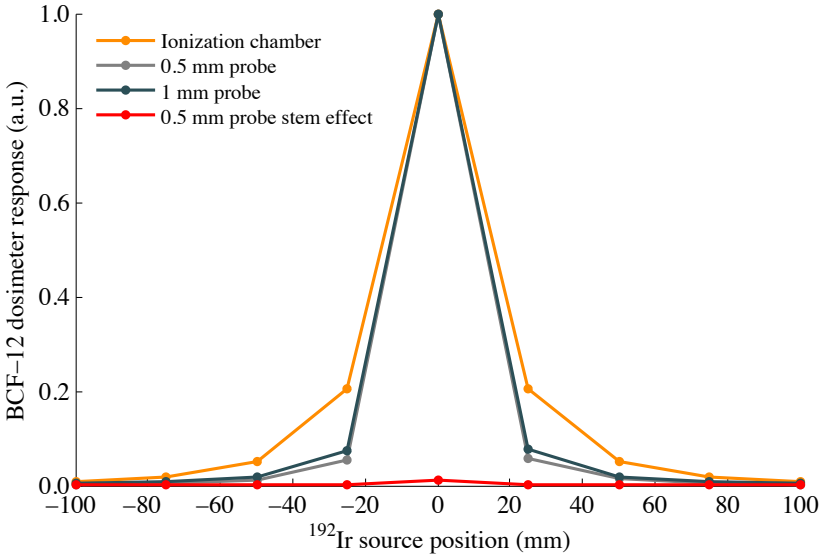

Figure 4.21: Fiber optic dosimeter response when irradiated with ^{192}Ir and comparison with ionization chamber and clear optical fiber for *stem effect* account.

effect removal can be achieved by subtracting the *stem effect* signal. By computing the ratio of the normalized response of the Ø 0.5 mm reference probe (without scintillator) to the Ø 0.5 mm dosimeter probe (with scintillator) one verifies that the *stem effect* contribution is lower than 1.6% when the ^{192}Ir source is at 0.0 mm position. The amount of observable *stem effect* increases up to ∼10% at 3 cm from the ^{192}Ir source and ∼25% at distances above ∼10 cm from the ^{192}Ir source (Figure 4.22). Envisaging the application in dosimetry for prostrate brachtherapy, the dosimeter should comprehend correction for *stem effect* contribution or *stem effect* removal techniques.

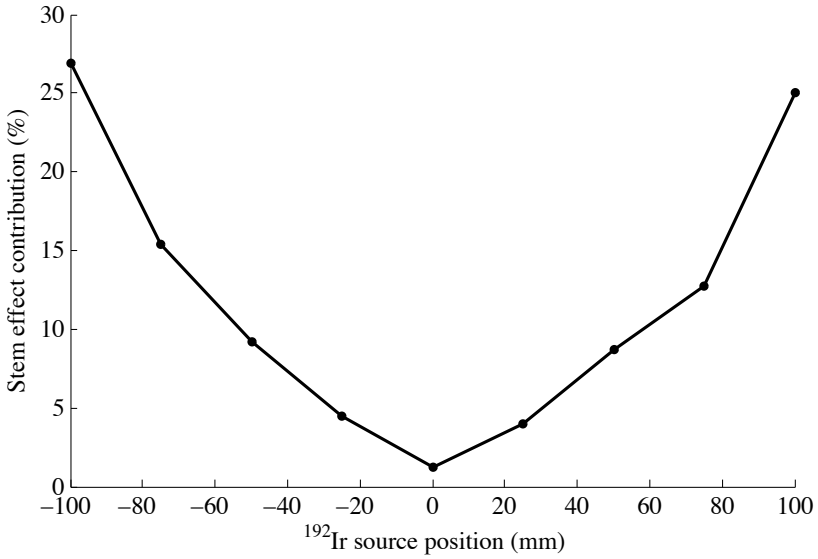

Figure 4.22: *Stem effect* contribution with ^{192}Ir source for Ø 0.5 mm probe.

4.6 Final remarks

The dosimeter shows a linear response with dose and is capable of detecting nGy/s dose rate variations like an ionization chamber. From the calibration of the dosimeter response in a wide dose rate range, nGy/s to μGy/s (Figure 4.17), it was possible to verify that the dosimeter based on scintillating optical fibers allows operation in a wide dose range even at low energies. In addition, the operation in current mode presents lower dependency on the dose rate and on X-ray beam energy. Further studies at higher energies are under planning. It was observed a deviation between the fiber optic dosimeter and the ionization chamber response for the different conditions of PMMA depth and aluminum filtering. Although the dosimeter response is linear, the sensitivity of the fiber optic dosimeter shows not to be the same for all X-ray energies, dose rate and beam hardening.

The results obtained for both studies at low energies, performed by irradiation of the dosimeter probe with X-rays from an X-ray tube operating in the potential range $30-50$ kVp, and at higher energies with an ^{192}Ir source from an afterloader used for HDR-brachytherapy treatments, are in agreement with similar studies with optical fiber dosimeters with organic scintillators [220].

Besides fulfilling all the requirements for *in-vivo* and real-time dosimetry, the high sensitivity of this device makes it a suitable candidate for application in LDR brachytherapy. The first round of studies in the clinical setting allowed to demonstrate that fiber optical based dosimeters are suitable for dosimetry in regimes such the ones in HDR prostate brachytherapy. Although the *stem effect* was minimal, future work should comprehend more studies regarding the *stem effect* in optical fiber cables. The versatility and easiness of use of this kind of device allows application in other radiotherapy modalities such as brachytherapy for macular degeneration and breast cancers.

The studies presented in this chapter follows previous works [76, 267] and have been partially published elsewhere [232–234].

Technology related to the dosimeter has been patented [268] by the University of Aveiro and a *spin-off*, NU-RISE, was created in April 2015. This project has been awarded in several occasions, namely:

- Concurso Nacional de Inovação, Novo Banco, 2015, 30000€
- Building Global Innovators, 5th edition, Medical & Health IT track. Accelerator Program by ISCTE (Lisbon) and MIT (Boston), with Caixa Capital investment of 100000€
- Prove it, Universidade de Aveiro
- Arrisca C, 1000€

Chapter 5

Application case: easyPET

5.1 Motivation

Position Emission Tomography (PET) and *Single-photon Emission Computed Tomography* (SPECT) are the two nuclear imaging techniques with the highest potential for high-resolution molecular imaging. Both techniques allow functional imaging but several features differ between them. PET isotopes emit positrons which produce two 511 keV gamma photons per nuclear decay, thus requiring coincidence detection. PET scanners are usually stationary ring detectors with electronic collimation (best for detection efficiency). PET isotopes are produced in cyclotrons and have short half-life (min - hrs). SPECT isotopes produce a single gamma photon per nuclear decay and have longer half-lives (hrs - days) and can be produced by reactors, generators or cyclotrons. SPECT detectors use physical collimation (poor detection efficiency) and usually have single-head rotating 360° or dual and triple-head systems rotating 180° (or static) and 120°, respectively. A triple-head SPECT scanner is three times faster than a single-head one. Modern SPECT detector-heads have body-contouring orbit allowing to stay closer to the patient body favoring the system position resolution. PET's main applications are in diagnostic nuclear medicine for cancer and brain functional imaging, drug delivery, cardiology, neuroscience and metabolic disorders. As pointed by Schnockel [269] and Phelps [270], small-animal PET would promote the transfer from the *in-vitro* molecular findings to *in-vivo* applications in humans, bridging the gap between basic preclinical and clinical research and the clinical application.

Small size PET systems for small animal imaging have been an active topic of research in the last two decades. Preclinical molecular imaging discoveries in small animals allow a better understanding of human diseases and the development of more effective ways for disease diagnosis and treatment. The transition from the preclinical research into the medical practice has an important role in drug development, noninvasive quantification of 3D

distribution of radio-pharmaceutical administered to a live subject, fundamental molecular processes at cellular level and imaging of gene expression [269, 271]. These systems, generally designated by microPET systems, are intended for small organs, typically 2 to 3 orders of magnitude smaller than the equivalent human structures. For instance, a rat heart is close to 100 times smaller than the human heart. These microPET systems, typically have a ring diameter below 150 mm in comparison with the 800 mm for human PET systems [271]. The smaller gantry of the preclinical PET systems allows better spatial resolution in comparison with clinical PET scanners, 1 - 2 mm for preclinical systems and 4 - 6 mm in clinical PET. This is mainly due to the lower resolution degradation resulting from the non-colinearity of the annihilation γ-rays [272].

Research topics where functional imaging systems are required would benefit from a portable detector with a lower cost than the devices available in the market. Large amount of research on neuronal diseases such as Alzheimer's are conducted with small animals, but current technologies for functional imaging can be expensive.

5.2 Positron Emission Tomography detectors

5.2.1 Principle of operation

In a basic approach, cancer cells reveal a high growth rate and high metabolic rate showing a higher glucose uptake. By linking a positron-emitting radionuclide to a glucose molecule and injecting it into the patient's bloodstream, it is possible to obtain the localization of the cancerous tissues. In these applications, positron emitting radioisotopes are used. Replacement of an atom in a molecule with its radioactive counterpart is known as isotopic labeling [273]. The most common PET radiotracer is the ^{18}F-fluorodeoxyglucose ^{18}F-FDG. The positron emitted from ^{18}F travels a very short distance (on average 200 μm, 2.4 mm maximum range [274]) before losing its kinetic energy. Afterwards, the positron interacts with an electron, suffering an annihilation process with the emission of two 511 keV gamma (γ) photons. These emitted γ-photons are collinear but with opposite directions, being detected by detectors in the same line and almost at the same time. Typically, a PET-scanner has a ring composed by many sensitive cells, allowing the simultaneous detection of these two γ-photons resulting from the annihilation process (Figure 5.1). Only these coincidence events are considered as *lines of response* (LOR). Moving the patient through the detector ring will allow acquiring several 2D slices that later allow a full body 3D image reconstruction.

The limitations of PET arise from the physics of β^+ decay and the detector design, electronics for position determination of the two two γ-photons in coincidence and algorithms for image reconstruction [275].

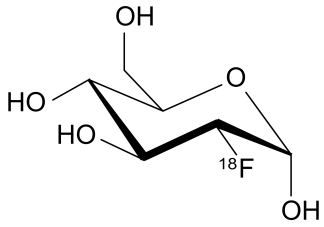

Figure 5.1: ^{18}F-fluorodeoxyglucose radiotracer.

5.2.2 True vs. random coincidences

Due to several factors, the detected coincidence can be a true coincidence, a random event or coincidence due to scattered photons (Figure 5.2).

A scatter coincidence is originated by two gamma photons created in the same annihilation process, however due to scatter of one or the two photons the event is assigned to a wrong LOR (Figure 5.2, center). On the other hand, a random coincidence might be triggered by noise or by two different annihilation processes. This number of accidental coincidences (N_{acc}) can be estimated, considering that:

$$N_{acc} = 2\tau N_1 N_2 \tag{5.1}$$

where N_1 and N_2 are the background rates of each detector and τ is the coincidence time window. Once known the number of random coincidences, a simple correction method is to subtract the number of random coincidences to the total number at each LOR. Further details and discussion on correction of random coincidences can be found in [276, 277].

5.2.3 Spatial and energy resolution

Three major factors limit the spatial resolution in PET scanners: (1) detector intrinsic spatial resolution, (2) positron range, i.e., average distance traveled by the positron before annihilation, and (3) photon acollinearity, i.e., the two photons are not emitted at exactly 180° [275]. Besides the positron range and photon acollinearity, Yao *et al* [271] highlight that

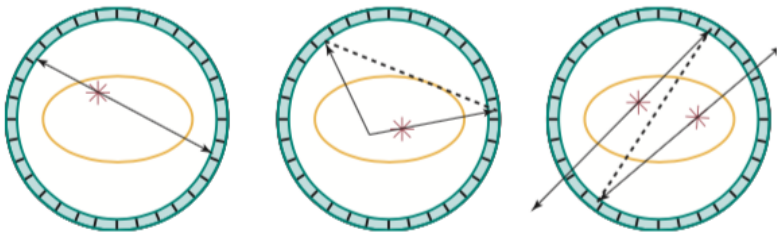

Figure 5.2: True coincidence (left), scatter coincidence (center) and random (accidental) coincidence (right). From [276].

the spatial resolution in small-animal PET scanners is also highly influenced by the size of the scintillator and the detectors decoding scheme. Other factors that limit PET resolution are inter-crystal scattering and inter-crystal penetration.

The spatial resolution can be expressed as the *full-width-at-half-maximum* (FWHM) of the *point spread function* (PSF) after a filtered back-projection [275] in terms of the crystal pitch (d), detector ring diameter (D_R), effective source diameter including positron range (r) and the parallax error (p):

$$FWHM = 1.2\sqrt{\left(\frac{d}{2}\right)^2 + b^2 + (0.0022D_R)^2 + r^2 + p^2} \tag{5.2}$$

where 1.2 is the degradation factor due to tomographical reconstruction. From eq. 5.2, the spatial resolution in PET is intrinsically limited to $0.7 - 0.8$ mm FWHM [275].

5.2.4 Scintillators for PET

Regarding scintillators, the best option for PET applications are high density scintillators with short absorption length for 511 keV photon detection. In commercial PET scanners, typically crystal size is below 20 mm to reduce parallax errors. Knowing that each photon will travel different path lengths, an additional feature of some PET scanners is *time-of-flight* (TOF) detection, by measuring the time of arrival difference between the two photons. This gives further information on the position of the LOR where the annihilation occurred. For these PET scanners, the low decay time of the scintillator is crucial [278]. A system with high efficiency allows the use of radioactive material with lower activity which means that a lower dose is given to the patient. A scintillator suitable for PET scanners should present a high attenuation coefficient for 511 keV photons, should be fast to reduce dead-time effects and discriminate true from random coincidences [276]. In addition, it is desirable that the scintillator emission is in the visible region to match the region of highest PDE of the most common photodetectors (PMTs and SiPMs). Bismuth germanate (BGO), with a decay time of 300 ns, was a common option for PET detectors. Nowadays it is being replaced by faster scintillators such as lutetium oxyorthosilicate (LSO), lutetium-yttrium oxyorthosilicate (LYSO) or gadolinium oxyorthosilicate (GSO) [276].

Table 5.1 shows the main properties of the typical scintillators applied in PET systems. LYSO and BGO are the most common applied in commercial PET scanners. Other typical scintillators are GSO, GSO:Ce, LGSO, LSO, $LaCl_3$, $LaBr_3$ and CWO [279].

5.2.5 Photon attenuation correction

The probability of absorption or scattering of a photon in a given material occurring by photoelectric effect, Compton or pair production, is given by the *linear attenuation coefficient*

Table 5.1: Typical crystals for PET scanners

	% FWHM	Density (g/cm^3)	Relaxation length (cm)	Light yield (photon/MeV)	Decay time (ns)	Emission max. (nm)	Hygroscopic	Radioactive
BGO	12	7.13	1.1	8000	300	480	no	no
LSO:Ce		7.4	1.1	31000	40-47	420	no	yes
LYSO:Ce	20	7.1	1.2	32000	41	420	no	yes
LGSO:Ce	12	7.3	1.18	20000-30000	41	420	no	yes
GSO:Ce/Zr		6.71	1.43	7500	30-60	430	no	no
NaI:Tl	3	3.67	2.9	38000	250	415	yes	no
$LaBr_3$	8	5.29	1.88	65000	15	360	yes	
LuI_3	8	5.6	1.8	47000	30	470	yes	yes

(μ) of that material. From the Beer–Lambert law, the number of transmitted photons (I) is

$$\frac{I}{I_0} = e^{-\mu l} \tag{5.3}$$

where I_0 is the number of incident photons and l is the material depth.

Each coincidence event requires that both photons escape the patient body. The probability of both photons escaping without interaction is the product of the probabilities of each escaping the patient (length, l)

$$e^{-\mu\chi}.e^{-\mu(l-\chi)} = e^{-\mu l} \tag{5.4}$$

where χ and $l - \chi$ are the distances that each photon has to travel to escape [276].

Nowadays PET scanners are usually multimodal systems, integrating X-ray and CT imaging systems for attenuation corrections and to overcome the lack of anatomic information [276]. In these hybrid detectors, the linear attenuation coefficient of each voxel for 511 keV photons is estimated from the linear attenuation coefficient for that voxel obtained by the CT system [276].

5.3 Small size PET systems: state-of-the-art

The major interest of small size PET systems is related to small-animal and preclinical PET/CT imaging systems for oncology, drug discovery, immunology, neurology, bone metabolism and probe development as well as to educational PET systems [269, 280–283]. High-resolution PET imaging of small animals or specific organs require scanners with small sized FOV and small cross-sectional areas of individual scintillator crystals, to enhance spatial resolution, as well as relatively long crystals to enhance detection efficiency and sensitivity. However, if *depth-of-interaction* (DOI) of γ-rays in the crystal is unknown, spatial resolution of small PET scanners rapidly degrades from the center to the edges of the FOV, due to oblique penetration of γ-rays in scintillators. Therefore, determination of DOI, to achieve high spatial resolution and high sensitivity, is one of the most active development topics in PET. Several DOI determination methods have been proposed, which can be divided in two groups: multi-layer (using multiple layers of crystal blocks) and single-layer.

Currently, a strong research topic on PET scanners is related to the integration of PET with other imaging techniques. Options such as ultrasound, CT and Magnetic Resonance Imaging (MRI) allow to gather morphologic information for integration with PET images. Small size PET scanners allow to provide a proof of concept for several techniques seeking integration of imagaging detectors with PET scanners. Some of the most significant works on the subject are presented.

COMPET

The preclinical COMPET, is a PET MRI compatible scanner [284–287]. This detector adds a new concept based on the detection of the *point-of-interaction* (POI) by stacking several layers in a module using WLS fibers perpendicular to the LYSO crystals (Figure 5.3). The COMPET concept consists of four modules of five layers stacked, with 8×8 cm^2 square layers of 30 LYSO crystals (2×3×80 mm^3) interleaved with 24 wavelength shifting fibers (3×1×80 mm^3). The authors [287] reported time and energy resolution around 4 ns and 14% respectively. In MRI compatibility tests, noise counts were observed under radio-frequency (RF) field and gradient field but gating can remove MRI induced noise.

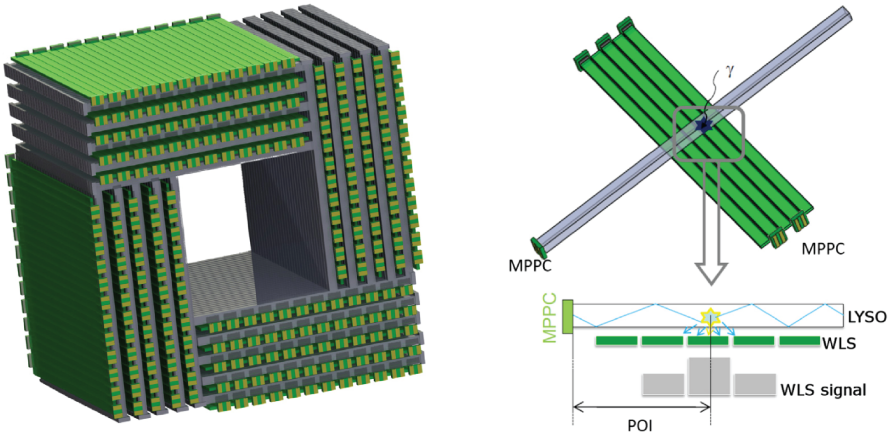

Figure 5.3: Schematic of the Point-of-Interaction concept used in COMPET PET scanner. From [287].

ClearPEM

The ClearPEM [288–300] is a dual-head PET scanner for breast imaging. The Clear-PEM design is intended to achieve low background, minimizing the fraction of random coincidences under a high flux of single photons (up to 10 MHz), high sensitivity and spatial resolution down to 2 mm [289]. The authors reported a 1.3 mm FWHM at the center of the FOV [298] and energy resolution of 16.5% at 511 keV and single photon time *root mean square* (RMS) resolution of 1.3 ns also for 511 keV photons [293]. With an improved LYSO:Ce *compact crystal matrix* (CCM) the inactive area is reduced increasing the single-photon efficiency by 57% [300].

In order to overcome the edge effects of monolithic crystal detectors and poor energy resolution of pixelated crystal detectors, Hwang and Chung *et al* [301] developed a partially

segmented block crystal detector. The detector module uses a LSO block crystal segmented into a 11×11 array read by a 4×4 MPPC array (Hamamatsu S11064) of 3.0×3.0 mm^2. Authors reported a 1.5 mm spatial resolution.

X'tal

The X'tal cube PET system [302–310], is a 146 mm diameter ring comprehending sixteen 18×18×18 cm^3 cubes. The X'tal cubes are laser-processed 3D square grids of 2 mm and 1 mm length. All of the X'tal cube faces are covered with 4×4 SiPMs. The average spatial resolution of the 2-mm X'tal cube was 1.9 mm FWHM over the FOV and 48% improvement for the 1 mm version [302]. An updated version consists of several layers of 2D segmented LYSO scintillator plates (18×18×2.0 mm^3) by laser processing. These are stacked together forming a cube, with SiPM readout in all the six faces of the cube. Updated version is a crystal block with a 9×9×9 array of 2.0×2.0×2.0 mm^3 crystal segments coupled to 4×4 MPPCs at each face of the cube [310]. Authors report a 10% energy resolution for the outer segments as well for the center segment.

AX-PET

The AX-PET [311–315], is a 3D axial PET with long LYSO crystals oriented in its axial arrangement and orthogonally mounted WLS strips for the axial coordinate measurement. The AX-PET demonstrator [314] consists of two modules operating in coincidence, each module comprises 48 LYSO crystals with dimension 3×3×100 mm^3 and 156 WLS strips (3×0.9×40 mm^3 each), arranged in six different layers, with eight crystals and 26 WLS strips per layer. Initial tests with a single LYSO crystal and one WLS strip read by two Phillips digital SiPMs and a ^{22}Na source revealed a 12.3% FWHM. Imaging result from [313] achieved a combined intrinsic axial resolution of 1.21 mm FWHM. In [315] a coincidence time resolution of 211 ps FWHM in the coincidence of two axial modules using digital SiPMs is reported. The coincidence resolving time of 211 ps FWHM is constant over the full FOV and constrains the annihilation point on the LOR to 3.1 cm FWHM.

Educational PET systems

Nowadays there is an increasing interest on basic PET systems envisaging educational purposes. However, little work has been published on this subject and only a few references regarding two different projects were found. An example of such detector is the MiniPET [283], a concept detector composed by two detector heads facing each other, each one comprising 4×4 LYSO crystals and read by 16-channel PMTs (Figure 5.4). The system comprises 3 motors, one for the rotation of the detector cells, a second motor enables the acquisition of data along LORs not crossing the center of rotation and a third motor for the transversal motorized litter movement. The detector allows study of samples up to 20 cm along the axial movement and 350 mm along the transverse plan [283]. Johansson *et al* [282] reported a simple educational PET camera model comprising two pairs of γ-ray detectors,

each pair mounted on a common movable arm and set 10 cm apart. Each pair of detectors can be moved in 10 cm long rails allowing a 10×10 cm^2 area. The detectors use BaF_2 $5\times5\times30$ mm^3 scintillators coupled to 13 mm diameter Hamamatsu R647-01 photomultiplier tubes. Due to the limited translation and rotation movements, the system does not provide imaging capabilities.

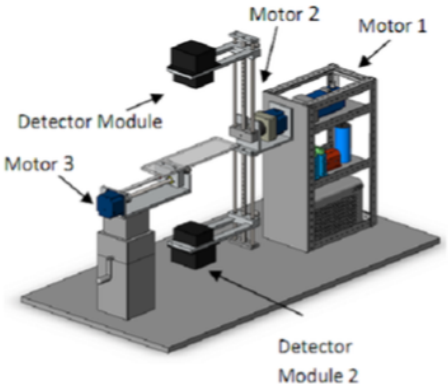

Figure 5.4: Schematic of the MiniPET scanner [283].

5.4 The easyPET

The easyPET[1] concept uses multiple rotational movements to cover the whole FOV. From this idea, a simple and portable PET system for educational purposes can be considered. The easyPET allows the setup of several studies related to traditional PET scanners, namely the component characterization and selection regarding scintillators and photodetectors. Its companion software allows full characterization of the photodetector system (e.g. gain, crosstalk and noise), scintillator (e.g. energy resolution), coincidence detection and PET imaging studies.

In a PET scan, the patient is injected with a radio-tracer such as the ^{18}F-fluorodeoxyglucose (^{18}F-FDG). The radio-tracer will have higher concentration in organs or tissues with higher metabolic rate. The radio-tracer will produce two 511 keV photons resulting from the positron annihilation. In the interaction of the gamma photon with the scintillator, the light produced is proportional to the energy of the γ-photon. To identify a true event, it is necessary to ensure that the two photons detected belong to the same annihilation thus defining an emission line, meaning that they must be detected in a coincidence time interval as small as possible. The functional image is obtained by the detection in coincidence of the two 511 keV photons that are produced simultaneously within the same line but in opposite directions. When these two photons are detected simultaneously a line for the emission (LOR) is defined. The emission of the photons is fully isotropic, so

[1]Patent pending by the Aveiro University, PCT/IB2016/051487

for each point of emission there will be line overlap. This is why PET scanners comprehend a full ring of detectors.

The easyPET is a small PET system simplified to a single pair of detectors oppositely aligned. This is only possible by placing these two sensitive cells in a single structure (U-board) that, in contrast to typical systems, moves around the fixed radioactive source or sample. The system has two rotating axes with two stepper motors executing rotation movements to cover the whole FOV recreating a full ring. The main motor provides full rotation of the U-board (a PCB which comprehends the main components of the detection system). This motor is fixed to a second stepper-motor as represented in Figure 5.5. This second motor allows the scanning movement with a length $d_S/2 \times \theta_2$ at each position of the main motor (Figure 5.5), where d_S is the distance between the two scintillators. Figure 5.6 illustrates the easyPET FOV in three positions for axis-1 (the axis of the main stepper motor) and the scanning movement provided by the second stepper motor. The two scintillators are fully aligned with the center of axis-1.

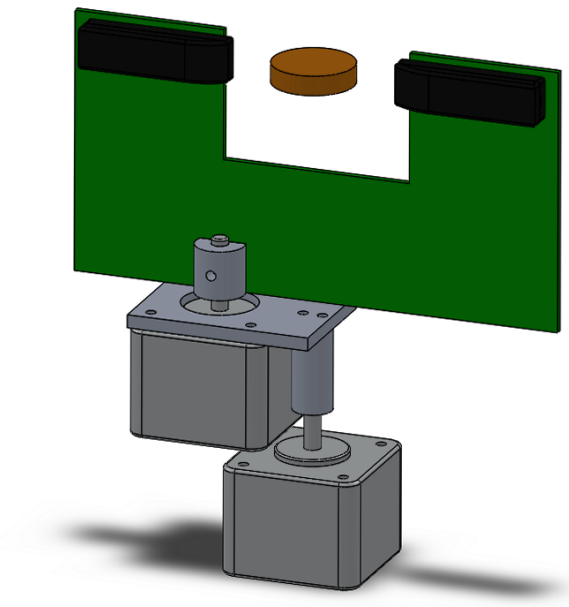

Figure 5.5: Illustration of the easyPET system, comprising a U-board with two sensitive cells and two stepper motors.

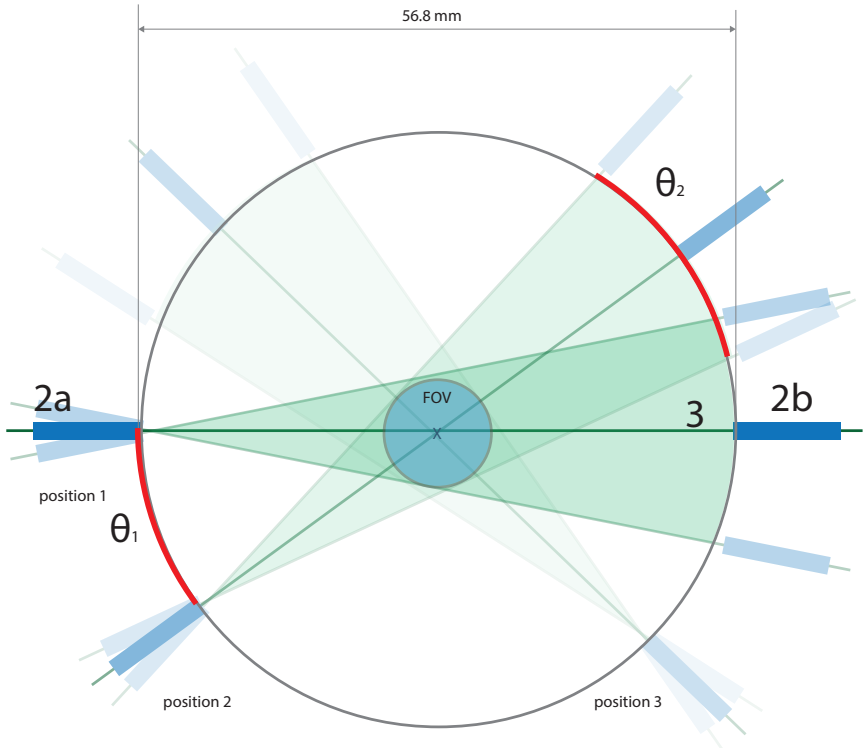

Figure 5.6: Illustration of the easyPET principle of operation with two rotating axes and FOV.

5.4.1 Development of the easyPET detector

PET system with a single pair of cells

The easyPET comprises only two detectors (or cells) (Figure 5.7), aligned and set 56.8 mm apart in the U-board. Each detector is made by a 2×2×30 mm^3 LYSO scintillator and a Hamamatsu MPPC S10362-11-050P silicon photomultiplier with 1 mm^2 active area and 50×50 μm^2 cell area. The SiPM-scintillator optical coupling is done with optical grease (BC-630, Saint-Gobain). For the easyPET system, low cost LYSO crystals (Kingheng, China) were used. The LYSO crystals have an emission peak at 420 nm perfectly matching the MPPC maximum PDE at 425 nm. The detector cells are isolated from ambient light by a light-tight 3D-printed plastic enclosure. This enclosure has also a plug-in connector allowing the use of different cells (e.g. SiPMs with more or less pixels or higher active area SiPMs and scintillators).

The easyPET prototype was developed in the 2013-2015 period and 5 versions of the U-board were developed. The initial U shaped board (U-board) comprised a single pair of detectors (SiPM + LYSO) and the transimpedance amplifier with a second stage for additional gain. Following U-board versions were updated to include all the electronics for SiPM biasing, signal amplification and coincidence event discrimination with the possibility of software adjustment of threshold levels and coincidence window length (Figure 5.8). The board, together with the stepper motors of the system are controlled through an Arduino

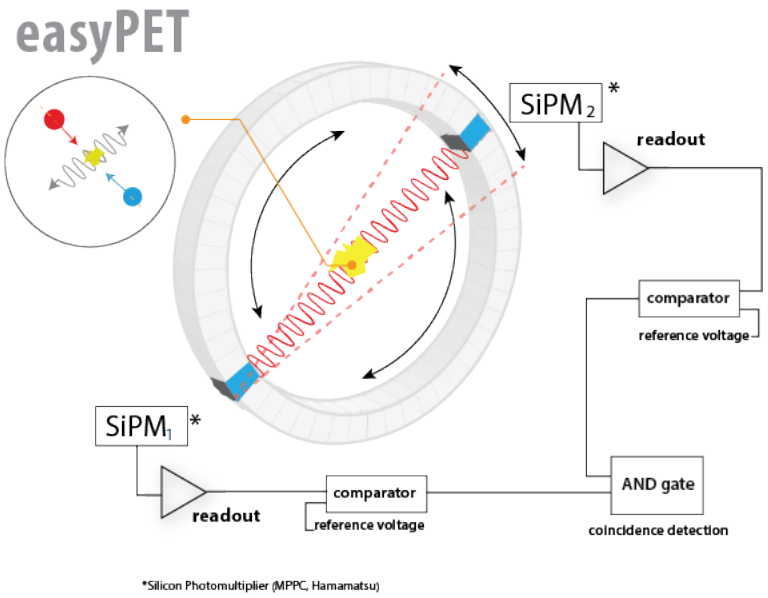

Figure 5.7: Illustration of the easyPET principle of operation with two rotating axes and detection scheme.

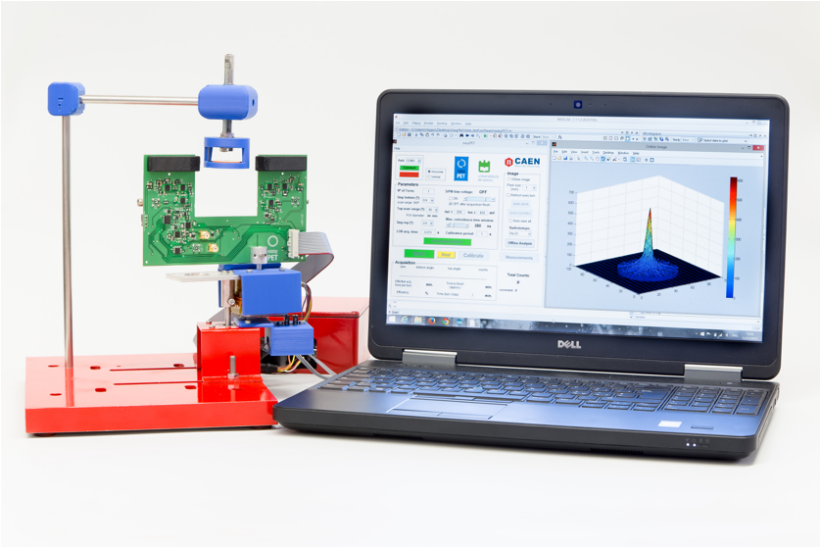

Figure 5.8: The first easyPET prototype from University of Aveiro, University of Insubria and CAEN collaboration.

micro-controller. The main components of the easyPET detector are described in the next sections.

Readout electronics

The easyPET U-board comprehends all the electronics on-board, allowing full analog discrimination of coincidence events (Figure 5.9). The SiPMs are biased with a MAX1932 (Maxim Integrated) 8-bit DC-DC converter. The MAX1932 is controlled through the Arduino micro-controller. The SiPM signal amplification is performed in a 3-stage scheme:

first a transimpedance amplifier, the second stage is a 10 fold gain and the third stage an inverter with unitary gain. The pulse signals from the two channels are fed into a logic section comprising two comparators (MAX9011, Maxim Integrated) and a single 2-input positive AND gate (SN74AUC1G08, Texas Instruments) for coincidence event discrimination (for details, see Appendix C). For each line/position of the system, the total number of events in coincidence is used to trace the 2D image. For counting the number of events in coincidence, the TTL output signal from the AND Gate is digitized by the Arduino micro-controller. In Figure 5.10, a scope screen capture shows the triggered signals by a coincidence TTL signal from the AND Gate output, corresponding to the pulse signal from the two detectors and the respective comparator outputs (bottom) and the amplitude histograms (top) where one can see the ^{22}Na 511 keV photopeak and the respective Compton scattering.

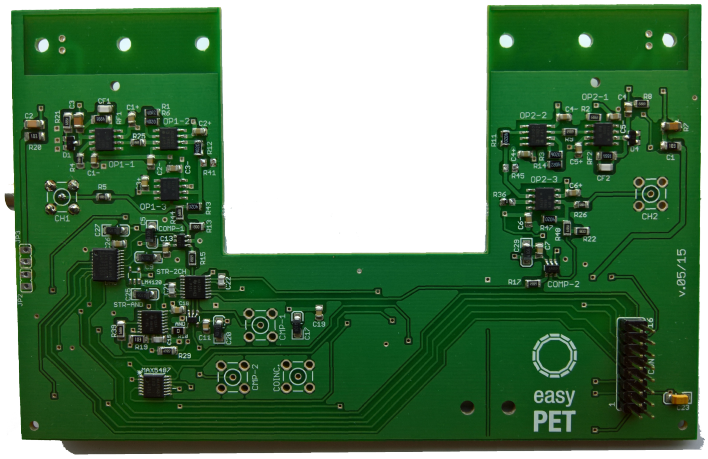

Figure 5.9: Detail of the easyPET U-board before the installation of the SiPMs and the scintillators.

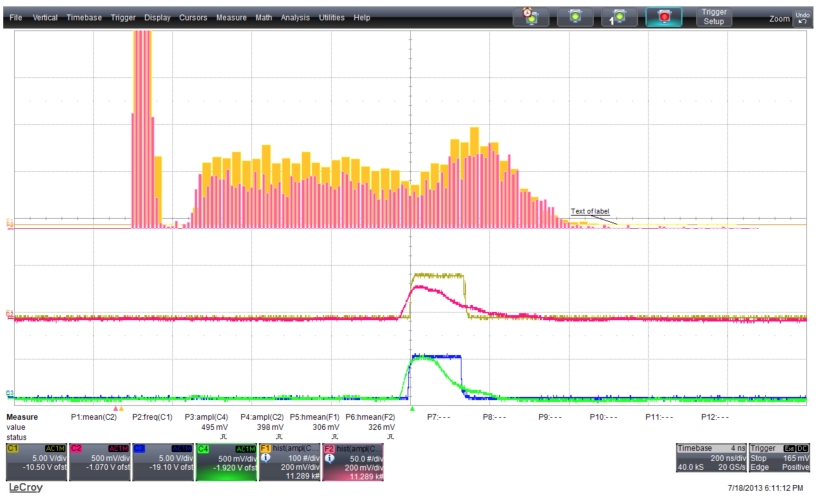

Figure 5.10: Scope capture with 2 detector histograms (top) and pulses in coincidence with comparator output triggered by a coincidence event.

5.4.2 Initial characterization of the easyPET system

System noise

The easyPET scanner comprises a single pair of cells. The noise contribution of each cell is due to crystal radioactivity, SiPM dark noise and electronic noise. As mentioned previously, two setup parameters of the easyPET system can affect the number of coincidence events. First, the threshold of each comparator defines the minimum amplitude of the photodetector signal to be considered and second the time coincidence window.

A simple study was performed to evaluate the relation between the threshold level and the event rate. In this study the threshold voltage is changed and the rate of events is recorded. The majority of SiPM pulses generated by dark noise and crosstalk are expected to be below 3 p.e. As the threshold increases, pulses below the threshold are neglected and so, between the amplitudes of two successive p.e. an abrupt change in frequency is expected. In Figure 5.11 it is depicted the obtained stair-case diagram for the SiPM dark noise, SiPM dark noise plus LYSO background and detector response with ^{22}Na radioactive source. The threshold level for the comparator was set with a *digital to analog converter* (DAC) controlled by an Arduino micro-controller also used for event counting. For each pulse with amplitude above the threshold a TTL signal is generated. The measurements were repeated for five SiPM bias voltages ($73 - 75$ V range). The SiPM gain increases with bias voltage, a fact that is observable by the larger steps in the staircase diagram (Figure 5.11), also due to the higher crosstalk probability. In addition, one can observe the increase of the number of steps due to the increase of SiPM dark noise. At 73 V the SiPM V_{bias} is above breakdown voltage but the gain is still low and the photo-peak plateaus are not clearly defined. When a ^{22}Na source is placed in front of the LYSO crystal, one can observe that the detector gets saturated, even close to the breakdown voltage. Typically, in applications such as TOF-PET, to decrease pulse rise-time the SiPMs are at a voltage where the signal reaches saturation. Although this fact is undesirable when measuring detector efficiency, it has no direct impact in coincidence mode operation.

Coincidence Window

To evaluate the role of the coincidence window to the total rate of accidental coincidences, several acquisitions were taken, varying the coincidence time window from the minimum (120 ns) to the maximum (1520 ns) allowed by the system. A ^{22}Na radioactive source with an activity $\sim$5 μCi was used. The source was placed at the center of the FOV. The SiPMs bias voltage were set to 73.6 V. An acquisition corresponding to a complete turn was performed, with a step of 0.9° for both top and bottom and acquisition time of 0.025 s per step. The TOP scan range was set to 54°. Before the acquisitions it was verified that the coincidence rate without the presence of the radioactive source was zero for both thresholds.

In figure 5.12, it is depicted the number of coincidence events for several window lengths in the $120 - 1520$ ns range, for threshold values of 60 and 150 mV for both channels. For

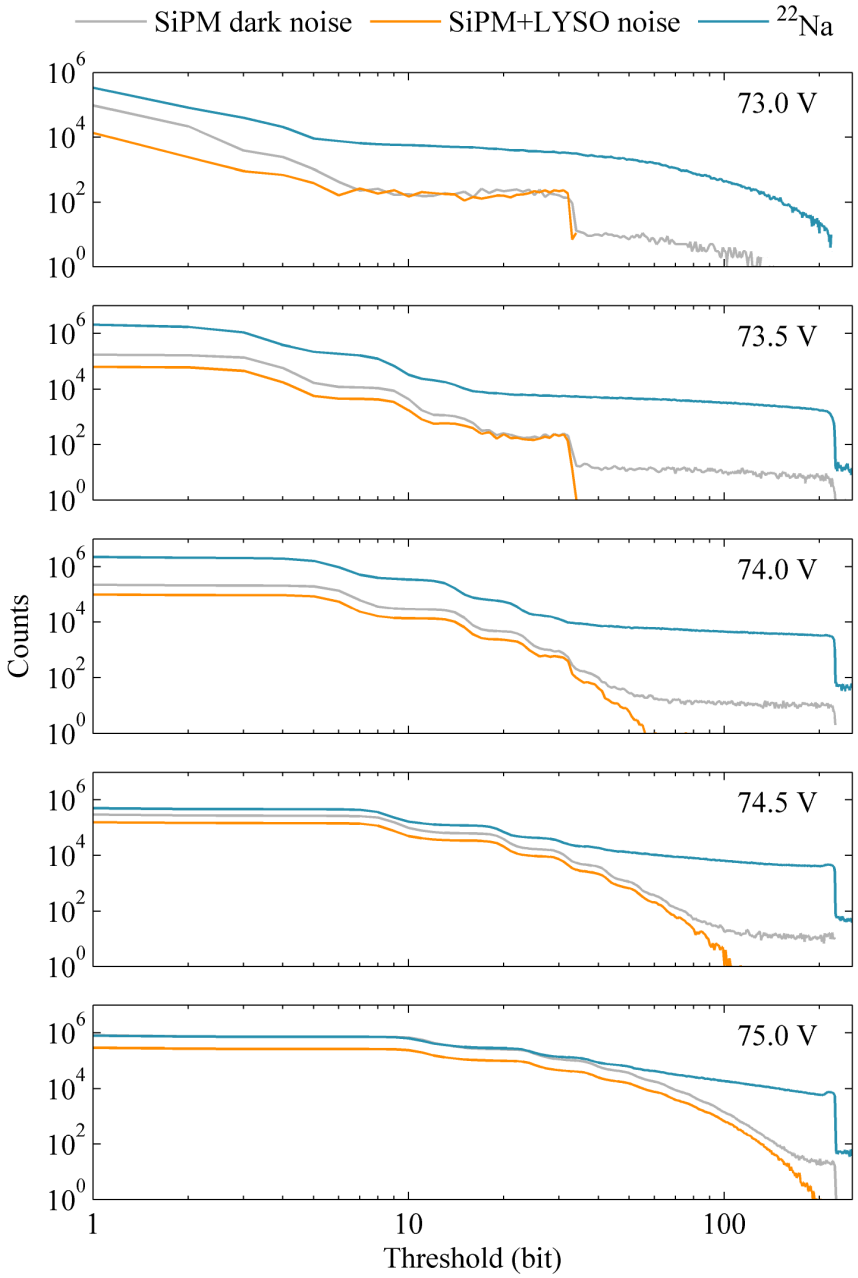

Figure 5.11: Single channel noise rate dependence on threshold.

a 2.5 increase in the threshold one can observe a decrease of the number of coincidences by the same magnitude, approximately. Considering Figure 5.11, for a threshold below 100 mV the typical counting rate is 10 kHz. Assuming equal counting rate for both detectors, from Eq. 5.1, the number of accidental coincidences for a coincidence window of 120 ns and 1520 ns would be 2 kHz and 30 kHz, respectively. As observed, for 60 mV there is an apparent increase in the number of events detected in coincidence while for a 150 mV threshold the system is not affected by the width of the coincidence window. This allows to verify that a proper threshold level is enough to reduce the number of false coincidences, improving the

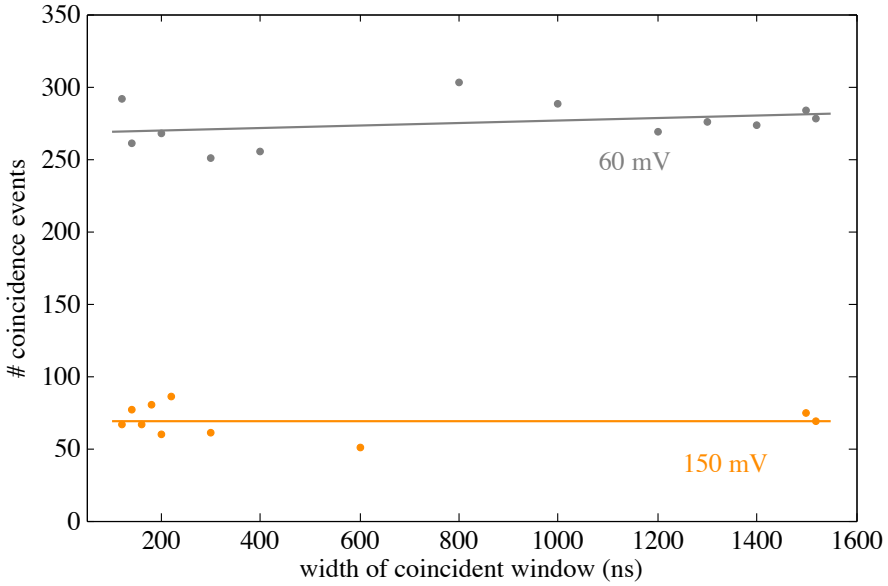

Figure 5.12: Number of coincidences using different window lengths.

system resolution. Although it must be noted that this threshold level must be such as to avoid discarding photons from Compton scattering events, at $\sim$ 340 keV.

It is known that a wider coincidence time window might reflect a higher number of events in coincidence. If a portion of these coincidence events are false, the image would present higher blur surrounding the source position. To check if this is observable, two images were acquired, using the shorter and wider windows allowed by the system (other ranges might be set by hardware adjustment). Five complete turns were performed, with a step of 0.9° for both top and bottom and an acquisition time of 25 ms per step (time per LOR). The SiPMs were biased at 75.37 V and the thresholds were set to 150 mv and 170 mV for channels 1 and 2, respectively. A total of 2391 and 4460 coincidence events were recorded for the 120 ns and 1520 ns coincidence windows, respectively, representing a 53% increase with the wider coincidence window. The two images are plotted in Figure 5.13. The higher background is clear for the larger coincidence window (Figure 5.13, right).

Images with multiple ^{22}Na sources

A simple evaluation of the system resolution of the easyPET was performed by the acquisition of several images of up to three 5 μCi ^{22}Na sources. Sources with two different dimensions were used, the smaller ones of Ø 2.54 mm, encapsulated in a Plexiglas cylinder with Ø 12.7 mm and 4.32 mm height (Spectrum Techniques, USA) and a larger source of Ø 6.35 mm encapsulated in a plastic disk with Ø 25.4 mm. The image obtained for the two smaller ^{22}Na sources placed side-by-side is presented in Figure 5.14 (left). The distance between the sources corresponds to the diameter of the Plexiglas, thus the sources are at $\sim$12.7 mm distance. A second image was taken with the additional source (Ø 25.4 mm)

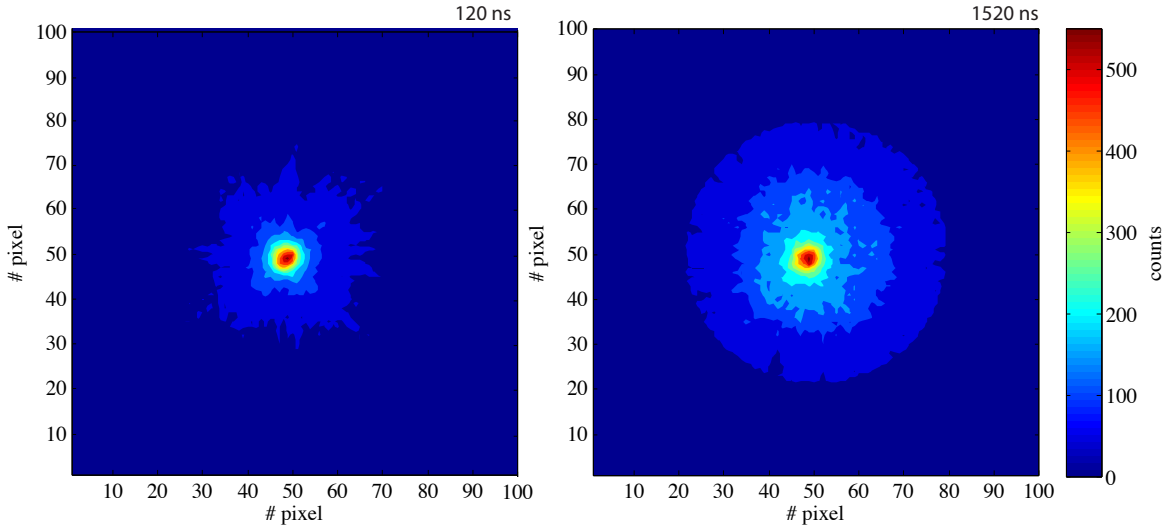

Figure 5.13: Images obtained with 120 ns (left) and 1520 ns (right) coincidence windows.

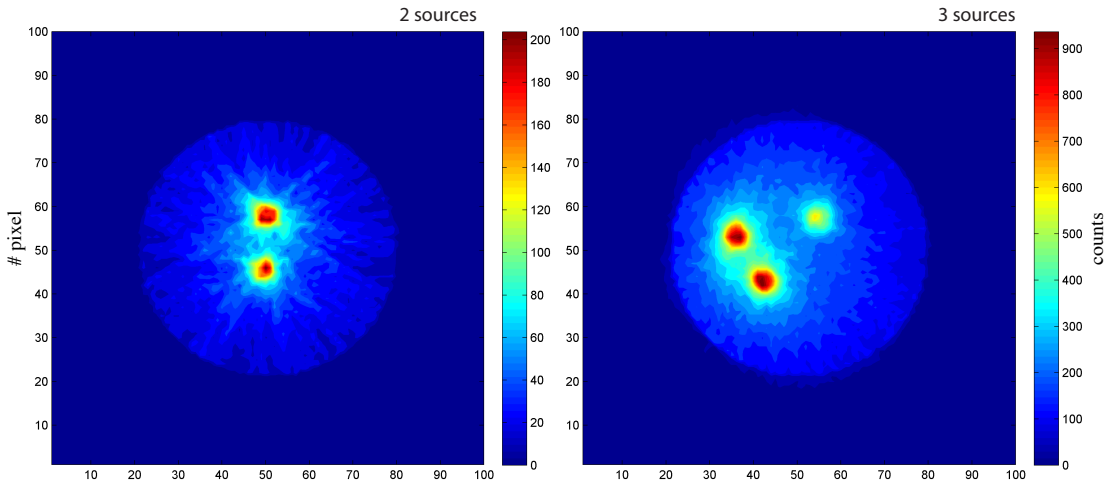

Figure 5.14: easyPET imagens acquired for two (left) and three (right) 5 μCi ^{22}Na sources.

(Figure 5.14, right). Both images were obtained with a step of 0.9° for both top and bottom step motors and an acquisition time of 25 ms per LOR. Both images presented in Figure 5.14 don't include additional filtering or reconstruction algorithms.

Test with ^{18}F-FDG radiotracer

Two tests where performed using ^{18}F-FDG radiotracer. A first test used a PMMA phantom with two cavities of 2 mm and 5 mm diameter, separated by 2 mm (center-to-center distance of 5.5 mm). The cavities were filled with ^{18}F-FDG radiotracer with a red dye diluted for easier identification (Figure 5.15, right). The acquisition was performed in a 20 min period with a with a top and bottom mottor step of 0.9 °. The image obtained is depicted in Figure 5.15, left.

The obtained image shows the capability of the easyPET system in terms of spatial resolution. The image pixel size is 250 μm.

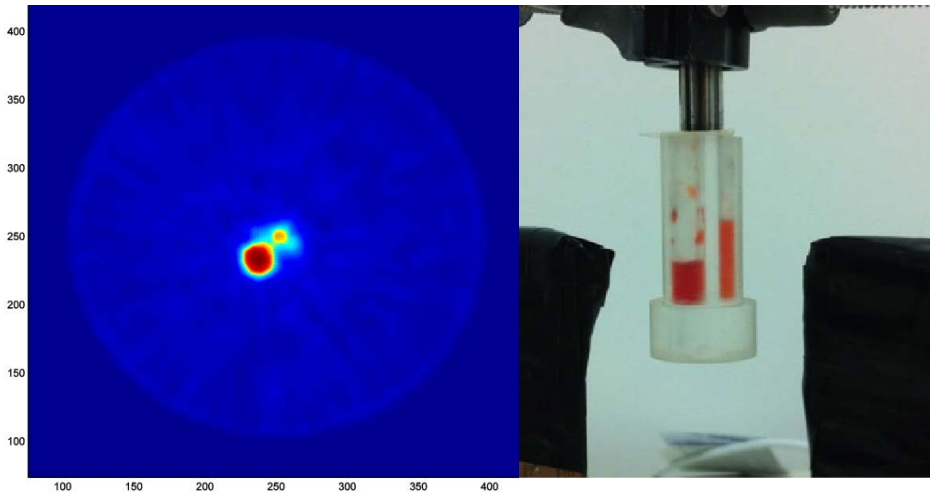

Figure 5.15: Image corresponding to ^{18}F-FDG radiotracer inserted in a PMMA phantom with two cavities of 2 mm and 5 mm diameter, separated by 2 mm (center-to-center distance of 5.5 mm).

A second test was done using a lab rat, injected with ^{18}F-FDG radiotracer. Post-mortem the heart and liver were removed. The image was obtained by simple back-projection, without any filtering (Figure 5.16). The easyPET system resolution allows the identification of the heart's left and right auricular and ventricular cavities.

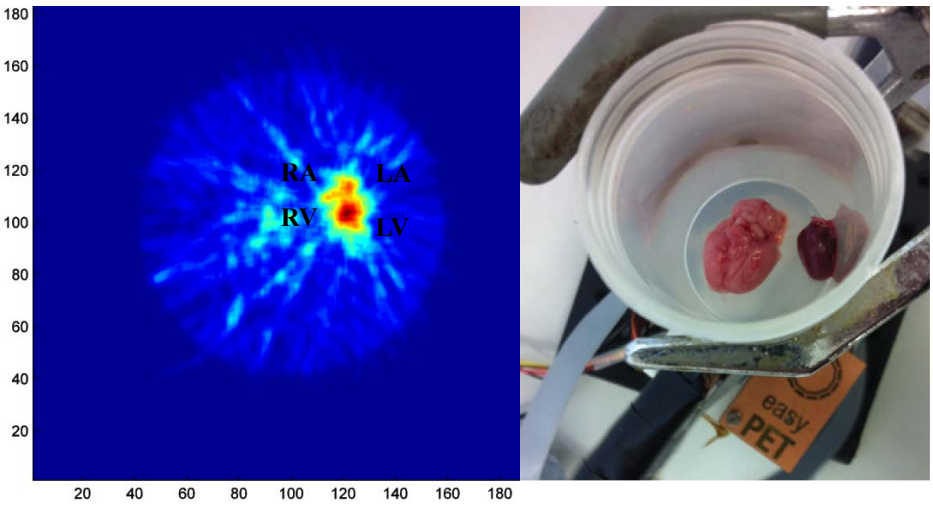

Figure 5.16: Image corresponding to scan of lab rat heart's left and right auricular (LA, RA) and ventricular (LV, RV) cavities injected with ^{18}F-FDG radiotracer.

5.5 Final remarks

A PET scanner should present some key features such as high detection efficiency, high spatial resolution, low dead time, good timing resolution and good energy resolution [316].

The easyPET is a fully functional small-size PET system. This system is suitable for educational purposes as a tool for learning PET physics and electronics. This small FOV high resolution system is limited to 2D imaging and requires no DOI correction. From the several studies performed, namely with multiple radioactive sources, a position resolution of $\sim$1 mm has been observed [317], believed to be limited by the crystal width. Typical animal PET systems have lower ring diameter allowing sub-millimeter spatial resolution [318, 319] compared to the 4–6 mm FWHM of human PET scanners [317].

The lower number of cells relative to other preclinical devices results in lower sensitivity. On the other hand, a lower number of readout channels simplifies the instrumentation and decreases the detector cost. The system can be scaled up to several pairs of cells, increasing sensitivity thus allowing application as preclinical PET scanner.

The easyPET technology has been patented and licensed to CAEN[2]. An improved version of the system is under development. In addition, an extended version is being developed comprehending multiple pair of detector cells, allowing 3D imaging, thus opening the possibility for application has a pre-clinical system.

[2]http://www.caen.it

Conclusion

The studies conducted within this PhD envisaged the application of novel silicon photodetectors in different research fields. The versatility of the silicon photomultipliers allows for current and pulse mode operation, making it easy to adapt to the application in concern. Several solutions to overcome some of the shortcomes of these detectors have been proposed and evaluated.

In applications such as the tracking plane for the NEXT detector, high demands are imposed. One of the major requirements for NEXT as a neutrinoless double beta decay experiment is to achieve the lowest possible radiation background and high sensitivity to identify the topological signature expected from the $0\nu\beta\beta$-decay. The Hamamastsu MPPCs are one of the best SiPMs available, presenting the highest PDE in the blue region and low crosstalk. However, in the radiation screening tests at Laboratorio Subterraneo de Canfranc, these revealed levels of radioactivity above the desired. For this reason, SensL SiPMs are the present choice for the NEXT detector tracking plane.

The NEXT detector is expected to be scaled to 1 tonne before 2020. Preparing this demanding task, several options are under evaluation, namely the use of scintillating optical fibers for topological signature recognition. Considering this, several studies were conducted with a scintillating optical fiber with emission in the blue region, the region of highest PDE of typical SiPMs.

The application of the developed technologies in the society is always a goal. Having this principle in mind, several projects came to life, namely a radiation dosimeter for use in prostate brachytherapy and a small PET scanner for educational purposes. Both technologies have been licensed and are expected to be in the market in 2017 and 2016, respectively.

The prostate brachytherapy dosimeter could have a major impact in the quality of treatments and consequently, in the improvement of patient outcome in these treatments.

The SiPM is an attractive photosensor for low light level regimes. The lower cost comparatively with other single photon detectors, such as the PMT, allows the wide implementation in experiments or equipments, from medical applications to particle physics or high energy physics, where a single experiment typically requires thousands of these photosensors. The MPPCs present some limitations, e.g. high crosstalk, that could be surpassed with future SiPM generations.

A radiation dosimeter and an educational PET system using SiPMs were successfully prototyped. From this initial experience, the biggest concern encountered was the difficulty

of gain stabilization due to temperature variations. In one perspective, where a single or a couple of SiPMs are used, this control may be straightforward, however in applications using hundreds of SiPMs the gain adjustment is a great concern and needs to be cost effective. Considering the recent participation of our group in the NEXT experiment, new challenges arise.

References

[1] M. Green et al., "*The MAJORANA DEMONSTRATOR for* $0\nu\beta\beta$*: Current Status and Future Plans*", Physics Procedia, vol. 61, pp. 232 - 240, 2015.

[2] K. Zuber, "*Status and perspectives of double beta decay searches*", Journal of Physics: Conference Series, vol. 578, no. 1, pp. 012007, 2015.

[3] V. Barger, D. Marfatia and K. Whisnant, "*The Physics of Neutrinos*", Princeton University Press, 2012.

[4] M. Auger et al., "*The EXO-200 detector, part I: detector design and construction*", Journal of Instrumentation, vol. 7, no. 05, pp. P05010, 2012.

[5] S. M. Bilenky and C. Giunti, "*Neutrinoless double-beta decay: A probe of physics beyond the Standard Model*", International Journal of Modern Physics A, vol. 30, no. 04n05, pp. 1530001, 2015.

[6] O. Cremonesi and M. Pavan, "*Challenges in Double Beta Decay,*", Advances in High Energy Physics, vol. 2014, 2014.

[7] J. Heeck, "*Unbroken* $B-L$ *symmetry*", Physics Letters B, vol. 739, pp. 256 - 262, 2014.

[8] J. Greene, "*Neutrinos: properties, sources and detection*", Academic Press, pp. xxiv, 764 p., 2007.

[9] S. Pascoli and S. Petcov, "*The SNO solar neutrino data, neutrinoless double beta-decay and neutrino mass spectrum*", Physics Letters B, vol. 544, no. 3–4, pp. 239 - 250, 2002.

[10] J. J. Gómez-Cadenas and J. Martín-Albo, "*Phenomenology of neutrinoless double beta decay*", PoS, vol. GSSI14, pp. 004, 2015.

[11] S. M. Bilenky and C. Giunti, "*Neutrinoless double beta decay: a brief review*", Modern Physics Letters A, vol. 27, no. 13, pp. 1230015, 2012.

[12] J. Martín-Albo et al., "*Sensitivity of NEXT-100 to neutrinoless double beta decay*", Journal of High Energy Physics, vol. 2016, no. 5, pp. 1–30, 2016.

[13] T. N. collaboration, "*NEXT a high-pressured xenon-based experiments for ultimate sensitivity to a Majorana neutrino*", European Strategy Preparatory Group, 2012.

[14] J. Kotila and F. Iachello, "*Phase-space factors for double-β decay*", Phys. Rev. C, vol. 85, pp. 034316, 2012.

[15] K. Asakura, others et al., "*Results from KamLAND-Zen*", AIP Conf. Proc., vol. 1666, pp. 170003, 2015.

[16] J. N. Bahcall, H. Murayama and C. Pena-Garay, "*What can we learn from neutrinoless double beta decay experiments?*", Phys. Rev., vol. D70, pp. 033012, 2004.

[17] H. Klapdor-Kleingrothaus, "*Double beta decay and neutrino mass. The Heidelberg-Moscow experiment*", Progress in Particle and Nuclear Physics, vol. 32, pp. 261 - 280, 1994.

[18] L. Baudis et al., "*The Heidelberg-Moscow experiment: improved sensitivity for 76Ge neutrinoless double beta decay*", Physics Letters B, vol. 407, no. 3–4, pp. 219 - 224, 1997.

[19] H. Klapdor-Kleingrothaus et al., "*Latest results from the HEIDELBERG-MOSCOW double beta decay experiment*", The European Physical Journal A - Hadrons and Nuclei, vol. 12, no. 2, pp. 147–154, 2001.

[20] H. Klapdor-Kleingrothaus et al., "*Search for neutrinoless double beta decay with enriched 76Ge in Gran Sasso 1990–2003*", Physics Letters B, vol. 586, no. 3–4, pp. 198 - 212, 2004.

[21] H. Klapdor-Kleingrothaus et al., "*Data acquisition and analysis of the 76Ge double beta experiment in Gran Sasso 1990–2003*", Nuclear Instruments and Methods in Physics Research Section A: Accelerators, Spectrometers, Detectors and Associated Equipment, vol. 522, no. 3, pp. 371 - 406, 2004.

[22] H. Klapdor-Kleingrothaus, "*First evidence for neutrinoless double beta decay, with enriched ^{76}Ge in Gran Sasso 1990-2003*", Nuclear Physics B - Proceedings Supplements, vol. 143, pp. 229 - 232, 2005.

[23] Y. Zdesenko, F. Danevich and V. Tretyak, "*Has neutrinoless double β decay of ^{76}Ge been really observed?*", Physics Letters B, vol. 546, no. 3–4, pp. 206 - 215, 2002.

[24] S. Biller, "*SNO+ with Tellurium*", Phys. Procedia, vol. 61, pp. 205-210, 2015.

[25] A. Barabash and F. Piquemal, "*Double Beta Decay Experiments: Beginning of a New Era*", Nuclear Physics News, vol. 23, no. 3, pp. 12-18, 2013.

[26] F. Piquemal, "*NEMO 3: the goals, results and legacy*", http://cerncourier.com/cws/article/cern/48344 accessed on june 2016., 2012.

[27] B. Wonsak, "*Status and Perspectives of the COBRA Experiment*", Physics Procedia, vol. 61, pp. 295 - 299, 2015.

[28] I. C. Bandac, "*Search for neutrinoless double beta decay with the CUORE detector*", Journal of Physics: Conference Series, vol. 110, no. 8, pp. 082001, 2008.

[29] L. Canonica et al., "*Results of CUORE-0 and prospects for the CUORE experiment*", Nuclear and Particle Physics Proceedings, vol. 265–266, pp. 73 - 76, 2015.

[30] A. Vignati et al., "*First data from CUORE-0*", Physics Procedia, vol. 61, pp. 289 - 294, 2015.

[31] F. Alessandria et al., "*Sensitivity of CUORE to Neutrinoless Double-Beta Decay*", arXiv, 2011.

[32] "*Search for Majorana Neutrinos near the Inverted Mass Hierarchy region with KamLAND-Zen*", 2016.

[33] T. E. . Collaboration, "*Search for Majorana neutrinos with the first two years of EXO-200 data*", Nature, vol. 510, no. 7504, pp. 229–234, 2014.

[34] V. Álvarez et al., "*NEXT-100 Technical Design Report (TDR). Executive summary*", Journal of Instrumentation, vol. 7, no. 06, pp. T06001, 2012.

[35] D. Lorca et al., "*Characterisation of NEXT-DEMO using xenon K_α X-rays*", Journal of Instrumentation, vol. 9, no. 10, pp. P10007, 2014.

[36] V. Álvarez et al., "*Near-Intrinsic Energy Resolution for 30 to 662 keV Gamma Rays in a High Pressure Xenon Electroluminescent TPC*", arxiv, 2012.

[37] K. Twelker and S. Kravitz, "*Barium Tagging from nEXO Using Resonance Ionization Spectroscopy*", Physics Procedia, vol. 61, pp. 278 - 282, 2015.

[38] M. K. Moe, "*Detection of neutrinoless double-beta decay*", Phys. Rev. C, vol. 44, pp. R931–R934, 1991.

[39] B. Mong, "*Barium tagging in solid xenon for the EXO experiment*", 2011.

[40] B. Mong et al., "*Spectroscopy of Ba and* Ba^+ *deposits in solid xenon for barium tagging in nEXO*", Phys. Rev. A, vol. 91, pp. 022505, 2015.

[41] J. E. Sansonetti and J. J. Curry, "*Wavelengths, Transition Probabilities, and Energy Levels for the Spectra of Barium (BaIII through BaLVI)*", Journal of Physical and Chemical Reference Data, vol. 39, no. 4, 2010.

[42] V. Álvarez et al., "*Initial results of NEXT-DEMO, a large-scale prototype of the NEXT-100 experiment*", Journal of Instrumentation, vol. 8, no. 04, pp. P04002, 2013.

[43] V. Álvarez et al., "*SiPMs coated with TPB: coating protocol and characterization for NEXT*", Journal of Instrumentation, vol. 7, no. 02, pp. P02010, 2012.

[44] P. Ferrario et al., "*First proof of topological signature in the high pressure xenon gas TPC with electroluminescence amplification for the NEXT experiment*", Journal of High Energy Physics, vol. 2016, no. 1, pp. 1–18, 2016.

[45] V. Álvarez et al., "*Operation and first results of the NEXT-DEMO prototype using a silicon photomultiplier tracking array*", Journal of Instrumentation, vol. 8, no. 09, pp. P09011, 2013.

[46] S. Cebrián et al., "*Radiopurity assessment of the tracking readout for the NEXT double beta decay experiment*", Journal of Instrumentation, vol. 10, no. 05, pp. P05006, 2015.

[47] J. Renner et al., "*Characterization of Nuclear Recoils in High Pressure Xenon Gas: Towards a Simultaneous Search for WIMP Dark Matter and Neutrinoless Double Beta Decay*", Physics Procedia, vol. 61, pp. 766 - 773, 2015.

[48] V. Álvarez et al., "*Operation and first results of the NEXT-DEMO prototype using a silicon photomultiplier tracking array*", Journal of Instrumentation, vol. 8, no. 09, pp. P09011, 2013.

[49] K. Lung, others et al., "*Characterization of the Hamamatsu R11410-10 3-Inch Photomultiplier Tube for Liquid Xenon Dark Matter Direct Detection Experiments*", Nucl. Instrum. Meth., vol. A696, pp. 32-39, 2012.

[50] M. Garcia, "*Light Conversion and Transmission Studies for the NEXT Experiment*", 2014.

[51] Hamamatsu, "*Multi-Pixel Photon Counter*", 2007.

[52] N. Pavlov, G. Mashlum and D. Meier, "*Gamma spectroscopy using a silicon photomultiplier and a scintillator*", In *IEEE Nuclear Science Symposium Conference Record, 2005*, 2005.

[53] F. Villa et al., "*SPICE Electrical Models and Simulations of Silicon Photomultipliers*", IEEE Transactions on Nuclear Science, vol. 62, no. 5, pp. 1950-1960, 2015.

[54] F. Corsi et al., "*Electrical Characterization of Silicon Photo-Multiplier Detectors for Optimal Front-End Design*", In *2006 IEEE Nuclear Science Symposium Conference Record*, 2006.

[55] S. Seifert et al., "*Simulation of Silicon Photomultiplier Signals*", IEEE Transactions on Nuclear Science, vol. 56, no. 6, pp. 3726-3733, 2009.

[56] D. Marano et al., "*Improved SPICE electrical model of silicon photomultipliers*", Nuclear Instruments and Methods in Physics Research Section A: Accelerators, Spectrometers, Detectors and Associated Equipment, vol. 726, pp. 1 - 7, 2013.

[57] V. Álvarez et al., "*Radiopurity control in the NEXT-100 double beta decay experiment: procedures and initial measurements*", Journal of Instrumentation, vol. 8, no. 01, pp. T01002, 2013.

[58] S. Cebrián et al., "*Radon and material radiopurity assessment for the NEXT double beta decay experiment*", AIP Conference Proceedings, vol. 1672, 2015.

[59] V. Álvarez et al., "*Design and characterization of the SiPM tracking system of NEXT-DEMO, a demonstrator prototype of the NEXT-100 experiment*", Journal of Instrumentation, vol. 8, no. 05, pp. T05002, 2013.

[60] N. Yahlali et al., "*SiPM Readout Technique in a High Pressure Xenon Electroluminescent TPC for neutrinoless $\beta\beta$ decay searches*", 2016.

[61] Vertilon, "*Readout Techniques for Silicon Photomultipliers - Application note*", 2015.

[62] G. Bonanno et al., "*Characterization Measurements Methodology and Instrumental Set-Up Optimization for New SiPM Detectors Part I: Electrical Tests*", IEEE Sensors Journal, vol. 14, no. 10, pp. 3557-3566, 2014.

[63] G. Bonanno et al., "*Characterization Measurements Methodology and Instrumental Set-Up Optimization for New SiPM Detectors Part II: Optical Tests*", IEEE Sensors Journal, vol. 14, no. 10, pp. 3567-3578, 2014.

[64] D. Marano et al., "*Electro-optical characterization of MPPC detectors for the ASTRI Cherenkov telescope camera*", Nuclear Instruments and Methods in Physics Research Section A: Accelerators, Spectrometers, Detectors and Associated Equipment, vol. 768, pp. 32 - 42, 2014.

[65] P. Marrocchesi et al., "*Active control of the gain of a Silicon PhotoMultiplier*", Nuclear Instruments and Methods in Physics Research Section A: Accelerators, Spectrometers, Detectors and Associated Equipment, vol. 602, no. 2, pp. 391 - 395, 2009.

[66] Z. Li et al., "*A gain control and stabilization technique for Silicon Photomultipliers in low-light-level applications around room temperature*", Nuclear Instruments and Methods in Physics Research Section A: Accelerators, Spectrometers, Detectors and Associated Equipment, vol. 695, pp. 222 - 225, 2012.

[67] F. Licciulli, I. Indiveri and C. Marzocca, "*A Novel Technique for the Stabilization of SiPM Gain Against Temperature Variations*", Nuclear Science, IEEE Transactions on, vol. 60, no. 2, pp. 606-611, 2013.

[68] N. Yahlali, L. Fernandes and D. Lorca, "*Characterization of UV-enhanced SiPMs for imaging in a high pressure xenon electroluminescent TPC*", In *Advancements in Nuclear Instrumentation Measurement Methods and their Applications (ANIMMA), 2013 3rd International Conference on*, 2013.

[69] N. Yahlali et al., "*Imaging with SiPMs in noble-gas detectors*", Journal of Instrumentation, vol. 8, no. 01, pp. C01003, 2013.

[70] D. L. Presti, D. L. Bonanno and F. Longhitano, "*Development of a Real-Time, Large Area, High Spatial Resolution Particle Tracker Based on Scintillating Fibers*", Advances in High Energy Physics, vol. 2014, pp. 13, 2014.

[71] T. Armstrong et al., "*The E864 lead-scintillating fiber hadronic calorimeter*", Nuclear Instruments and Methods in Physics Research Section A: Accelerators, Spectrometers, Detectors and Associated Equipment, vol. 406, no. 2, pp. 227 - 258, 1998.

[72] I. Castro et al., "*Development of a light readout based on silicon photomultipliers for a wavelength-shifting fibre gamma camera*", Nuclear Instruments and Methods in Physics Research Section A: Accelerators, Spectrometers, Detectors and Associated Equipment, vol. 695, pp. 298 - 302, 2012.

[73] I. F. Castro et al., "*Characterization of a small CsI(Na)-WSF-SiPM gamma camera prototype using 99 m Tc*", Journal of Instrumentation, vol. 8, no. 03, pp. C03008, 2013.

[74] F. Therriault-Proulx et al., "*Development of a novel multi-point plastic scintillation detector with a single optical transmission line for radiation dose measurement*", Physics in Medicine and Biology, vol. 57, no. 21, pp. 7147, 2012.

[75] L. Archambault et al., "*Plastic scintillation dosimetry: Optimal selection of scintillating fibers and scintillators*", Medical Physics, vol. 32, no. 7, 2005.

[76] L. Moutinho, "*Desenvolvimento de um dosimetro gama para braquiterapia*", 2010.

[77] V. Álvarez et al., "*Ionization and scintillation response of high-pressure xenon gas to alpha particles*", Journal of Instrumentation, vol. 8, no. 05, pp. P05025, 2013.

[78] V. Álvarez et al., "*Description and commissioning of NEXT-MM prototype: first results from operation in a Xenon-Trimethylamine gas mixture*", Journal of Instrumentation, vol. 9, no. 03, pp. P03010, 2014.

[79] S. Cebrián et al., "*Present Status and Future Perspectives of the NEXT Experiment,*", Advances in High Energy Physics, vol. 2014, 2014.

[80] V. Álvarez et al., "*Characterization of a medium size Xe/TMA TPC instrumented with microbulk Micromegas, using low-energy γ-rays*", Journal of Instrumentation, vol. 9, no. 04, pp. C04015, 2014.

[81] L. Serra et al., "*An improved measurement of electron-ion recombination in high-pressure xenon gas*", Journal of Instrumentation, vol. 10, no. 03, pp. P03025, 2015.

[82] J. Renner et al., "*Ionization and scintillation of nuclear recoils in gaseous xenon*", Nuclear Instruments and Methods in Physics Research Section A: Accelerators, Spectrometers, Detectors and Associated Equipment, vol. 793, pp. 62 - 74, 2015.

[83] N. Dinu, A. Nagai and A. Para, "*Studies of MPPC detectors down to cryogenic temperatures*", Nuclear Instruments and Methods in Physics Research Section A: Accelerators, Spectrometers, Detectors and Associated Equipment, vol. 787, pp. 275 - 279, 2015.

[84] C. Abate-Shen and M. M. Shen, "*Diagnostics: The prostate-cancer metabolome*", Nature, vol. 457, no. 7231, pp. 799–800, 2009.

[85] T. Maurer et al., "*Current use of PSMA-PET in prostate cancer management*", Nat Rev Urol, vol. advance online publication, pp. –, 2016.

[86] C. R. King, "*LDR vs. HDR brachytherapy for localized prostate cancer: the view from radiobiological models*", Brachytherapy, vol. 1, no. 4, pp. 219 - 226, 2002.

[87] G. Morton and P. Hoskin, "*Brachytherapy: Current Status and Future Strategies - Can High Dose Rate Replace Low Dose Rate and External Beam Radiotherapy?*", Clinical Oncology, vol. 25, no. 8, pp. 474 - 482, 2013.

[88] J. Michalski et al., "*Radiation exposure to family and household members after prostate brachytherapy*", International Journal of Radiation Oncology*Biology*Physics, vol. 56, no. 3, pp. 764 - 768, 2003.

[89] I. S. Grills et al., "*High Dose Rate Brachytherapy as Prostate Cancer Monotherapy Reduces Toxicity Compared to Low Dose Rate Palladium Seeds*", The Journal of Urology, vol. 171, no. 3, pp. 1098 - 1104, 2004.

[90] F. Cattani et al., "*Radiation exposure after permanent prostate brachytherapy*", Radiotherapy and Oncology, vol. 79, no. 1, pp. 65 - 69, 2006.

[91] J. Skowronek, "*Low-dose-rate or high-dose-rate brachytherapy in treatment of prostate cancer –between options*", Journal of Contemporary Brachytherapy, vol. 5, no. 1, pp. 33–41, 2013.

[92] R. Taschereau, J. Roy and J. Pouliot, "*Monte Carlo simulations of prostate implants to improve dosimetry and compare planning methods*", Medical Physics, vol. 26, no. 9, 1999.

[93] A. Rosenfeld et al., "*In vivo dosimetry and seed localization in prostate brachytherapy with permanent implants*", Nuclear Science, IEEE Transactions on, vol. 51, no. 6, pp. 3013-3018, 2004.

[94] T. Simnor et al., "*Justification for inter-fraction correction of catheter movement in fractionated high dose-rate brachytherapy treatment of prostate cancer*", Radiotherapy and Oncology, vol. 93, no. 2, pp. 253 - 258, 2009.

[95] E. J. B. Gurp et al., "*In Vivo Dosimetry Using a Linear Mosfet-Array Dosimeter to Determine the Urethra Dose In ^{125}I Permanent Prostate Implants*", International Journal of Radiation Oncology*Biology*Physics, vol. 73, no. 1, pp. 314 - 321, 2009.

[96] J. S. Eshleman et al., "*Radioactive seed migration to the chest after transperineal interstitial prostate brachytherapy: extraprostatic seed placement correlates with migration*", International Journal of Radiation Oncology*Biology*Physics, vol. 59, no. 2, pp. 419 - 425, 2004.

[97] D. B. Fuller, J. A. Koziol and A. C. Feng, "*Prostate brachytherapy seed migration and dosimetry: analysis of stranded sources and other potential predictive factors*", Brachytherapy, vol. 3, no. 1, pp. 10 - 19, 2004.

[98] S. Daniel et al., "*Three-dimensional visualization and dosimetry of stranded source migration following prostate seed implant*", Practical Radiation Oncology, vol. 2, no. 3, pp. 193 - 200, 2012.

[99] S. J. Damore et al., "*Needle displacement during HDR brachytherapy in the treatment of prostate cancer*", International Journal of Radiation Oncology*Biology*Physics, vol. 46, no. 5, pp. 1205 - 1211, 2000.

[100] L. Archambault et al., "*Toward a Real-Time In Vivo Dosimetry System Using Plastic Scintillation Detectors*", International Journal of Radiation Oncology Biology Physics, vol. 78, no. 1, pp. 280-287, 2010.

[101] C. M. Able, M. Bright and B. Frizzell, "*Quality Control of High-Dose-Rate Brachytherapy: Treatment Delivery Analysis Using Statistical Process Control*", International Journal of Radiation Oncology*Biology*Physics, vol. 85, no. 3, pp. 828 - 833, 2013.

[102] A. A. o. P. i. Medicine, "*Code of practice for brachytherapy physics Report of the AAPM Radiation Therapy Committee Task Group No 56*", 1997 .

[103] P. Vaz, "*Radiation protection and dosimetry issues in the medical applications of ionizing radiation*", Radiation Physics and Chemistry, vol. 104, pp. 23 - 30, 2014.

[104] Y. Su et al., "*Dosimetry accuracy as a function of seed localization uncertainty in permanent prostate brachytherapy: increased seed number correlates with less variability in prostate dosimetry*", Physics in Medicine and Biology, vol. 52, no. 11, pp. 3105, 2007.

[105] S. Smathers et al., "*Radiation safety parameters following prostate brachytherapy*", International Journal of Radiation Oncology*Biology*Physics, vol. 45, no. 2, pp. 397 - 399, 1999.

[106] G. Briggs et al., "*Towards Safer Radiotherapy*", The Royal College of Radiologists, 2008.

[107] S. Mattsson and M. Soderberg, Radiation Protection in Nuclear Medicine, Chapter Dose Quantities and Units for Radiation Protection, pp. 7–18, Springer Berlin Heidelberg, 2013.

[108] IAEA, "*Calibration of radiation protection monitoring instruments.*", IAEA, 2000.

[109] G. F. Knoll, "*Radiation detection and measurement*", John Wiley & Sons, pp. xiv, 802 p., 2000.

[110] E. B. Podgorsak, "*Radiation Oncology Physics: A Handbook for Teachers and Students*", IAEA, 2005.

[111] H. Cember and T. Johnson, "*Introduction to Health Physics*", McGraw Hill Medical, 2009.

[112] R. Nath et al., "*Dosimetry of interstitial brachytherapy sources: Recommendations of the AAPM Radiation Therapy Committee Task Group No. 43*", Medical Physics, vol. 22, no. 2, 1995.

[113] M. J. Rivard et al., "*Update of AAPM Task Group No. 43 Report: A revised AAPM protocol for brachytherapy dose calculations*", Medical Physics, vol. 31, no. 3, 2004.

[114] M. Thorne, "*ICRP publication 60: 1990 recommendations of the international commission on radiological protection*", Annals of Nuclear Energy, vol. 19, no. 1, pp. 51 - 52, 1992.

[115] K. Eckerman et al., "*ICRP Publication 119: Compendium of Dose Coefficients based on ICRP Publication 60*", Annals of the ICRP, vol. 42, no. 4, pp. e1 - e130, 2013.

[116] ICRP, "*Basis for dosimetric quantities used in radiological protection*", International Commission on Radiological Protection, 2005.

[117] D. T. Bartlett, "*Personal dose equivalent, Hp(d), and reference point for calibration*", Radiation Protection Dosimetry, vol. 121, no. 3, pp. 209-210, 2006.

[118] F. Attix, "*Introduction to Radiological Physics and Radiation Dosimetry*", Wiley, 1991.

[119] E. B. Podgorsak, "*Radiation physics for medical physicists*", Springer, pp. xxi, 437 p., 2006.

[120] H. Bouchard, "*A theoretical re-examination of Spencer-Attix cavity theory*", Physics in Medicine and Biology, vol. 57, no. 11, pp. 3333, 2012.

[121] D. J. La Russa and D. W. O. Rogers, "*Accuracy of Spencer-Attix cavity theory and calculations of fluence correction factors for the air kerma formalism*", Medical Physics, vol. 36, no. 9, 2009.

[122] P. Puente and A. K. Azab, "*Delivery systems for brachytherapy*", Journal of Controlled Release, vol. 192, pp. 19 - 28, 2014.

[123] C. M. Cha et al., "*Isotope selection for patients undergoing prostate brachytherapy*", International Journal of Radiation Oncology*Biology*Physics, vol. 45, no. 2, pp. 391 - 395, 1999.

[124] B. Reniers et al., "*Calculation of relative biological effectiveness of a low-energy electronic brachytherapy source*", Physics in Medicine and Biology, vol. 53, no. 24, pp. 7125, 2008.

[125] T. Kehwar, "*Use of Cesium-131 radioactive seeds in prostate permanent implants*", J Med Phys., vol. 34(4), pp. 191-193, 2009.

[126] C. R. UK, "*Internal radiotherapy (brachytherapy) for prostate cancer*", 2014.

[127] K. Tanderup et al., "*In vivo dosimetry in brachytherapy*", Medical Physics, vol. 40, no. 7, pp. -, 2013.

[128] B. Lee et al., "*Measurements of Relative Depth Doses Using Fiber-Optic Radiation Sensor and EBT Film for Brachytherapy Dosimetry*", Nuclear Science, IEEE Transactions on, vol. 57, no. 3, pp. 1496-1501, 2010.

[129] A. J. Cherpak et al., "*Clinical use of a novel in-vivo 4D monitoring system for simultaneous patient motion and dose measurements*", Radiotherapy and Oncology, vol. 102, no. 2, pp. 290–296, 2012.

[130] A. J. Cherpak et al., "*Real-time measurement of urethral dose and position during permanent seed implantation for prostate brachytherapy*", Brachytherapy, vol. 13, no. 2, pp. 169–177, 2014.

[131] K. Chuamsaamarkkee et al., "*Skin dosimetry of thyroid radioiodine with MOSkin detector: A phantom study*", In *Nuclear Science Symposium and Medical Imaging Conference (NSS/MIC), 2011 IEEE*, 2011.

[132] PTW, "*PTW diamond dosimeter catalog*", .

[133] J. F. Williamson et al., "*Plastic scintillator response to low-energy photons*", Physics in Medicine and Biology, vol. 44, no. 4, pp. 857, 1999.

[134] A. Beddar, T. Mackie and F. Attix, "*Water-equivalent plastic scintillation detectors for high-energy beam dosimetry: II. Properties and measurement*", Phys. Med. Biol., vol. 37, no. 10, pp. 1901, 1992.

[135] A. Beddar et al., "*Monte Carlo calculations of the absorbed dose and energy dependence of plastic scintillators*", Med. Phys., vol. 32, no. 5, pp. 1265, 2005.

[136] A. M. Frelin et al., "*Comparative Study of Plastic Scintillators for Dosimetric Applications*", Nuclear Science, IEEE Transactions on, vol. 55, no. 5, pp. 2749-2756, 2008.

[137] F. Lessard et al., "*Validating plastic scintillation detectors for photon dosimetry in the radiologic energy range*", Medical Physics, vol. 39, no. 9, 2012.

[138] L. Beaulieu et al., "*Current status of scintillation dosimetry for megavoltage beams*", Journal of Physics: Conference Series, vol. 444, no. 1, pp. 012013, 2013.

[139] L. Peralta and F. Rêgo, "*Response of plastic scintillators to low-energy photons*", Physics in Medicine and Biology, vol. 59, no. 16, pp. 4621-4633, 2014.

[140] H. Yücel et al., "*Determination of the energy dependence of the BC-408 plastic scintillation detector in medium energy x-ray beams*", Physics in Medicine and Biology, vol. 59, no. 22, pp. 6749, 2014.

[141] B. Lee et al., "*Effects of Temperature and X-rays on Plastic Scintillating Fiber and Infrared Optical Fiber*", Sensors, vol. 15, no. 5, pp. 11012, 2015.

[142] L. Wootton and S. Beddar, "*Temperature dependence of BCF plastic scintillation detectors*", Phys. Med. Biol., vol. 58, pp. 2955-2967, 2013.

[143] S. Buranurak et al., "*Temperature variations as a source of uncertainty in medical fiber-coupled organic plastic scintillator dosimetry*", Radiation Measurements, vol. 56, pp. 307 - 311, 2013.

[144] J. Hubbell and S. Seltzer, "*NIST X-ray Attenuation Databases*", U.S. Secretary of Commerce, 2004.

[145] S. Beddar, "*On possible temperature dependence of plastic scintillator response*", Medical Physics, vol. 39, no. 10, 2012.

[146] A. Beddar, T. Mackie and F. Attix, "*Water-equivalent plastic scintillation detectors for high-energy beam dosimetry: I. Physical characteristics and theoretical considerations*", Phys. Med. Biol., vol. 37, no. 10, pp. 1883, 1992.

[147] J. Suter et al., "*Ionizing radiation detector using multimode optical fibers*", pp. 104-106 vol.1, 1992.

[148] B. L. Justus and A. L. Huston, "*Fiber-optic-coupled dosemeter for remote optical sensing of radiation*", IRPA9: 1996 international congress on radiation protection. Proceedings., vol. 4, 1996.

[149] P. K. Soltani et al., "*Fiber Optic Radiation Dosimetry*", Proc. SPIE, vol. 1169, pp. 540-551, 1990.

[150] M. Akselrod, L. Bøtter-Jensen and S. McKeever, "*Optically stimulated luminescence and its use in medical dosimetry*", Radiation Measurements, vol. 41, Supplement 1, pp. S78 - S99, 2007.

[151] R. Gaza et al., "*A fiber-dosimetry method based on OSL from Al2O3:C for radiotherapy applications*", Radiation Measurements, vol. 38, no. 4-6, pp. 809-812, 2004.

[152] E. Mones et al., "*Ce-doped optical fibre as radioluminescent dosimeter in radiotherapy*", Radiation Measurements, vol. 43, no. 2–6, pp. 888 - 892, 2008.

[153] N. Chiodini et al., "*Ce-doped SiO2 optical fibers for remote radiation sensing and measurement*", Proc. SPIE, vol. 7316, pp. 731616-731616-8, 2009.

[154] N. Chiodini, A. Vedda and I. Veronese, "*Rare Earth Doped Silica Optical Fibre Sensors for Dosimetry in Medical and Technical Applications*", Advances in Optics, vol. 2014, 2014.

[155] I. Veronese et al., "*Phosphorescence of SiO2 optical fibres doped with Ce3+ ions*", physica status solidi (c), vol. 4, no. 3, pp. 1024–1027, 2007.

[156] I. Veronese et al., "*Radioluminescence dosimetry by scintillating fiber optics: the open challenges*", SPIE Proceedings, vol. 8852, 2013.

[157] M. Carrara et al., "*Temperature dependence of a Ce^{3+} doped SiO2 radioluminescent dosimeter for in vivo dose measurements in HDR brachytherapy*", Radiation Measurements, vol. 71, pp. 324 - 328, 2014.

[158] M. Carrara et al., "*Stem effect of a Ce3+ doped SiO2 optical dosimeter irradiated with a 192Ir {HDR} brachytherapy source*", Radiation Physics and Chemistry, vol. 104, pp. 175 - 179, 2014.

[159] P. Molina et al., "*Characterization of a fiberoptic radiotherapy dosimetry probe based on Mg2SiO4:Tb*", Radiation Measurements, vol. 45, no. 1, pp. 78-82, 2010.

[160] E. G. Yukihara et al., "*Time-resolved optically stimulated luminescence of Al2O3:C for ion beam therapy dosimetry*", Physics in Medicine and Biology, vol. 60, no. 17, pp. 6613, 2015.

[161] F. Issa et al., "*Ge-doped optical fibres as thermoluminescence dosimeters for kilovoltage X-ray therapy irradiations*", Nuclear Instruments and Methods in Physics Research Section A: Accelerators, Spectrometers, Detectors and Associated Equipment, vol. 652, no. 1, pp. 834 - 837, 2011.

[162] F. Issa et al., "*Establishment of Ge-doped optical fibres as thermoluminescence dosimeters for brachytherapy*", Applied Radiation and Isotopes, vol. 70, no. 7, pp. 1158 - 1161, 2012.

[163] F. Issa et al., "*Novel high resolution 125I brachytherapy source dosimetry using Ge-doped optical fibres*", Radiation Physics and Chemistry, vol. 92, no. 0, pp. 48-53, 2013.

[164] F. Therriault-Proulx et al., "*A Phantom Study of an in Vivo Dosimetry System Using Plastic Scintillation Detectors for Real-Time Verification of 192Ir HDR Brachytherapy.*", Medical Physics, vol. 38, no. 5, pp. 2542-2551, 2011.

[165] J. C. Gagnon et al., "*Dosimetric performance and array assessment of plastic scintillation detectors for stereotactic radiosurgery quality assurance*", Medical Physics, vol. 39, no. 1, 2012.

[166] A. Beierholm, C. Behrens and C. Andersen, "*Dosimetric characterization of the Exradin W1 plastic scintillator detector through comparison with an in-house developed scintillator system*", Radiation Measurements, vol. 69, pp. 50 - 56, 2014.

[167] P. Carrasco et al., "*Characterization of the Exradin W1 scintillator for use in radiotherapy*", Medical Physics, vol. 42, no. 1, 2015.

[168] P. Francescon et al., "*Variation of Q clin , Q msr f clin , f msr for the small-field dosimetric parameters percentage depth dose, tissue-maximum ratio, and off-axis ratio*", Medical Physics, vol. 41, no. 10, 2014.

[169] P. Papaconstadopoulos, F. Tessier and J. Seuntjens, "*On the correction, perturbation and modification of small field detectors in relative dosimetry*", Physics in Medicine and Biology, vol. 59, no. 19, pp. 5937, 2014.

[170] A. Bourgouin, N. Varfalvy and L. Archambault, "*Estimating and reducing dose received by cardiac devices for patients undergoing radiotherapy*", Journal of applied clinical medical physics / American College of Medical Physics, vol. 16, no. 6, pp. 5317, 2015.

[171] M. Alhabdan, "*Dosimeters using plastic scintillators and fibre optics*", 2005.

[172] C. Andersen et al., "*Fiber-coupled radioluminescence dosimetry with saturated Al2O3:C crystals: Characterization in 6 and 18 MV photon beams*", Radiation Measurements, vol. 46, no. 10, pp. 1090 - 1098, 2011.

[173] C. E. Andersen et al., "*Characterization of a fiber-coupled Al2O3:C luminescence dosimetry system for online in vivo dose verification during I192r brachytherapy*", Medical Physics, vol. 36, no. 3, 2009.

[174] L. Archambault et al., "*Measurement accuracy and Cerenkov removal for high performance, high spatial resolution scintillation dosimetry*", Medical Physics, vol. 33, no. 1, 2006.

[175] L. Archambault et al., "*Water-equivalent dosimeter array for small-field external beam radiotherapy*", Medical Physics, vol. 34, no. 5, 2007.

[176] D. M. Klein et al., "*Measuring output factors of small fields formed by collimator jaws and multileaf collimator using plastic scintillation detectors*", Medical Physics, vol. 37, no. 10, 2010.

[177] M. Arnfield et al., "*Radiation-induced light in optical fibers and plastic scintillators: application to brachytherapy dosimetry*", Nuclear Science, IEEE Transactions on, vol. 43, no. 3, pp. 2077 - 2084, 1996.

[178] M. C. Aznar et al., "*In vivo absorbed dose measurements in mammography using a new real-time luminescence technique*", The British Journal of Radiology, vol. 78, no. 928, pp. 328-334, 2005.

[179] G. Bartesaghi et al., "*A real time scintillating fiber dosimeter for gamma and neutron monitoring on radiotherapy accelerators*", Nuclear Instruments and Methods in Physics Research Section A: Accelerators, Spectrometers, Detectors and Associated Equipment, vol. 572, no. 1, pp. 228 - 230, 2007.

[180] G. Bartesaghi et al., "*A scintillating fiber dosimeter for radiotherapy*", Nuclear Instruments and Methods in Physics Research Section A: Accelerators, Spectrometers, Detectors and Associated Equipment, vol. 581, no. 1–2, pp. 80 - 83, 2007.

[181] A. Beddar, T. Mackie and F. Attix, "*Cerenkov light generated in optical fibers and other light-pipes irradiated by electron beams*", Phys. Med. Biol., vol. 37, no. 4, pp. 925-935, 1992.

[182] A. S. Beddar et al., "*A miniature "scintillator-fiberoptic-PMT" detector system for the dosimetry of small fields in stereotactic radiosurgery*", Nuclear Science, IEEE Transactions on, vol. 48, no. 3, pp. 924-928, 2001.

[183] A. S. Beddar et al., "*Plastic scintillation dosimetry: optimization of light collection efficiency*", Physics in Medicine and Biology, vol. 48, no. 9, pp. 1141, 2003.

[184] A. Beddar et al., "*A miniature "scintillator-fiberoptic-PMT" detector system for the dosimetry of small fields in stereotactic radiosurgery*", Nuclear Science, IEEE Transactions on, vol. 48, no. 3, pp. 924-928, 2001.

[185] A. S. Beddar, "*Water equivalent plastic scintillation detectors in radiation therapy*", Radiation Protection Dosimetry, vol. 120, no. 1-4, pp. 1-6, 2006.

[186] A. S. Beddar, "*Plastic scintillation dosimetry and its application to radiotherapy*", Radiation Measurements, vol. 41, no. Supplement 1, pp. S124-S133, 2007.

[187] A. Beierholm et al., "*Investigation of linear accelerator pulse delivery using fast organic scintillator measurements*", Radiation Measurements, vol. 45, no. 3–6, pp. 668 - 670, 2010.

[188] A. Beierholm, "*Pulse-resolved radiotherapy dosimetry using fiber-coupled organic scintillators*", 2011.

[189] A. R. Beierholm et al., "*Characterizing a pulse-resolved dosimetry system for complex radiotherapy beams using organic scintillators*", Physics in Medicine and Biology, vol. 56, no. 10, pp. 3033, 2011.

[190] A. Beierholm, C. Behrens and C. Andersen, "*Studying the potential of point detectors in time-resolved dose verification of dynamic radiotherapy*", Radiation Measurements, vol. 82, pp. 129 - 137, 2015.

[191] D. Benoit et al., "*Real-Time Fibered Optically Stimulated Luminescence Dosimeter Based on SrS:Ce,Sm Phosphor*", IEEE Transactions on Nuclear Science, vol. 55, no. 4, pp. 2154-2160, 2008.

[192] D. Benoit et al., "*Feasibility of Fibered Monitoring System for Pulsed Dose-Rate Facilities Based on Radioluminescence of SrS:Ce,Sm Phosphor*", IEEE Transactions on Nuclear Science, vol. 55, no. 6, pp. 3421-3427, 2008.

[193] D. Benoit et al., "*Performance studies of an optical fiber OSL/RL dosimetry system in pulsed high-intensity radiation beams*", Radiation Measurements, vol. 45, no. 36, pp. 688 - 690, 2010.

[194] J. Boivin et al., "*Systematic evaluation of photodetector performance for plastic scintillation dosimetry*", Medical Physics, vol. 42, no. 11, 2015.

[195] S. Boer, A. Beddar and J. Rawlinson, "*Optical filtering and spectral measurements of radiation-induced light in plastic scintillation dosimetry*", Physics in Medicine and Biology, vol. 38, no. 7, pp. 945, 1993.

[196] L. E. Cartwright et al., "*Dose mapping of the rectal wall during brachytherapy with an array of scintillation dosimeters*", Medical Physics, vol. 37, no. 5, 2010.

[197] T. Chen, "*Scintillator wavelength influence in an optical dosimeter*", 2006.

[198] M. A. Clift, R. A. Sutton and D. V. Webb, "*Dealing with Cerenkov radiation generated in organic scintillator dosimeters by bremsstrahlung beams*", Physics in Medicine and Biology, vol. 45, no. 5, pp. 1165, 2000.

[199] M. A. Clift, R. A. Sutton and D. V. Webb, "*Water equivalence of plastic organic scintillators in megavoltage radiotherapy bremsstrahlung beams*", Physics in Medicine and Biology, vol. 45, no. 7, pp. 1885, 2000.

[200] M. A. Clift, P. N. Johnston and D. V. Webb, "*A temporal method of avoiding the Cerenkov radiation generated in organic scintillator dosimeters by pulsed mega-voltage electron and photon beams*", Physics in Medicine and Biology, vol. 47, no. 8, pp. 1421, 2002.

[201] A. Correia, R. Pirraco and C. C. Rosa, "*Validation of dose measurements by scintillating fiber optic dosimeters for medical applications*", Proc. SPIE, vol. 8785, pp. 8785F5-8785F5-7, 2013.

[202] C. Dilcher et al., "*Dose mapping of porcine coronary arteries using an optical fiber dosimeter*", Cardiovascular Revascularization Medicine, vol. 6, no. 4, pp. 163 - 169, 2005.

[203] L. Dusseau and J. Gasiot, "*Online and realtime dosimetry using optically stimulated luminescence*", International Journal of High Speed Electronics and Systems, vol. 14, no. 02, pp. 605-623, 2004.

[204] A. F. Fernandez et al., "*Real-time fibre optic radiation dosimeters for nuclear environment monitoring around thermonuclear reactors*", Fusion Engineering and Design, vol. 83, no. 1, pp. 50-59, 2008.

[205] A. M. Frelin et al., "*Spectral discrimination of Čerenkov radiation in scintillating dosimeters*", Medical Physics, vol. 32, no. 9, 2005.

[206] J. Fontbonne et al., "*Scintillating fiber dosimeter for radiation therapy accelerator*", Nuclear Science, IEEE Transactions on, vol. 49, no. 5, pp. 2223-2227, 2002.

[207] M. Guillot et al., "*Spectral method for the correction of the Cerenkov light effect in plastic scintillation detectors: A comparison study of calibration procedures and validation in Cerenkov light-dominated situations*", Medical Physics, vol. 38, no. 4, 2011.

[208] M. Ishikawa et al., "*A feasibility study of novel plastic scintillation dosimetry with pulse-counting mode*", Physics in Medicine and Biology, vol. 54, no. 7, pp. 2079, 2009.

[209] M. Ishikawa et al., "*Development of a wavelength-separated type scintillator with optical fiber (SOF) dosimeter to compensate for the Cerenkov radiation effect*", Journal of Radiation Research, vol. 56, no. 2, pp. 372-381, 2015.

[210] A. Ismail et al., "*In vivo dosimetric system based on Gallium Nitride radioluminescence*", Radiation Measurements, vol. 46, no. 12, pp. 1960 - 1962, 2011.

[211] K. W. Jang et al., "*Measurement of Cerenkov light in a fiber-optic radiation sensor by high energy photon and electron beams*", J. Korean Phys.Soc., vol. 56, no. 765, .

[212] K. W. Jang et al., "*Measurements of relative depth doses and Cerenkov light using a scintillating fiber optic dosimeter with Co-60 radiotherapy source*", Applied Radiation and Isotopes, vol. 70, no. 1, pp. 274 - 277, 2012.

[213] A. Huston et al., "*Remote optical fiber dosimetry*", Nuclear Instruments and Methods in Physics Research Section B: Beam Interactions with Materials and Atoms, vol. 184, no. 12, pp. 55 - 67, 2001.

[214] A. L. Huston et al., "*Optically Stimulated Luminescent Glass Optical Fibre Dosemeter*", Radiation Protection Dosimetry, vol. 101, no. 1-4, pp. 23-26, 2002.

[215] B. L. Justus et al., "*Gated fiber-optic-coupled detector for in vivo real-time radiation dosimetry*", Appl. Opt., vol. 43, no. 8, pp. 1663–1668, 2004.

[216] B. L. Justus et al., "*Elimination of Cerenkov interference in a fibre-optic-coupled radiation dosemeter*", Radiat. Prot. Dosim., vol. 120, no. 1-4, pp. 20, 2006.

[217] G. Kertzscher et al., "*Stem signal suppression in fiber-coupled Al2O3:C dosimetry for 192Ir brachytherapy*", Radiation Measurements, vol. 46, no. 12, pp. 2020 - 2024, 2011.

[218] G. Kertzscher et al., "*Identifying afterloading PDR and HDR brachytherapy errors using real-time fiber-coupled Al_2O_3:C dosimetry and a novel statistical error decision criterion*", Radiotherapy and Oncology, vol. 100, no. 3, pp. 456 - 462, 2011.

[219] D. C. Konnoff, T. K. Plant and E. Shiner, "*SSPM based radiation sensing: Preliminary laboratory and clinical results*", Radiation Measurements, vol. 46, no. 1, pp. 76-87, 2011.

[220] J. Lambert et al., "*A plastic scintillation dosimeter for high dose rate brachytherapy*", Physics in Medicine and Biology, vol. 51, no. 21, pp. 5505, 2006.

[221] J. Lambert et al., "*A fibre optic dosimeter for prostate cancer therapy*", In *Optical Fibre Technology/Australian Optical Society, 2006. ACOFT/AOS 2006. Australian Conference on*, 2006.

[222] J. Lambert et al., "*In vivo dosimeters for HDR brachytherapy: A comparison of a diamond detector, MOSFET, TLD, and scintillation detector*", Medical Physics, vol. 34, no. 5, 2007.

[223] J. Lambert et al., "*Cerenkov-free scintillation dosimetry in external beam radiotherapy with an air core light guide*", Physics in Medicine and Biology, vol. 53, no. 11, pp. 3071, 2008.

[224] J. Lambert et al., "*A prototype scintillation dosimeter customized for small and dynamic megavoltage radiation fields*", Physics in Medicine and Biology, vol. 55, no. 4, pp. 1115, 2010.

[225] J. J. Lee et al., "*A method to remove residual signals in fibre optic luminescence dosimeters*", Physics in Medicine and Biology, vol. 58, no. 5, pp. 1581, 2013.

[226] B. Lee et al., "*Measurements and elimination of Cherenkov light in fiber-optic scintillating detector for electron beam therapy dosimetry*", Nuclear Instruments and Methods in Physics Research Section A: Accelerators, Spectrometers, Detectors and Associated Equipment, vol. 579, no. 1, pp. 344 - 348, 2007.

[227] B. Lee et al., "*Characterization of one-dimensional fiber-optic scintillating detector for electron beam therapy dosimetry*", In *2007 IEEE Nuclear Science Symposium Conference Record*, 2007.

[228] B. Lee et al., "*Development of One-dimensional Fiber-Optic Radiation Sensor for Measuring Dose Distributions of High Energy Photon Beams*", Optical Review, vol. 14, no. 5, pp. 351–354, 2007.

[229] P. Molina et al., "*Characterization of new materials for fiberoptic dosimetry*", Journal of Physics: Conference Series, vol. 313, no. 1, pp. 012007, 2011.

[230] C. De Mattia et al., "*Recent progresses in scintillating doped silica fiber optics*", Proc. SPIE, vol. 9213, pp. 92131F-92131F-8, 2014.

[231] C. De Mattia et al., "*Ionizing radiation detection by Yb-doped silica optical fibers*", Proceedings of SPIE - The International Society for Optical Engineering, vol. 9593, 2015.

[232] L. Moutinho et al., "*Development of a scintillating optical fiber dosimeter with silicon photomultipliers*", Nuclear Instruments and Methods in Physics Research Section A: Accelerators, Spectrometers, Detectors and Associated Equipment, vol. 735, pp. 640 - 643, 2014.

[233] L. M. Moutinho et al., "*Fiber optic dosimeter with silicon photomultipliers*", Proc. SPIE, vol. 9286, pp. 92864Q-92864Q-5, 2014.

[234] L. Moutinho et al., "*Brachytherapy dosimeter with silicon photomultipliers*", Nuclear Instruments and Methods in Physics Research Section A: Accelerators, Spectrometers, Detectors and Associated Equipment, vol. 787, pp. 358 - 360, 2015.

[235] L. Nascimento et al., "*Medical dosimetry using a RL/OSL prototype*", Radiation Measurements, vol. 71, pp. 359 - 363, 2014.

[236] L. Nascimento et al., "*Application of Al2O3:C+fibre dosimeters for 290 MeV/n carbon therapeutic beam dosimetry*", Radiation Physics and Chemistry, vol. 115, pp. 75 - 80, 2015.

[237] P. Naseri, N. Suchowerska and D. R. McKenzie, "*Scintillation dosimeter arrays using air core light guides: simulation and experiment*", Physics in Medicine and Biology, vol. 55, no. 12, pp. 3401, 2010.

[238] P. Pittet et al., "*Fiber background rejection and crystal over-response compensation for GaN based in vivo dosimetry*", Physica Medica, vol. 29, no. 5, pp. 487 - 492, 2013.

[239] F. Rego and L. Peralta, "*Si-PIN photodiode readout for a scintillating optical fiber dosimeter*", Radiation Measurements, vol. 47, no. 10, pp. 947-950, 2012.

[240] F. Rego et al., "*Small dimension plastic dosimeter in high dose rate brachytherapy with 192Ir source*", In *Nuclear Science Symposium and Medical Imaging Conference (NSS/MIC), 2011 IEEE*, 2011.

[241] A. M. C. Santos, M. Mohammadi and S. A. V., "*Investigation of a fibre-coupled beryllium oxide (BeO) ceramic luminescence dosimetry system*", Radiation Measurements, vol. 70, pp. 52 - 58, 2014.

[242] S. Stefanowicz et al., "*Dosimetry in clinical static magnetic fields using plastic scintillation detectors*", Radiation Measurements, vol. 56, pp. 357 - 360, 2013.

[243] N. Suchowerska et al., "*A fibre optic dosimeter customised for brachytherapy*", Radiation Measurements, vol. 42, no. 4-5, pp. 929-932, 2007.

[244] N. Suchowerska et al., "*Clinical Trials of a Urethral Dose Measurement System in Brachytherapy Using Scintillation Detectors*", International Journal of Radiation Oncology*Biology*Physics, vol. 79, no. 2, pp. 609-615, 2011.

[245] J. A. Tanyi et al., "*Performance characteristics of a gated fiber-optic-coupled dosimeter in high-energy pulsed photon radiation dosimetry*", Applied Radiation and Isotopes, vol. 68, no. 2, pp. 364-369, 2010.

[246] J. A. Tanyi et al., "*Characterization of a gated fiber-optic-coupled detector for application in clinical electron beam dosimetry*", Medical Physics, vol. 38, no. 2, 2011.

[247] F. Therriault-Proulx et al., "*Technical Note: Removing the stem effect when performing Ir-192 HDR brachytherapy in vivo dosimetry using plastic scintillation detectors: A relevant and necessary step*", Medical Physics, vol. 38, no. 4, pp. 2176–2179, 2011.

[248] R. Wang et al., "*Implementation of GaN based real-time source position monitoring in HDR brachytherapy*", Radiation Measurements, vol. 71, pp. 293 - 296, 2014.

[249] K. Watanabe et al., "*Development of a micro-size dosimeter using an optical fiber probe based on photostimulable phosphorescence*", Radiation Measurements, vol. 55, pp. 64 - 67, 2013.

[250] L. Wootton, "*In Vivo Dosimetry using Plastic Scintillation Detectors for External Beam Radiation Therapy*", 2014.

[251] W. J. Yoo et al., "*Development of a scintillating fiber-optic dosimeter for measuring the entrance surface dose in diagnostic radiology*", Radiation Measurements, vol. 48, no. 0, pp. 29-34, 2013.

[252] W. J. Yoo et al., "*Simultaneous measurements of pure scintillation and Cerenkov signals in an integrated fiber-optic dosimeter for electron beam therapy dosimetry*", Opt. Express, vol. 21, no. 23, pp. 27770–27779, 2013.

[253] W. J. Yoo et al., "*Measurement of Entrance Surface Dose on an Anthropomorphic Thorax Phantom Using a Miniature Fiber-Optic Dosimeter*", Sensors, vol. 14, no. 4, pp. 6305, 2014.

[254] W. J. Yoo et al., "*Development of a Small-Sized, Flexible, and Insertable Fiber-Optic Radiation Sensor for Gamma-Ray Spectroscopy*", Sensors, vol. 15, no. 9, pp. 21265, 2015.

[255] A. R. Beierholm et al., "*A comparison of BCF-12 organic scintillators and Al2O3:C crystals for real-time medical dosimetry*", Radiation Measurements, vol. 43, no. 2-6, pp. 898-903, 2008.

[256] C. E. Andersen et al., "*Temperature coefficients for in vivo RL and OSL dosimetry using*", Radiation Measurements, vol. 43, no. 2–6, pp. 948 - 953, 2008.

[257] F. Therriault-Proulx, L. Wootton and S. Beddar, "*A method to correct for temperature dependence and measure simultaneously dose and temperature using a plastic scintillation detector*", Physics in Medicine and Biology, vol. 60, no. 20, pp. 7927, 2015.

[258] G. Kertzscher et al., "*In vivo dosimetry: trends and prospects for brachytherapy*", The British Journal of Radiology, vol. 87, no. 1041, pp. 20140206, 2014.

[259] P. Z. Y. Liu et al., "*Plastic scintillation dosimetry: comparison of three solutions for the Cerenkov challenge*", Physics in Medicine and Biology, vol. 56, no. 18, pp. 5805, 2011.

[260] A. M. C. A. C. E. Marckmann C J and L. Botter-Jensen, "*Influence of the stem effect on radioluminescence signals from optical fibre Al 2 O 3 :C dosemeters*", Radiat. Prot. Dosim., vol. 119, no. 1-4, pp. 363, 2006.

[261] C. E. Andersen et al., "*An algorithm for real-time dosimetry in intensity-modulated radiation therapy using the radioluminescence signal from Al2O3:C*", Radiation Protection Dosimetry, vol. 120, no. 1-4, pp. 7-13, 2006.

[262] J. Venselaar and J. Perez-Calatayud, "*A Practical Guide to Quality Control of Brachytherapy Equipment*", IAEA, 2000.

[263] S. G. Crystals, "*Scintillating Optical Fibers*", Saint-Gobain Crystals, 2008.

[264] K. W. Jang et al., "*Application of Cerenkov radiation generated in plastic optical fibers for therapeutic photon beam dosimetry*", Journal of Biomedical Optics, vol. 18, no. 2, pp. 027001-027001, 2013.

[265] K. W. Jang et al., "*Measurement of Cerenkov Radiation Induced by the Gamma-Rays of Co-60 Therapy Units Using Wavelength Shifting Fiber*", Sensors, vol. 14, no. 4, pp. 7013, 2014.

[266] R. Nowotny, "*Radioluminescence of some optical fibres*", Phys. Med. Biol., vol. 52, no. 4, pp. N67-N73, 2007.

[267] H. Freitas, "*Caraterização in Vitro de um Dosimetro de Fibra Optica para Braquiterapia de HDR*", 2015.

[268] J. Veloso, L. Moutinho and I. Castro, "*Dosímetro de fibra óptica cintilante*", no. PT106337, 2012.

[269] U. Schnöckel et al., "*Small-animal PET: A promising, non-invasive tool in pre-clinical research*", European Journal of Pharmaceutics and Biopharmaceutics, vol. 74, no. 1, pp. 50 - 54, 2010.

[270] M. E. Phelps, "*PET: The Merging of Biology and Imaging into Molecular Imaging*", Journal of Nuclear Medicine, vol. 41, no. 4, pp. 661-681, 2000.

[271] R. Yao, R. Lecomte and E. S. Crawford, "*Small-Animal PET: What Is It, and Why Do We Need It?*", Journal of Nuclear Medicine Technology, vol. 40, no. 3, pp. 157-165, 2012.

[272] S. Cherry, D. Badawi and J. Qi, "*Essentials of In Vivo Biomedical Imaging*", CRC Press, 2015.

[273] W. R. Hendee and E. R. Ritenour, "*Medical Imaging Physics*", Wiley-Liss, 2002.

[274] P. Christian and K. Waterstram-Rich, "*Nuclear Medicine and PET/CT: Technology and Techniques*", Elsevier, 2012.

[275] A. D. Guerra et al., "*Advances in position-sensitive photodetectors for PET applications*", Nuclear Instruments and Methods in Physics Research Section A: Accelerators, Spectrometers, Detectors and Associated Equipment, vol. 604, no. 1–2, pp. 319 - 322, 2009.

[276] J. T. Bushberg, "*The Essential physics of medical imaging*", Lippincott Williams & Wilkins, 2002.

[277] A. Rahmim and H. Zaidi, "*PET versus SPECT: strengths, limitations and challenges*", Nuclear Medicine Communications, vol. 29, pp. 193–207, 2008.

[278] J. Torres et al., "*Positron Emission Tomography - Recent Developments in Instrumentation, Research and Clinical Oncological Practice*", 2013-12-18.

[279] A. Nassalski et al., "*Comparative study of scintillators for PET/CT detectors*", In *Nuclear Science Symposium Conference Record, 2005 IEEE*, 2005.

[280] T. Bäck et al., "*An educational tool for demonstrating the TOF-PET technique*", Nuclear Instruments and Methods in Physics Research Section A: Accelerators, Spectrometers, Detectors and Associated Equipment, vol. 471, no. 1–2, pp. 200 - 204, 2001.

[281] T. Bäck et al., "*A TOF-PET system for educational purposes*", Nuclear Instruments and Methods in Physics Research Section A: Accelerators, Spectrometers, Detectors and Associated Equipment, vol. 477, no. 1–3, pp. 82 - 87, 2002.

[282] K. E. Johansson, C. Nilsson and P. E. Tegner, "*An educational PET camera model*", Physics Education, vol. 41, no. 5, pp. 437, 2006.

[283] R. Pedro et al., "*The MiniPET: a didactic PET system*", Journal of Instrumentation, vol. 8, no. 03, pp. C03005, 2013.

[284] E. Bolle et al., "*COMPET – high resolution and high sensitivity PET scanner with novel readout concept: Setup and simulations*", Nuclear Instruments and Methods in Physics Research Section A: Accelerators, Spectrometers, Detectors and Associated Equipment, vol. 648, Supplement 1, pp. S93 - S95, 2011.

[285] M. Rissi et al., "*Characterization of a high resolution and high sensitivity pre-clinical {PET} scanner with 3D event reconstruction*", Nuclear Instruments and Methods in Physics Research Section A: Accelerators, Spectrometers, Detectors and Associated Equipment, vol. 695, pp. 135 - 138, 2012.

[286] F. Retière et al., "*Development of a low cost planar detector for positron emission tomography*", Nuclear Instruments and Methods in Physics Research Section A: Accelerators, Spectrometers, Detectors and Associated Equipment, vol. 695, pp. 139 - 142, 2012.

[287] K. E. Hines et al., "*COMPET: High resolution high sensitivity MRI compatible pre-clinical PET scanner*", Nuclear Instruments and Methods in Physics Research Section A: Accelerators, Spectrometers, Detectors and Associated Equipment, vol. 732, pp. 581 - 585, 2013.

[288] P. Lecoq and J. Varela, "*Clear-PEM, a dedicated PET camera for mammography*", Nuclear Instruments and Methods in Physics Research Section A: Accelerators, Spectrometers, Detectors and Associated Equipment, vol. 486, no. 1–2, pp. 1 - 6, 2002.

[289] M. Abreu et al., "*Design and evaluation of the clear-PEM scanner for positron emission mammography*", Nuclear Science, IEEE Transactions on, vol. 53, no. 1, pp. 71-77, 2006.

[290] P. Amaral et al., "*Performance and quality control of Clear-PEM detector modules*", Nuclear Instruments and Methods in Physics Research Section A: Accelerators, Spectrometers, Detectors and Associated Equipment, vol. 580, no. 2, pp. 1123 - 1126, 2007.

[291] P. Amaral et al., "*Long-term stability of the Clear-PEM detector modules*", Nuclear Instruments and Methods in Physics Research Section A: Accelerators, Spectrometers, Detectors and Associated Equipment, vol. 571, no. 1–2, pp. 488 - 492, 2007.

[292] J. Varela, "*A PET imaging system dedicated to mammography*", Radiation Physics and Chemistry, vol. 76, no. 2, pp. 347 - 350, 2007.

[293] E. Albuquerque et al., "*Experimental characterization of the 192 channel Clear-PEM frontend ASIC coupled to a multi-pixel APD readout of LYSO:Ce crystals*", Nuclear Instruments and Methods in Physics Research Section A: Accelerators, Spectrometers, Detectors and Associated Equipment, vol. 598, no. 3, pp. 802 - 814, 2009.

[294] N. Oliveira et al., "*Optimization of 2D image reconstruction for positron emission mammography using IDL*", Computers in Biology and Medicine, vol. 39, no. 2, pp. 119 - 129, 2009.

[295] J. Trummer, E. Auffray and P. Lecoq, "*Simulation results of a veto counter for the ClearPEM*", Nuclear Instruments and Methods in Physics Research Section A: Accelerators, Spectrometers, Detectors and Associated Equipment, vol. 602, no. 2, pp. 614 - 617, 2009.

[296] J. Mesquita et al., "*Choosing the ART relaxation parameter for Clear-PEM 2D image reconstruction*", Computer Methods and Programs in Biomedicine, vol. 98, no. 2, pp. 183 - 190, 2010.

[297] M. Abrantes et al., "*ClearPEM scanners: Performance results and studies in preclinical environment*", In *Nuclear Science Symposium and Medical Imaging Conference (NSS/MIC), 2011 IEEE*, 2011.

[298] J. A. Neves, "*The ClearPEM breast imaging scanner*", Nuclear Instruments and Methods in Physics Research Section A: Accelerators, Spectrometers, Detectors and Associated Equipment, vol. 628, no. 1, pp. 444 - 447, 2011.

[299] L. Martins et al., "*Scatter Correction for Positron Emission Mammography using an Estimation of Trues Method Approach*", Procedia Technology, vol. 5, pp. 903 - 911, 2012.

[300] V. Veckalns et al., "*Detection sensitivity and light collection studies of an APD-based high packing-fraction LYSO:Ce matrix for PET applications*", Nuclear Instruments and Methods in Physics Research Section A: Accelerators, Spectrometers, Detectors and Associated Equipment, vol. 732, pp. 607 - 610, 2013.

[301] J. Y. Hwang et al., "*Optimization of a partially segmented block detector for MR-compatible small animal PET*", Nuclear Instruments and Methods in Physics Research Section A: Accelerators, Spectrometers, Detectors and Associated Equipment, vol. 652, no. 1, pp. 815 - 818, 2011.

[302] E. Yoshida et al., "*Impact of Laser-Processed X'tal Cube Detectors on PET Imaging in a One-Pair Prototype System*", Nuclear Science, IEEE Transactions on, vol. 60, no. 5, pp. 3172-3180, 2013.

[303] E. Yoshida et al., "*The X'tal cube PET detector with a monolithic crystal processed by the 3D sub-surface laser engraving technique: Performance comparison with glued crystal elements*", Nuclear Instruments and Methods in Physics Research Section A: Accelerators, Spectrometers, Detectors and Associated Equipment, vol. 723, pp. 83 - 88, 2013.

[304] E. Yoshida et al., "*Spatial resolution limits for the isotropic-3D PET detector X'tal cube*", Nuclear Instruments and Methods in Physics Research Section A: Accelerators, Spectrometers, Detectors and Associated Equipment, vol. 728, pp. 107 - 111, 2013.

[305] Y. E. et al., "*Intrinsic spatial resolution evaluation of the X'tal cube PET detector based on a 3D crystal block segmented by laser processing*", Radiological Physics and Technology, vol. 6, no. 1, pp. 21-27, 2013.

[306] Y. E. et al., "*Design study of the DOI-PET scanners with the X'tal Cubes Toward sub-millimeter spatial resolution*", Journal of Medical Imaging and Health Informatics, vol. 3, no. 1, pp. 131-134, 2013.

[307] E. Yoshida et al., "*Development of a single-ring OpenPET prototype*", "Nuclear Instruments and Methods in Physics Research Section A: Accelerators, Spectrometers, Detectors and Associated Equipment ", vol. "729", pp. "800 - 808", 2013.

[308] Y. Hirano et al., "*Potential for reducing the numbers of SiPM readout surfaces of laser-processed X'tal cube PET detectors*", Physics in Medicine and Biology, vol. 58, no. 5, pp. 1361, 2013.

[309] F. Nishikido et al., "*Four-layer DOI PET detectors using a multi-pixel photon counter array and the light sharing method*", Nuclear Instruments and Methods in Physics Research Section A: Accelerators, Spectrometers, Detectors and Associated Equipment, vol. 729, pp. 755 - 761, 2013.

[310] I. N. et al., "*X'tal cube PET detector composed of a stack of scintillator plates segmented by laser processing*", IEEE Transactions on Nuclear Science, vol. 61, no. 1, pp. 53-59, 2014.

[311] A. Braem et al., "*AX-PET: A novel PET detector concept with full 3D reconstruction*", Nuclear Instruments and Methods in Physics Research Section A: Accelerators, Spectrometers, Detectors and Associated Equipment, vol. 610, no. 1, pp. 192 - 195, 2009.

[312] P. Beltrame et al., "*Construction and tests of demonstrator modules for a 3-D axial PET system for brain or small animal imaging*", Nuclear Instruments and Methods in Physics Research Section A: Accelerators, Spectrometers, Detectors and Associated Equipment, vol. 636, no. 1, Supplement, pp. S226 - S230, 2011.

[313] C. Joram, "*Imaging results and TOF studies with axial PET detectors*", Nuclear Instruments and Methods in Physics Research Section A: Accelerators, Spectrometers, Detectors and Associated Equipment, vol. 732, pp. 586 - 590, 2013.

[314] E. Bolle et al., "*The AX-PET experiment: A demonstrator for an axial Positron Emission Tomograph*", Nuclear Instruments and Methods in Physics Research Section A: Accelerators, Spectrometers, Detectors and Associated Equipment, vol. 718, pp. 126 - 129, 2013.

[315] C. Casella et al., "*A high resolution TOF-PET concept with axial geometry and digital SiPM readout*", Nuclear Instruments and Methods in Physics Research Section A: Accelerators, Spectrometers, Detectors and Associated Equipment, vol. 736, pp. 161 - 168, 2014.

[316] C. Kuntner and D. B. Stout, "*Quantitative preclinical PET imaging: opportunities and challenges*", Frontiers in Physics, vol. 2, no. 12, 2014.

[317] V. Arosio et al., "*easyPET a novel concept for an affordable tomographic system*", NIM-A, 2016.

[318] P. Bérard et al., "*Development of a 64-channel {APD} detector module with individual pixel readout for submillimetre spatial resolution in {PET}*", Nuclear Instruments and Methods in Physics Research Section A: Accelerators, Spectrometers, Detectors and Associated Equipment, vol. 610, no. 1, pp. 20 - 23, 2009.

[319] F. R. Schneider et al., "*A Submillimeter Resolution PET Prototype Evaluated With an ^{18}F Inkjet Printed Phantom*", IEEE Transactions on Nuclear Science, vol. 62, no. 5, pp. 2043-2047, 2015.

Appendices

Appendix A

SiPM readout board

The developed dual channel PCB for the SiPMs comprises both dual mode readouts (Figure A.1).

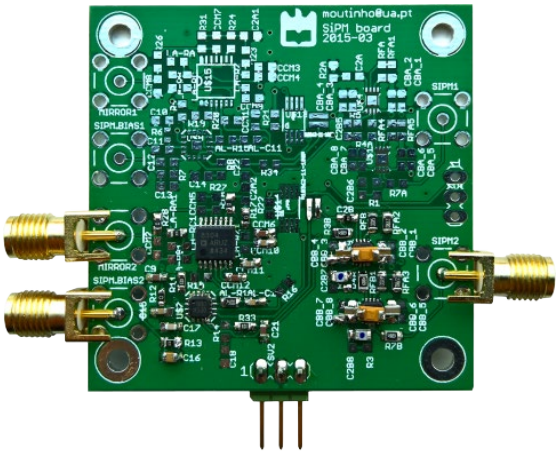

Figure A.1: Developed dual channel PCB for SiPM dual mode readout (with only 1 channel populated).

For the pulse mode readout, the developed amplification system comprehends an I-V conversion stage followed by a 2nd stage for gain, as schematics in Figure A.2. Two ultra-low noise 3.8 GHz AD8099 high speed op-amps from Analog Devices are used. The supply current is as low as 15 mA per op-amp. Each stage has a gain of 20, corresponding to a -3 dB SS Bandwidth. A digital temperature sensor (DS18B20) allows local temperature monitoring.

For the current mode an ALD5317 current mirror coupled to an AD8304 logarithmic amplifier is used, as depicted in Figure A.3.

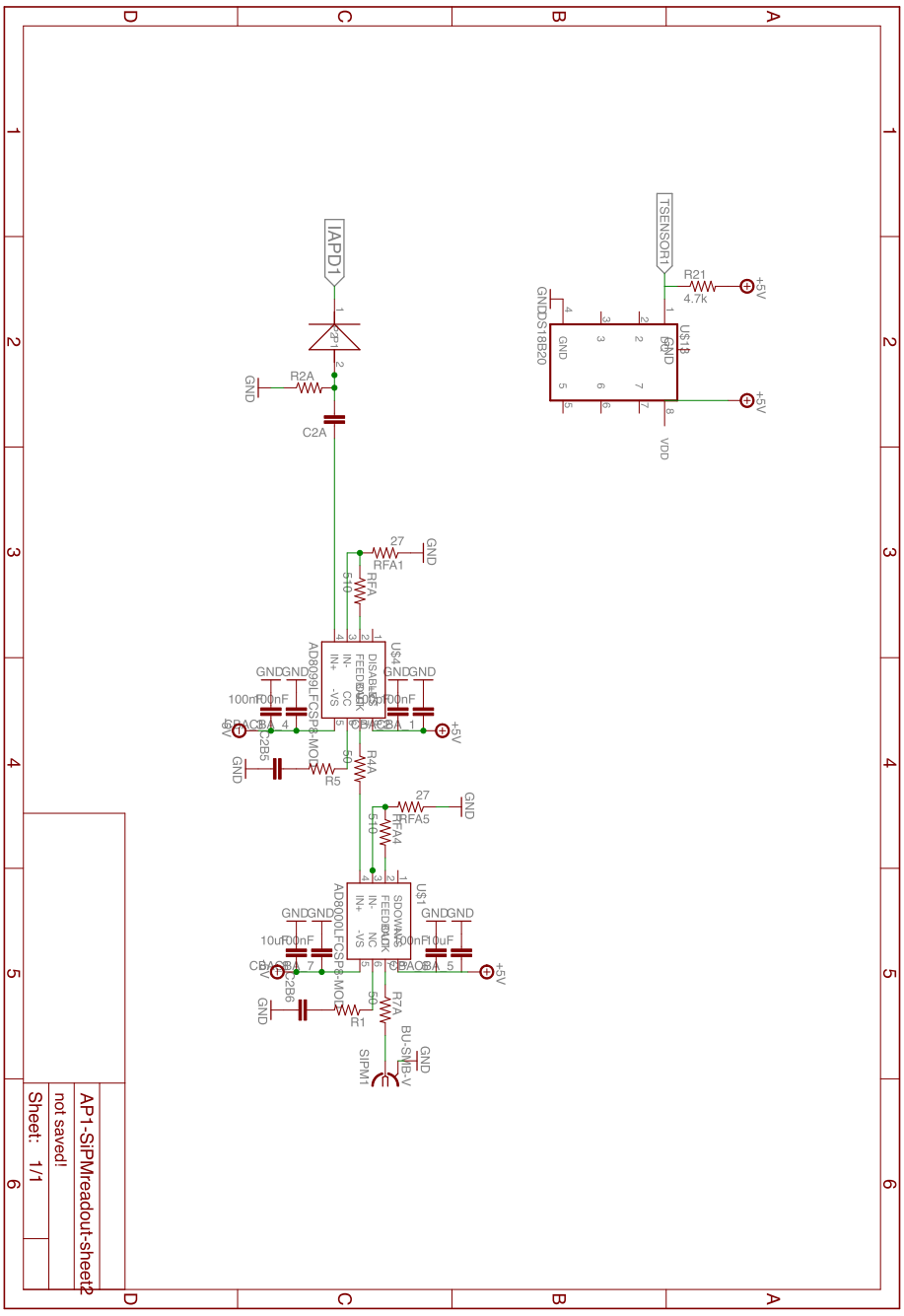

Figure A.2: Schematics of the SiPM pulse mode readout.

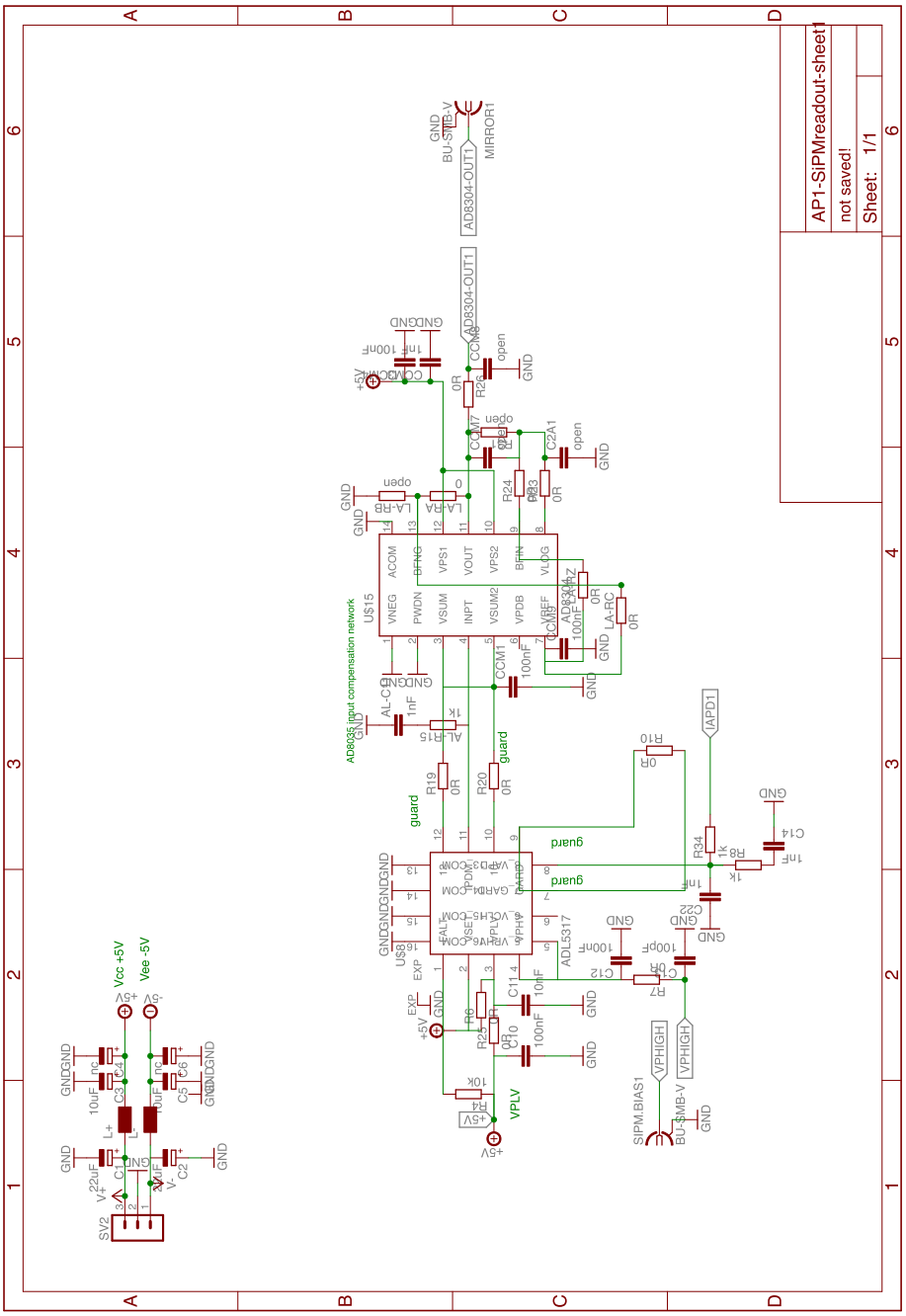

Figure A.3: Schematics of the SiPM current mode readout.

Appendix B

SiPM bias PCB

A dual channel module for two SiPMs biasing was developed, Figure B.1. For each channel a MAX1832 is used. The MAX1932 integrates accurate high-side current limiting to protect APDs under avalanche conditions. The IC integrates an 8-Bit SPI-Compatible DAC. The PCB schematics is depicted in Figure B.2.

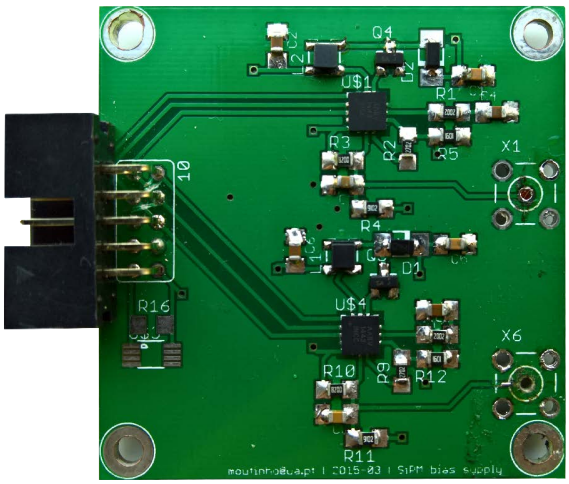

Figure B.1: Printed circuit board of the 2-channel SiPM bias.

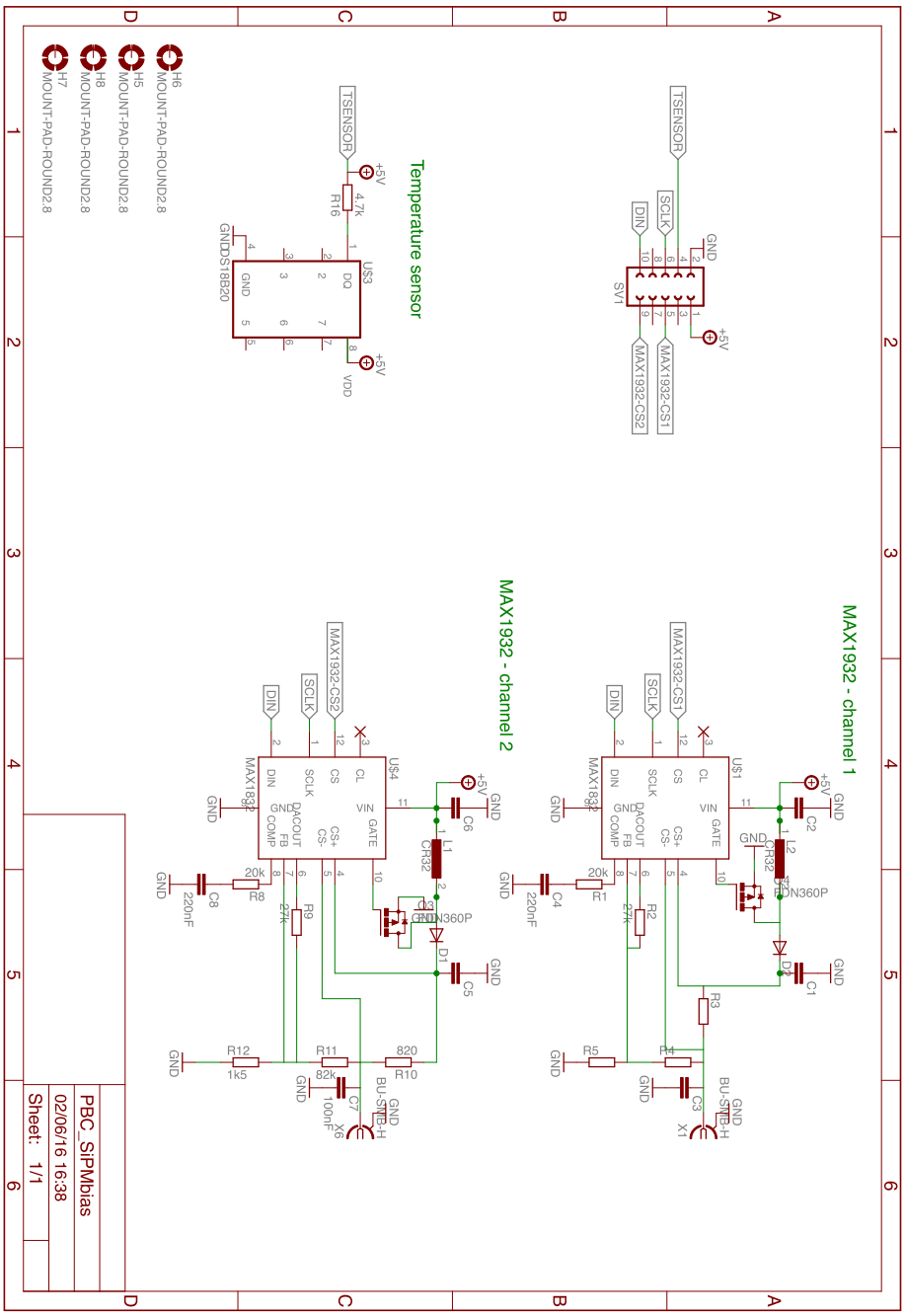

Figure B.2: Schematics of the circuit board of the 2-channel SiPM bias.

Appendix C

Coincidence board

A module for coincidence detection was developed, Figure C.1. This logic module comprehends two MAX9011 comparators. The threshold voltage to both comparators is provided by a MAX5700 DAC. The comparators output signal is a TTL signal with duration corresponding the the period over which the SiPM signal is higher than the provided threshold voltage. For the purpose of increase the signal width, a SN74LVC1G123 monostable multi-vibrator is used. The same IC is used for widening the coincidence signal provided by the SN74AUC1G08 AND Gate. The PCB schematics is depicted in Figure fg:AP3-logicboard.

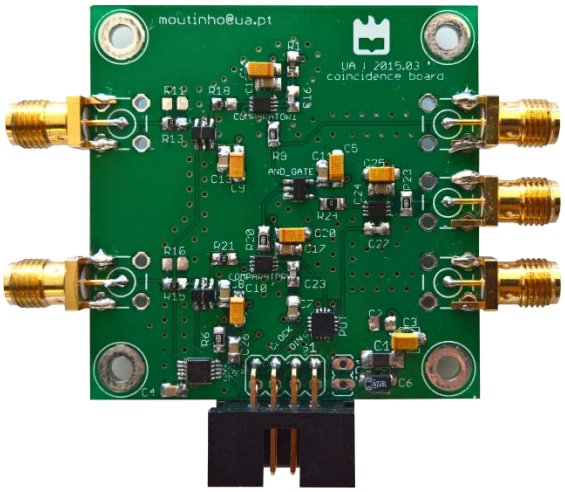

Figure C.1: Printed circuit board of the coincidence unit.

In Figure C.2, is depicted an oscilloscope (LeCroy Waverunner 625 Zi) screen capture of the two SiPM pulses, two comparator outputs (after the monostable multi-vibrator) and the coincidence signal. As noticed, there is an ∼15 ns delay between the SiPM and coincidence signals due to the both comparator and monostable multi-vibrator propagation delay.

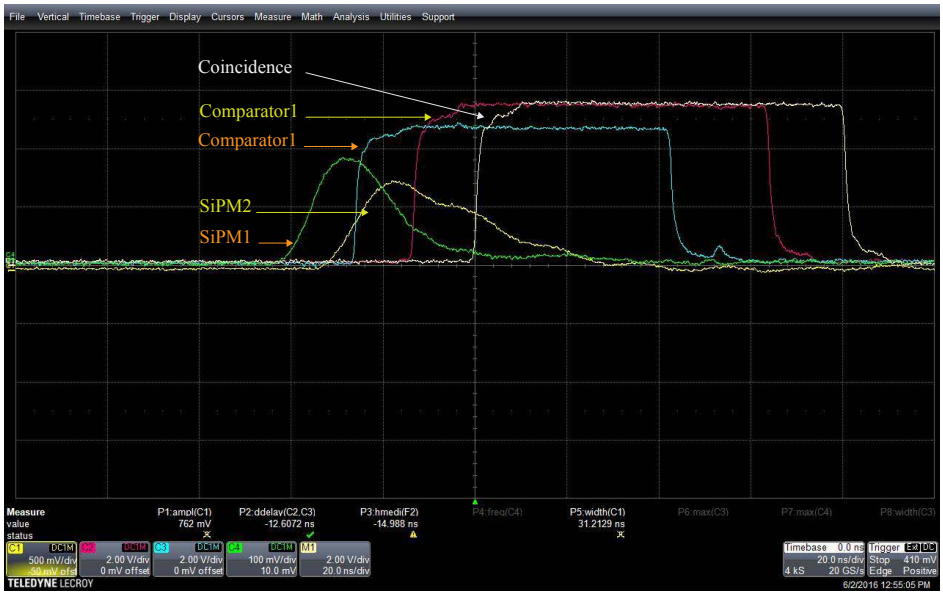

Figure C.2: Screen capture of two SiPMs operating in coincidence mode with coincidence signal used as oscilloscope trigger.

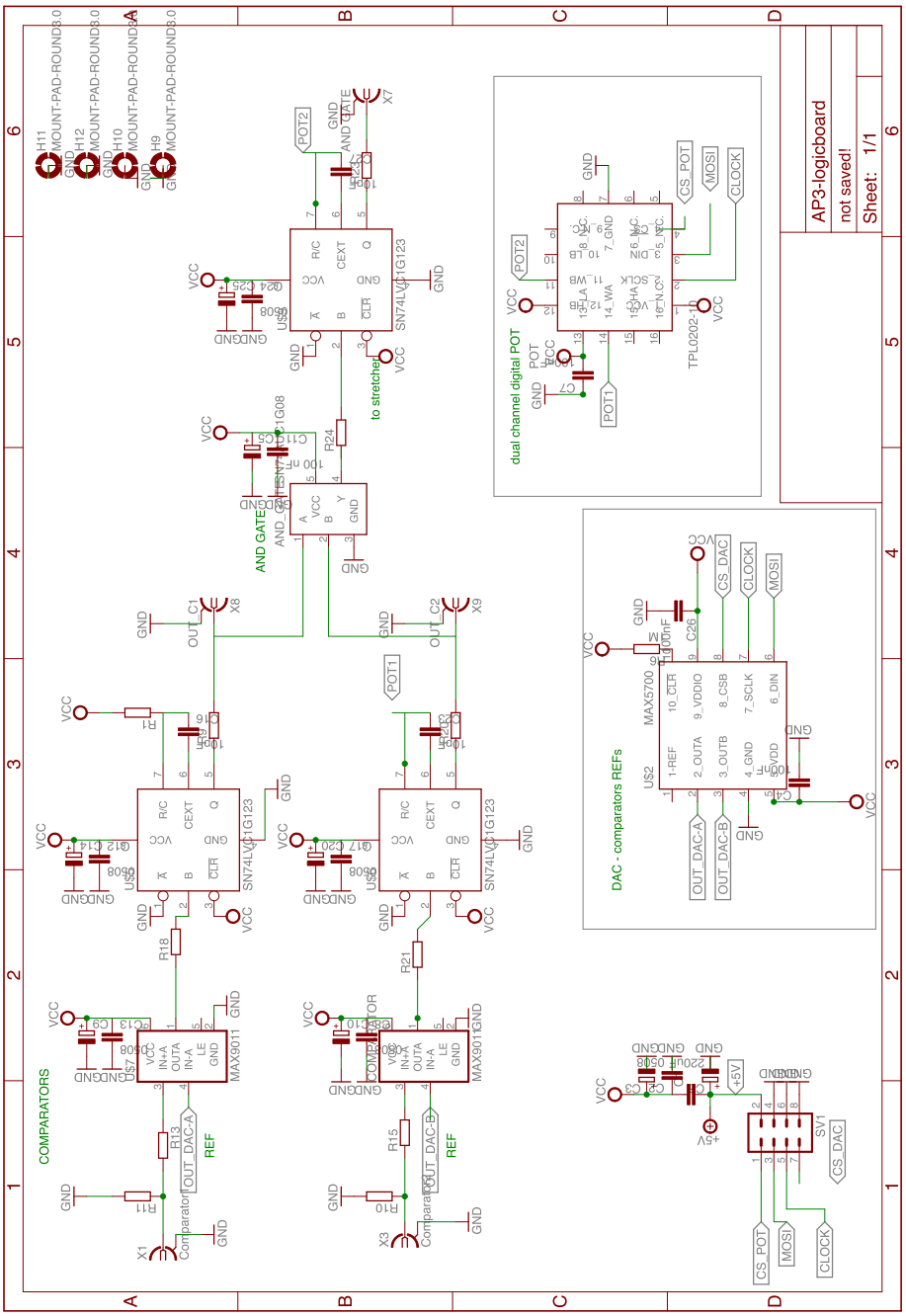

Figure C.3: Schematics of the coincidence circuit board.